QUALIFICATION OF LASER POWDER BED FUSION PROCESSED 17-4 PH STAINLESS STEEL AS A FUNCTION OF POWDER CONDITION

A Thesis
Presented to
The Academic Faculty

by

Jaime Michael Schnaier Berez

In Partial Fulfillment
of the Requirements for the Degree
Master of Science in the
George W. Woodruff School of Mechanical Engineering

Georgia Institute of Technology
August 2020

QUALIFICATION OF LASER POWDER BED FUSION PROCESSED 17-4 PH STAINLESS STEEL AS A FUNCTION OF POWDER CONDITION

Approved by:

Dr. Christopher Saldana, Advisor
School of Mechanical Engineering
Georgia Institute of Technology

Dr. Ramesh Ramakrishnan
Delta TechOps
Delta Air Lines

Dr. Thomas Kurfess, Advisor
School of Mechanical Engineering
Georgia Institute of Technology

Dr. Katherine Fu
School of Mechanical Engineering
Georgia Institute of Technology

Date Approved: July 17, 2020

ACKNOWLEDGEMENTS

To begin I would like to thank Dr. Christopher Saldana for his guidance and insight over the last two years as my advisor. Thank you as well to the other members of my reading committee including my co-advisor Dr. Thomas Kurfess, Dr. Katherine Fu, and Dr. Ramesh Ramakrishnan. I would also like to acknowledge the consistent support from the study sponsors and collaborators on the Delta Air Lines additive manufacturing team – Karthik Adapa, Donnell Crear, Jaikp Mallory, John Robertson, and Ramesh Ramakrishnan. There are several other persons who provided technical support and guidance at points including Dr. James Collins (mechanical testing), Elliott Jost (CT scans), Matthew Carroll (machining), Eric Woods (SEM and EDS), and Dr. Richard Cowan (fatigue results analysis). The staff of the Montgomery Machining Mall also have my thanks. I am very appreciative of my lab and office mates who make work a fun, interesting, and supportive place to be. Their influence and advice have been essential. This work was also supported in part by DE-EE0008303, NSF CMMI-1646013, NSF CMMI-1825640 and NSF IIP-1631803.

Thank you to my family, who has encouraged and supported me during my entire time as student. Thank you to Tali Cohen, who has been my irreplaceable teammate and partner.

TABLE OF CONTENTS

LIST OF TABLES

LIST OF FIGURES

LIST OF SYMBOLS AND ABBREVIATIONS

A1, A2, A3, A4	Additively manufactured builds/specimen lots/powder samples corresponding to the first, second, third, and fourth builds using the same powder feedstock supply
W1	Wrought specimen lot
p	Commonly used 'p-value' corresponding to the probability of Type I error of a statistical test
α	Commonly used significance value (such as 0.05 or 5%) used when computing a statistical test
X^2	Chi-squared statistic
β	Weibull distribution shape parameter
η	Weibull distribution scale parameter
γ	Three-parameter Weibull distribution location parameter, or the likelihood ratio depending on context
μ	Arithmetic mean, or log-mean in the context of the lognormal distribution
σ	Sample standard deviation, or log-standard deviation in the context of the lognormal distribution
ε	Strain
ε_f	Elongation or strain at failure
S_y	Yield strength
S_u	Ultimate strength
E	Young's modulus
S_{max}	Maximum stress level of a cyclic load
R	Stress ratio: S_{max}/S_{min}
f	Frequency of a cyclic load
N	Number of fully reversed loads
S-N, ε-N	Stress or strain versus number of fully reversed loads
N_f	Fully reversed cycles until failure
$S(x)$	Survival function, or probability of survival at value x
$P(x)$	Probability at value x
R_a	Arithmetic mean, or average roughness, of a profile as per ASME B46
S_a	Arithmetic mean, or average roughness, of an areal surface profile as per ASME B46
S_q	Root mean square of an areal surface profile per ASME B46
S_v	Maximum valley depth of an areal surface profile per ASME B46
ANOVA	'Analysis-of-variance' statistical test
DoF	Degrees of freedom, corresponding to an ANOVA
MS	Mean squares
SS	Sum of squares
F	"F" statistic, corresponding to an ANOVA test
PDF	Probability density function
CDF	Cumulative distirbution function
LPBF	Laser powder bed fusion
DMLS	Direct metal laser sintering

SLM	Selective laser melting
DED	Directed energy deposition
AM	Additive manufacturing
PM	Powder metallurgy
PH	Precipitation hardening
H900	Referring to the ‘H900’ condition as specified by AMS 5729/3G
H1025	Referring to the ‘H1025’ condition as specified by AMS 5729/3G
C.I.	Confidence interval
U.C.B.	Upper confidence bound
L.C.B.	Lower confidence bound
PSD	Powder size distribution
d_{10}	Diameter value at the 10th percentile of a PSD
d_{50}	Diameter value at the 50th percentile of a PSD
d_{90}	Diameter value at the 90th percentile of a PSD
L	Likelihood
θ	Parameter set corresponding to a model
MLE	Maximum likelihood estimation
t_{flow}	Flow time, corresponding to the Hall flowability test
γ	Austenite phase symbol
α'	Martensite phase symbol

ABSTRACT

The metal additive manufacturing process of laser powder-bed fusion (LPBF) presents a challenge to develop qualified processes to match the rapid pace of technology development. An aspect of the LPBF process where this applies is defining the how powder feedstock conditions affect the quality of produced components. This study examines how in-machine powder feedstock supplies evolve and are otherwise affected during the LPBF process, and how these effects impact subsequent builds which use said feedstock. An examination of powder flowability, rheology, and morphology is conducted to characterize the powder conditions. To study the effects, an assessment of produced component tensile, fatigue, and microstructural properties is conducted. Fatigue life is analyzed using a reliability modeling approach in order to provide detailed statistical conclusions often missing in other analyses. Powders are found to evolve their characteristics over exposure to repeated LPBF processes, particularly in the extremes of powder size distribution and measures of bulk flow. No significant effects on microstructural, hardness, tensile, and fatigue properties of the produced components are shown. Fatigue life is discovered to exhibit a dependence on spatial origin of the produced component. Additionally, a detailed characterization of the scatter in fatigue life typical to the process and material is provided.

INTRODUCTION

1.1 Problem statement

Metals powders are an integral part of the laser powder bed fusion (LPBF) manufacturing process in their role as the feedstock material. The lack of fundamental measurement science behind quantifying the morphology, chemistry, and microstructure of powders has been clearly identified by the additive manufacturing community [1], [2]. The evolution of in-machine powder supplies, used over the course of one or several builds, is an unstudied condition of powder. This evolution of powder condition is related but not identical to better studied practices such as powder recycling and extended environmental exposure which are known to lead to changes in powder characteristics [3]–[5]. Even in the case of these practices the links between powder and the effects on produced component quality are not fully understood. In particular, fatigue in LPBF produced components as a function of powder condition requires more in-depth study in addition to a generalized characterization of fatigue typical of the LPBF process and associated material systems. This work will address the unstudied case of in-machine LPBF process exposed powder via direct study of the powder, examination of produced component quality, and development of a detailed understanding of fatigue properties typical of the process and powder conditions.

1.2 Thesis organization

This thesis is organized into 5 chapters: *Introduction*, *Background*, *Methodology*, *Results and Discussion*, and *Conclusion*. In Chapter 2 provides context for metal powder use in AM along with a review of current challenges in qualification of powder feedstocks

in LPBF. Additionally, a review of relevant material fatigue properties is provided. Chapter 3 details the experimental methods used to characterize the sampled powders, assess the mechanical and microstructural properties of the produced specimens, and analyze and compare specimen response to fatigue. Chapter 4 presents the corresponding experimental results, a statistical analysis of powder and mechanical properties, and interspersed accompanying discussion as to the significance of the results. Chapter 5 provides a summary of results and the conclusions drawn from them. Contributions to the field are defined and opportunities for future work are identified.

BACKGROUND

2.1 Metal additive manufacturing

Advancement of manufacturing technology plays a critical enabling role in the development of numerous other fields. Designs, concepts, and manufacturing process improvements that were previously unattainable are now approachable via additive manufacturing (AM) which has recently captured the attention of industry, academia, and government alike when it comes to enabling new and groundbreaking development across a number of fields. Metal AM, specifically, is of interest due to its use of high-performance engineering materials. As opposed to traditional subtractive manufacturing techniques which remove material from a bulk to form the desired end-component, metal AM fuses, sinters, or bonds small units of raw material together, frequently in a layer-wise strategy, to create a component that is of the final desired geometry or near-net shape.

Laser powder bed fusion (LPBF) has emerged as a metal AM process which surpasses others in terms of attainable geometric precision, end-product density, process flexibility, and mechanical properties [6]. LPBF utilizes powdered metals as the feedstock material, their small size enabling piecewise fusion of the particles into a whole. This process goes by several other names in industry including direct metal laser sintering (DMLS) and selective laser melting (SLM). Electron beam additive manufacturing (EBAM) is closely related, with the major difference being the heat source utilized for fusion. While some of these common names imply a piece-wise sintering process it should be noted that LPBF is a true fusion process, creating near fully solid components from a

feedstock material that was fully melted before solidifying. The core mechanics of the LPBF process are described in Figure 1, where a prototypical process is shown.

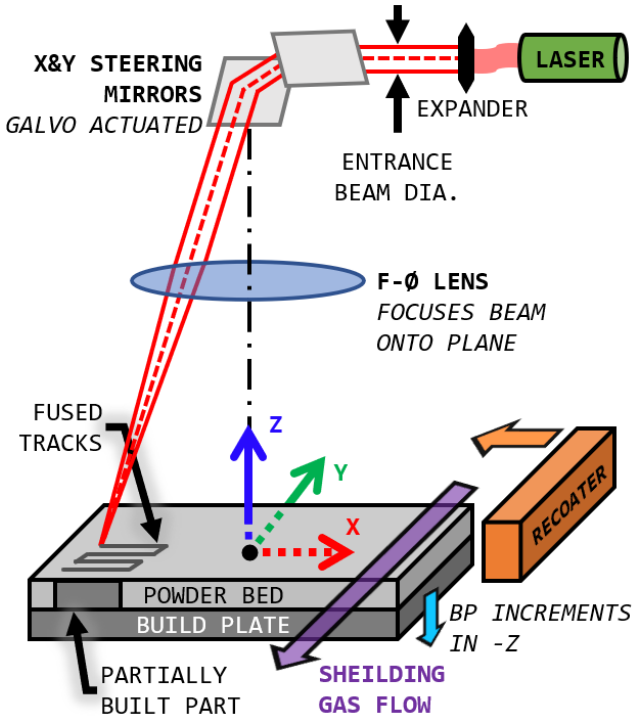

Figure 1. The prototypical laser powder bed fusion process. Gas flow and recoat directions may differ between respective machines. The origin of the coordinate system is normally defined off the top of the build plate.

The process proceeds as such: a thin layer of powder is spread over the build area by a recoating mechanism, most often a simple blade or straight edge. Galvanometer actuated steering mirrors direct a high-intensity laser, normally well over 100 *W*, through an optic and onto the build plate. The optic, an F-theta lens, focuses the beam to a consistent spot size on the build plate regardless of its X and Y position. The laser fuses a selective portion of the first powder layer to the sacrificial build plate. The build plate is lowered an amount known as the layer size, typically 20-80 μm, and the process is repeated. This continues incrementally, with selective portions of the powder bed corresponding to 'slices' of the final component geometry being fused to the previous layers until the desired geometry

has been achieved. The local fusion process, though at a small scale, is directly analogous to well-known welding processes such as laser welding although process speed, energy density, and thermal patterns do differ [6]–[8]. A shielding gas is flowed across the build area to protect the process zone from oxidization and remove byproducts.

Due to this methodology, metal AM provides a litany of advantages that enable designs, materials, and production practices that could yield significant benefits in many applications. Design freedom is offered via the layer-wise fabrication technique, allowing for components with internal cooling/fluid channels, novel light-weighting techniques, designs of a 'generative' origin, and structures that utilize 'meta-materials' such as lattices which can offer unrealized mechanical performance [9]–[11]. In the area of materials advances, metal AM offers increases in particular tensile performance metrics over wrought materials (in-part due to the nature of the high-power density solidification process), tailored materials properties, and gradient material properties [12]–[14]. Some results of these primary differentiators of metal AM are: reduced development time and design iteration overhead, more affordable realization of customizable/optimized designs, light-weighting/improved component mechanical performance, and 'distributed manufacturing' processes that can be utilized to increase supply chain robustness [15]–[17]. Much of the heightened interest surrounding metal AM in both popular press and academic literature has focused on these topics, however metal AM methods are not without their limitations. As compared to conventional subtractive processes and even some near-net-shape processes, metal AM produces less geometrically precise, rougher, less dense, and more defect-prone components [14], [18]–[20]. The potential benefits of metal AM cannot be reaped unless an advanced set of process qualification techniques can

be implemented [2], [21], [22]. Metal AM components offer great advantages under nominal and idealized conditions, but the process is inherently prone to defects such as porosity, unrepeatable material properties, and geometric uncertainty [18], [20], [21]. Due to these issues, demanding fields such as aerospace, medical, and automotive will not be able to adopt metal AM processes to their fullest extent without the technology to ensure process control and produced component quality [10], [23].

Qualification techniques applied in recent years are broad in their scope and method and encompass AM machine qualification [24], in-process monitoring [25], [26], and produced component destructive [27] and nondestructive evaluation [28], [29]. Although a large amount of work is focused on process and end-product qualification, control of the raw materials used by AM have been receiving heightened attention. Many commercial and cutting-edge metal AM techniques utilize powdered metals as the raw or feedstock material in the fabrication process. This includes LPBF process in addition to 'powder-fed' processes such as directed energy deposition. The question arises, how does powder feedstock affect the metal AM process and the produced components? Further, what features of the powder feedstock determine powder behavior in AM processes such as LPBF, and consequentially produced component behavior?

2.2 Powder feedstock use in LPBF

2.2.1 Powdered metal technology

Powdered metals are not a feedstock material form unique to metal AM. The field of "powder metallurgy" has existed for quite some time, with commercial uses of the technology beginning with difficult to process refractory metals such as tungsten in the late

1700s [30]. By the beginning of the 1900s the powder metallurgy (PM) process was in common commercial use in such applications. Also of note was the use of PM for processing of cemented carbides and porous bushings, bearings, and filters also in the early 1900s – PM is still used in these applications today [30], [31]. PM has since been used with conventionally difficult to process metals such as tool steels, superalloys, and the aforementioned refractory metals and cemented carbides [30], [31]. In addition, PM has proven to be an attractive route for economical processing of high production components with complex geometries [32]. For such applications sintering or metal injection molding (MIM) has been used in combination with powder feedstock material to create a near-net-shape component. It should be noted that powders have also been used in thermal-spray and welding applications for quite some time, where powders take the place of the normal wire or rod-shaped filler materials [31], [32].

Historical uses of PM, welding applications with powdered metals notwithstanding, have generally relied on compaction of the feedstock material in combination with heat to form the produced components. Use of powdered metals in freeform fabrication processes, now more commonly termed as additive manufacturing, differs in this aspect since it relies primarily on a repetitive small-scale welding process that does not create compaction or densification due to application of pressure [33]. Post-procession methods such as hot isostatic pressing (HIP) may be applied to AM components, though [34]. In particular, the AM processes that rely on powdered metal feedstock materials either insert powders into a meltpool (powder-fed) or locally fuse portions of a spread powder layer (powder-bed). Powder-bed applications include the quite common LPBF and EBAM processes, which are essentially the same in process structure with differences in the associated heat source

that drives the welding process. They may both be referred to as powder bed fusion methods. Powder-fed applications include directed energy deposition (DED), which involves a similar constitutive welding process albeit with directed addition of powder instead of a powder bed [35]. These various methods go by many trade names, and together make up a very large portion of the metal AM technologies currently utilized in industry. Amongst the similarities they share is the use of powdered metal as the feedstock material.

2.2.2 Measurement science for powders

Given the significant history of PM in industrial applications, methods for measuring metal powders were developed prior to modern AM applications to allow for quality control of feedstock materials. In a production environment especially, measurement science gains utility when based in standardization of materials specifications and test methods. The three most prevalent standardization bodies currently issuing standards in the field are ASTM, the Metal Powder Industries Federation (MPIF), and the International Standards Organization (ISO) [36]. Issued standards generally cover either material specifications or test methods. While important in the further advancement of powered metals in AM, a review of efforts to standardize material specifications is not focused on here. Test methods which provide standardized measurement techniques used to define aspects of powder that can be applied to powders regardless of material or type are given a greater focus.

While the body of standards in existence is quite large, there is an unfortunate dearth of relevant test methods for applications in the metal AM field exists. The majority of historically issued standards apply to more classical PM methods or end-products [36].

Many test methods are strongly rooted in the processes used in classical PM production methods [36]. This is an issue, especially in the context of the emerging focus on process and end-product qualification in AM. With its many high-performance applications and acknowledged propensity for quality control issues [16], [32]–[34] powder qualification has been identified as critical [2], [37], [38]. Further, qualification processes must be built on well-vetted and trusted methods if they are to be adopted and used to their maximum potential [1].

Leaders in measurement science and AM have clearly identified this gap. The National Institute of Standards and Technology (NIST) has been tasked by the Department of Commerce with identifying challenges to the industrial adoption of AM. Their *Measurement Science Roadmap for Metal-Based Additive Manufacturing* has clearly identified weaknesses in powder characterization, lack of standardization in AM-specific characterization techniques, and missing correspondence between powder and produced-component quality as major areas critical to metal AM at large [37]. Similar conclusions have been drawn by other road-mapping efforts, including one from the Consortium for Additive Manufacturing Materials (which dedicated an entire thrust area to "Part and Feedstock Testing Protocols"), and the NSF/ONR funded *Roadmap for Additive Manufacturing* developed by the leading organizers and contributors to the AM-focused yearly conference, the *Solid Freeform Fabrication Symposium* [2], [38].

Sutton et. al. provide a well-informed breakdown of powder properties and their existing characterization methods. Powders are said to be constituent of morphological, chemical, and microstructural properties [39]. Morphological properties include particle size, shape, and surface texture. Particle size characterization can be accomplished via a

crude sieving analysis, microscopy, or light diffraction [39]. Light diffraction offers the best sampling capabilities of the three but does not have the ability to characterize particle shape as all particles are treated as spheres to calculate their equivalent spherical diameter [3]. Particle chemistry can be evaluated through a gauntlet of well-known analytical methods (some challenged in expense, time, and precision) with combustion analysis notably providing a very rapid and precise measure of several elements [3], [39]. Microstructure includes internal porosity in addition to the arrangement of crystal structures within individual powder particles which can be evaluated via the conventionally methods used in metallography [39]. One other important category of powder characteristics would be what is sometimes termed as 'bulk behavior' which includes various measures of density and fluid behavior. There exists a litany of test methods and metrics in this area, many tied to specific functionalities of interest in industrial fields. It must be made clear that many terms exist to describe the fluid-like behavior of powders and they are often used interchangeably. For the purposes of this study 'flowability' refers to the mass-flow rate of powder flow under its own weight (measured by tests such as Hall flow), while terms such as 'cohesivity' and 'resistance to shear' specifically describe properties derived from shear tests of powders. Non-cohesive powders are also free flowing. The property measured by basic flow energy (BFE) is derived from a dynamic flow test?

Several authors have expounded on these needs in recent years. Anderson et. al. focused on powder internal porosity as a result of mushy-zone solidification physics, powder agglomeration and satellites, surface impurities inherent to powders in their directly manufactured or 'virgin' state, and how these defects can create porosity in the

produced AM components [40]. Slotwinski, Garboczi, and Jacob of NIST have made extensive comments on the broad metrology needs for metal AM powders across several works [1], [3], [41]. Their focus is on the need for traceable data that can be relied on with confidence to create definitive process controls. They point out the weak connection between powder size distribution (PSD) and the outcomes of the AM process, as well as the disagreement between powders with nearly identical PSDs that register as vastly different when characterized via other methods such as flowability and rheological tests [1]. A critical conclusion is that the all-important PSD characterization often held up as the defining powder characteristic is only a part of the overall powder characterization challenge. Amado et. al. pointed out that a review of the literature has shown a severe lack in methods applied than can quantitatively describe particle shape [42]. Amado studied plastic powders for selective laser sintering, but makes highly relevant comments about the lack of AM-process rooted tests that measure powder spreadability over the build area and proposes a conceptual test method that would address this gap in existing test methods [42]. Notably, the factors that contribute to the physics of spreading a powder bed are complex and not fully understood. The most prominent metrics in use to consider would be Hall flowability, basic flow energy (BFE), and multiple aspects of the dynamic flow behavior (rheology) including flow function, cohesivity, and resistance to shear. The metrics are subtly distinguished, complex, and observed behavior can be the result of many constitutive powder properties [43].

Standardization in some of the morphological, chemical, and microstructural efforts exist, but a thorough review here would be out of the scope of this work. Drake provides a detailed review that can be referenced, as does Senthilvelan et. al. [44], [45].

The important standards to note are those that govern PSD evaluation by light diffraction and image analysis, chemical analysis via combustion, and apparent, tap, and bulk density [46]–[49]. The list of methods for measuring various forms of density is quite long and not provided here. Also of note is the ASTM standard on powder sampling which has a strong pedigree based on applications of sampling feedstock materials in the PM field and is actually quite applicable to generalized purposes [50]. This standard is heavily utilized for the sampling of powders in AM. Some of the prominent methods of testing powder fluid behavior that have standards behind them are the Hall flowability test and the FT4 rheometry test (or shear cell test) [51], [52]. Both tests are rooted in powder processing techniques utilized in more conventional PM processes, and neither has a very direct physical relation to the mechanical processes undergone by powders in the LPBF process [42].

2.2.3 Powder feedstock characterization efforts for LPBF

Many efforts in powder characterization and powder effects on produced components have been motivated by the practice of powder recycling. Metal AM processes that utilize powder feedstock are characterized by low material usage efficiency and high material cost at the moment which together present a need for recycling practices [53]. Industrial practices exist for recycling powder which utilize a simple sieving process to remove both particles larger than desired (such as multiple particles fused together during the preceding build) and occasionally particles too fine for use. This removes large, non-spherical, and typically compositionally impure particles that decrease packing density [54]. Often though, machine operators engage in sieving practices to simply try to match virgin powder PSDs out of the simple motivation to not diverge from origin manufacturer

specification. This all said, this practice is still on the edge between the research stage and full-scale adoption and only users that have decided they can accept the potential loss of control over powder quality engage in this practice currently [1], [39]. Established process controls for identifying when powder has reached the end of its recyclability are sparse and certainly not standardized [41]. Due to this application of powder recycling the earlier discussed measurement science techniques and lack thereof have been studied in quite a large amount of recent work in the LPBF field.

Slotwinksi et. al. presented the results of a suite of characterization methods that were aimed at several powder types, including a 17-4 stainless steel powder [3]. Helium pycnometry, light diffraction, XCT, XRD, EDS, and XPS were all utilized. A novel technique of CT imaging of powders suspended in epoxy provided an extremely data-rich evaluation of powder morphology that included information about powder size and correlated data on powder shape. XPS did not uncover significant changes in elemental content and XRD showed a small increase in the amount of retained austenite in the 17-4 powder with degree of recycling, attributed to the powder's exposure to heat during previously experienced LPBF process conditions. Measurements of PSD via light diffraction offered an interesting insight into the recycling practice. The recoating process is identified to preferentially transport larger particles across the build area and into the powder collector [3]. Sieving is observed to largely restore powder to a PSD similar to that of virgin powder. A gradual increase the 90^{th} percentile of particle diameter, or d_{90} in conjunction with degree of recycling is also observed. This is primarily attributed to smaller particles adjoining to larger ones during the LPBF process, creating agglomerates which are not filtered out by sieving due to their elongated shape [3]. A companion paper

by Luecke and Slotwinski covers an evaluation of mechanical properties of components produced with virgin and recycled powders [55]. These components are treated with a stress-relieving heat treatment not strictly designed to harden the material via to solutionizing and aging. They note a significant departure in mechanical properties between AM and wrought materials. A hardness mapping effort does not discover any variation in mechanical properties related to location on the build plate. Evidence is found for a significant amount of retained austenite in the nominally martensitic 17-4 specimens.

Heiden et. al. have also conducted a thorough study of 316L stainless steel powder characteristics as a function of degree of recycling [4]. In agreement with Slotwinski et. al., they observe greater sphericity in virgin powders and an increase in satellites and irregular shapes in recycled powders. Heiden also notes a disagreement between PSD measurements attained by laser diffraction and SEM image processing, but both methods confirm a relatively minor change in PSD with recycling indicating an effective sieving process. Elongation to failure of built components appears to decrease with degree of recycling. Other authors have observed similar results [56]. Yield and ultimate strength do not change with degree of powder recycling. Large oxide particles are discovered in the recycled powder and also seen in the fracture surfaces of the tested specimens. Several other powder studies on powder recycling have produced a largely harmonious set of results. PSD and tensile properties (with the exception of elongation at failure) are observed to not be greatly influenced [5], [41], [57]. Flowability and apparent density changes are seen to both increase with degree of recycling [5], [41], [57]. These results are observed in several material systems including titanium, nickel-based, aluminum, and stainless-steel alloys.

The AM community has realized the importance of measures of bulk powder fluid behavior, as they can often reveal powder differences that other tests do not, but simultaneously the difficulty of applying them has become evident [39], [42], [43], [56]. Applications of relevance include two powder recycling studies that have observed the greater permeability of virgin powders, measured by pressured drop of a gas passed through them, and attributed the finding to a higher content of agglomerated particles that reduce packing density (recycling was seen to remove agglomerates via sieving) [57], [58]. This does not strictly match conclusions of other authors who have noted that virgin powders tend to be more spherical. In this case, the lack of agglomerates was concluded to mean greater flowability. In the first study this accompanied a higher basic flowability energy (BFE) and in the second the highest cohesivity, both indicators of a less free-flowing nature. In both cases more permeable less cohesive recycled powders showed better mechanical properties attributed to higher quality and denser powder beds. Importantly, flowability behavior (specifically when measured via the more direct method of Hall flow) can be distinct from measures produced by a powder shear test such as BFE and cohesivity measurements in some cases [43]. In a case study published by Clayton et. al. BFE, which is the energy required to displace powders during forced flow, is connected to higher packing and better cohesion of particles during a shearing behavior such as spreading. This claim is notably opposite to correlations established by the authors of both powder recycling studies [57], [58]. Strondl et. al. has also characterized the results of powder recycling in terms of fluid behavior, and in an EBM application found that virgin powder packed best and had a lower BFE while in an LPBF application it was recycled powder that packed better and had a higher BFE [56]. These opposing results imply that

even a powder condition evolution theorized to be similar in two cases did not produce the same fluid behavior results. To sum up, the measurement of powder fluid behavior in relation to AM is still developing, few consistent trends have yet been identified, and many powder properties cannot be consistently expected to trend together.

Studies on the aspects of 17-4 powder and the produced components have produced results that run in contrast to what might be expected of the conventionally processed alloy. The content of the powder and the as-built components is observed to contain significant amounts of retained austenite [41], [59]–[61]. This is explained by the extremely small austenite grain size present in both powder particles and fused portions of a build formed as a result of rapid cooling from their super-heated states [60]. While the composition of 17-4 would normally dictate that this austenite transforms to martensite as the powder particles and fused components cool, the extremely small prior austenite grain size inhibits the kinetics of the phase transformation [62]. This presence of retained austenite is also suspected to possibly inhibit the precipitation of copper rich particles during the aging process that hardens and strengthens the alloy [59]. Processing atmosphere conditions are also noted to affect the produced alloy phase composition. Both nitrogen and argon are commonly used as atmospheres for producing of powders via gas atomization and shielding gasses in LPBF processing of 17-4 powders. Nitrogen atmospheres are observed to contribute heavily to more austenitic microstructures while argon atmospheres produces a mostly martensitic microstructure [59], [63], [64]. Powders atomized in nitrogen gas will that are used in an LPBF that uses an argon atmosphere will produce a mostly martensitic end-product, though. This is attributed to the roughly four-times lower conductivity of

nitrogen gas as compared to argon gas [63]. Nitrogen, if incorporated in the alloy, is also an austenite stabilizer.

Linking powder properties to produced component properties remains a challenge for the field. Many studies have been published that either strictly evaluate changes in powder during recycling or assess mechanical and microstructural properties of produced components, but rarely are both aspects considered together. A small number of significant works (many of which have been reviewed here) have been conducted that perform the two assessments in parallel and can provide a few strongly evidenced correlations between powder and parts [4], [5], [41], [55], [57], [65], [66]. Notably, the work is spread out over several material systems, among them Ti-6Al-4V, Inconel 625, Inconel 718, and 17-4 PH. More work is required to better elucidate the dependent relationships proposed. Rheological properties of powder have rarely been studied in conjunction with properties of produced components. Powder chemistry is often evaluated by methods that lack precision. Further, it should be noted that a somewhat narrow definition of powder recycling has mostly been investigated, and several other powder conditions of interest deserve greater attention. Finally, the effects of powder on fatigue properties of produced components has received very little attention, with only a handful of studies, which are reviewed in the following sections, devoted to this possible effect.

2.3 Fatigue in LPBF produced components

2.3.1 Approaches to assessing fatigue performance

The nature of powder condition effects on produced components discussed thus far gives rise to questions about the possible effects on fatigue. Various treatments and

conditions of powders have been shown to produce disfavorable phases in microstructures, oxides that could be incorporated as incoherent second-phase inclusions, and conditions that favor porosity. Although it has been shown that the impact on tensile performance has been negligible each of these changes are established suspects that lead to premature failure in fatigue [67]–[69]. Fatigue failure is of great interest in many fields due to its roll in well over 50% of in-service failures [70]–[72]. In order to address this problem researchers and product developers engage in the practice of fatigue testing which has long been acknowledged as a time-intensive and expensive experimental effort [70], [72]. Testing can be summarized to accomplish one or more of several common goals [72]:

1. Extract information that yields actionable design knowledge.
2. Compare distinct materials or processing methods by determining their respective impacts on fatigue response.
3. Identify root causes that lead to failure in fatigue.

Multiple test methods exist that evaluate fatigue. They may largely be considered to fall into two categories: evaluation of fatigue life, and resistance to crack initiation and growth under specified loading conditions. Both methods can produce complex data sets where a resistance to fatigue, whether expressed in terms of fatigue life or crack growth, is represented over possibly several loading conditions. Experimentally observed fatigue life, often measured as number of loading cycles, is a highly stochastic property exhibiting coefficients of variation of 25-75% [71], [72]. It has been acknowledged that AM process-induced defects are particularly responsible for very high degrees of scatter in fatigue properties [69]. Frequently, when fatigue life is investigated a set of several loading conditions are examined. For uniaxial, bending, or rotating bending fatigue tests, different

regimes of fatigue life are often targeted for evaluation, broadly described as high cycle fatigue (HCF) and low cycle fatigue (LCF). These regimes correspond to low load amplitudes that lead to failure in roughly 10^5 cycles or greater (HCF) or higher load amplitudes that lead to failure in roughly 10^4 cycles or fewer (LCF). For design purposes it is valuable to express fatigue life over a spectrum of low-to-high cycle fatigue, providing life expressed in number of loading cycles (N) as a function of applied load or stress (S) forming a *S-N* curve [70], [72]. S may sometimes be replaced with strain should testing be conducted in a situation where strain is the driven variable (not applied force) forming a ε-N curve.

S-N curves provide valuable design information but are difficult to use for comparing materials or material processes due to their complex form, difficulty to describe deterministically, and the natural stochastic variation in fatigue life [71]. A very large number of tests conducted at varying stress or strain levels is required to form the curve, and a difference in variation at different stress/strain levels is expected, forming a heteroscedastic phenomenon, depicted in Figure 2Figure 1, where fatigue life variation increases as tests proceed from the LCF to HCF regimes. Some statistical tools exist to analyze *S-N* curves, notably ASTM E739 which describes the statistical description of linearized *S-N* or ε-*N* curves [73]. This method has multiple weakness – first data must be well described by a simple linear relationship that relies on taking the log of stress (or strain), or both stress and life. Second, the primary method of comparison between curves available involves a visual comparison of curve confidence bounds. Confidence bounds will be very large throughout the curve unless a very large number of tests is conducted at each level.

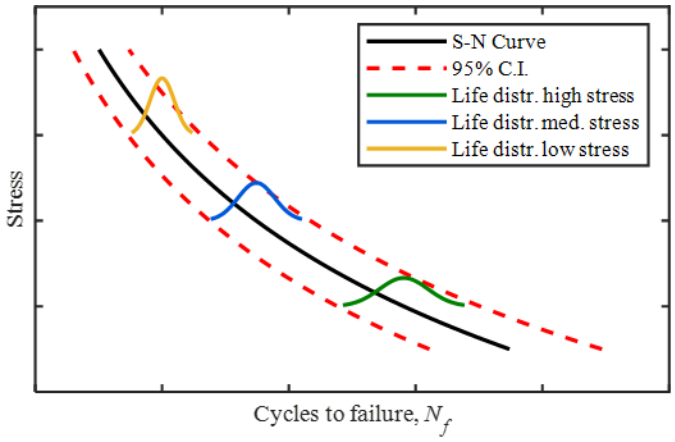

Figure 2. A simplified visualization of typical heteroscedastic behavior displayed in fatigue life. PDFs of an arbitrary distribution type are superimposed over the S-N curve at various stress levels to model increase in fatigue life variation as the stress level decreases.

An alternate method of comparing fatigue life between materials or manufacturing processes utilizes methods broadly described as reliability modeling. Simply put, these methods are generally pointed at a single measure (e.g. fatigue life), under a single set of service conditions (e.g. stress, strain). Methods for comparing reliability are varied and robust. They generally fall into two categories of statistical analysis – parametric and non-parametric. Wirsching and collaborators have provided a strong description of these methods applied to structural fatigue across multiple works [71], [74], [75]. Parametric methods used to model fatigue most frequently utilized the lognormal, Weibull, or three parameter Weibull probability distributions functions (PDF) to have long been used model fatigue life [75]–[77]. Modern applications are widespread, with common use of these methods in fields where manufacture methods are prone to defects, e.g. casting or composites, and applications of high demand and cost of failure [78]–[80]. Importantly, these methods provide for comparisons between models with definitive statistical tests [81], [82]. Simply put, conducting fatigue tests at a single or very select number of loading conditions can produce a large sample size which lends itself to robust statistical analysis.

This comes at the cost of not providing a description of fatigue properties useful to designer beyond the narrow band of loading conditions investigated but allows for a more conclusive answer of whether treatments produce a difference or lack thereof in fatigue life.

2.3.2 Prior work on fatigue of LPBF components

The body of work dedicated to describing fatigue in LPBF processed 17-4 PH stainless steel has been growing in recent years due to the popularity of 17-4 PH as a high strength corrosion resistant alloy that is more cost effective and safer to handle than nickel-based super alloys and titanium alloys (which are somewhat less tough than 17-4 PH). In addition, relevant work in other material systems has also been published. The effects of multiple aspects on fatigue have been investigated, including surface roughness and condition, internal porosity size location and shape, and heat treatment.

The basic metallurgy of 17-4 PH is worth a brief discussion to establish a context for decisions on heat treatment and microstructure, which greatly affect fatigue. 17-4 PH is also frequently referred to as just ‘17-4’, as it is here, and known technically as both grade UNS S17400 and AISI type 630. 17-4 is a stainless steel and thus Fe-based, with a significant content of Cr (~17%) and Ni (~4%). The alloy also contains roughly 4% Cu and less than 0.1% C. Ni content is kept low in order to avoid creating an austenitic microstructure at room temperature, as Ni is an austenite stabilizer. This means 17-4 does not have the high Ni content that boosts corrosion resistance in stainless steels such as 316, and to compensate Cr content has been raised far past the 12% threshold required to create the protective Cr-film of stainless steels. Corrosion resistance is preserved, though 17-4

does not compare to more corrosion resistant austenitic and duplex stainless steels without as much carbon. Importantly, the high chromium content also increases the hardenability of the alloy, raising the martensite formation start and finish temperatures. In order to be hardened, C is added to both extend the γ-loop (allowing for austenite formation at high temperatures) and to provide the necessary interstitial alloying required for martensite formation upon quenching. Together, the Cr and C content leads to a $\gamma \rightarrow \alpha'$ transformation upon cooling from a sufficiently high temperature. Normally air quenching produces sufficient cooling rates to accomplish this. It should be noted that the martensitic transformation is not the primary hardening method for 17-4. Cu, dissolved in the matrix, provides the opportunity for precipitation hardening, which is the dominant mechanism for raising hardness and strength in 17-4.

17-4 PH industry standard heat treatments are defined by an Aerospace Materials Specification (AMS) of SAE, which provides the standard for heat treatment of the alloy in industry [83]. Heat treatment is performed in two steps: solutionizing and aging. Solutionizing raises the alloy to a high temperature for a sufficient time to produce a fully austenitic microstructure and suspend all alloying elements, Cu in particular, into solid solution. Upon quenching, the Cy is trapped in a super-saturated solid solution. The alloy can now heat treated to varying degrees of hardness and strength by aging, which facilities the rejection of Cu by the matrix through precipitation of Cu-rich particles due to by exposure to intermediate temperatures. These precipitates accomplish higher hardness and strength by acting as impediments to dislocation movement and are the reason for the PH (precipitation hardening) term being sometimes included in the colloquial alloy name. As with most PH alloys, 17-4 PH is frequently utilized in its peak-aged state where the Cu-

rich precipitates are very fine and near-fully coherently incorporated in the matrix producing peak yield and hardness properties. This condition is referred to H900, referring to 1 hour of aging at 900 °F [482 °C] after solutionizing. 17-4 is also utilized in slightly over-aged conditions which can produce a mix of coherent, semi-coherent, and incoherent precipitates that promote strength in combination with ductility and toughness.

Given the unique processing history of LPBF processed 17-4 components, several researchers have studied which heat treatments most positively affect the alloy in regard to fatigue performance. Yadollahi et. al. performed multiple tests on as-built and H900 condition 17-4 specimens and identified that fatigue crack growth (FCG) behavior in LPBF manufactured 17-4 was not dependent on heat treat state [84]. Yadollahi also claimed that the large internal pores present dominated the material's response to fatigue and as such the conventional H900 condition did not produce more favourable fatigue properties as is expected in wrought material. Nezhadfar et. al. studied 17-4 heat treated to various conditions, and identified the H1025 condition as producing the best HCF life [61]. The solutionizing step of the heat treatment process was deemed to be critical as it removed defects in the as-built microstructure [85]. Multiple other researchers have noted this detail and have investigated condition H1025 17-4 to study optimal fatigue properties of the material [58], [86].

Several researchers have attempted to identify defects that drive fatigue performance. Surface condition is the most critical aspect of a structure in fatigue, and it has been broadly concluded that the rough, as-built surface condition of LPBF manufactured 17-4 will drive failure in fatigue [22], [69], [85]. Should as-built surfaces be removed or altered by secondary processing steps, it was found that defects of a sufficient

size, especially ones that fall in a sub-surface region, drive fatigue life [22], [84], [86]. These secondary manufacturing steps remove both surface defects and sub-surface internal porosity which is generally of greater concentration and severity in LPBF manufactured components [87]. These defects, if large enough, do not require any crack incubation period and thus fatigue life is defined by crack growth. It is noted that builds with this sort of significant porosity will not be greatly influenced in their fatigue life no matter the heat treat condition they are tested in [84]. Build orientation has been studied as well, with Yadollahi, Nezhadfar, and others consistently finding that orienting build direction perpendicular to the direction of internal stress increases fatigue life throughout the fatigue spectrum [61], [84], [88], [89]. This can be attributed to the lower projected area of lack-of-fusion (LoF) defects onto the stressed cross-sectional areas in this configuration. It was also concluded that build orientation did not greatly affect fatigue crack growth (FCG) rate or directionality [84].

Studies of fatigue as a function of powder characteristics have only been performed very recently and are few in number. Carrion et. al. studied powder recycling effects on the tensile and fatigue behavior in LPBF manufactured Ti-6Al-4V [57]. Reported powder measurements agree with the earlier presented works and show a narrowing of PSD due to a depletion of small particles as a result of recycling. This is correlated to increased flowability but, critically, Carrion points out that a narrowed PSD with fewer small particles and higher flowability contributes to lower powder bed density and commensurate increased part porosity. This suggests a possible ‘sweet-spot’ in flowability conditions, when weighed against other findings. Exposure to humid conditions is noted as influencing particle agglomeration, thus lowering powder flowability. Oxygen pick-up, due to

atmosphere exposure, is suspected based on prior work [90]. Carrion does not observe produced component microstructure changes as a result of recycling. Fatigue testing on specimens produced with virgin and recycled powder show no noticeable difference in LCF, but results in HCF, notably with high scatter, may show better performance for recycled powder manufactured components. Carrion points to flowability improvements as result of narrowed PSD as more important to determining powder bed density than the ideal packing density that might be attributed to a wider PSD.

Only one work known to this author has studied fatigue behavior in stainless steels as a function of powder characteristics. Soltani-Tehrani et. al. studied fatigue in LPBF manufactured 17-4 that was built with virgin and recycled powders in a nitrogen atmosphere [58]. Highly recycled powders are observed to show improved flowability and less compressibility due to a reduction in fines and agglomerates which agrees with the prior work. In agreement with Carrion, Soltani-Tehrani observes improved fatigue life for specimens manufactured from highly recycled powders. The causes of this are suspected to be complex. While a narrowed PSD increases flowability a reduction in fines might also cause powder agglomeration which decreases the density of the spread powder layers. These two effects would run in contrast, and thus it is difficult to attribute fatigue property changes to a specific powder characteristic. The author also observes a trend otherwise not presented in the known body of work – fatigue life dependence on built plate spatial origin. Components built further in the direction of recoat exhibited longer lives.

Although the efforts of multiple researchers have established a benchmark for fatigue in LPBF manufactured metals such as 17-4 and in some cases connected fatigue performance to attributes of the powder feedstock material there exists multiple weakness

and gaps in the prior work. Many investigations into fatigue have focused on the effects of large detrimental defects of the sort that may not be present in a well-controlled, monitored, and optimized production process. This means ideal service conditions of LPBF components have been understudied. Quite a few studies have conducted work in disagreement with best practices for fatigue testing, utilizing test specimens with machined or polished surfaces that do not meet guidelines designed to remove confounding factors from fatigue testing. This may not be of great importance, though, due to the more severe defects present in AM materials as compared to wrought materials. Of the small body of work that has examined powder condition effects on fatigue, a number of complex and interacting phenomena are observed, and clear conclusions are difficult to draw. Finally, many researchers have made conclusions based on relatively small sample sizes and have not made comparisons using rigorous statistical methods.

METHODOLOGY

3.1 Powder use methodology and specimen manufacture

3.1.1 Powder use methodology

In order to fully define a LPBF process, treatment of the feedstock metal powder must be carefully defined across the entire process. In this study, a specific set of powder handling and treatment conditions were examined. In summary, two methods of powder utilization were contrasted. The first method may be termed as direct use of virgin powder. Consider that a build is calculated to use 10 *kg* of virgin powder. Slightly more than 10 *kg* is loaded into the LPBF machine powder hopper directly from the sealed container supplied by the powder manufacturer. The LPBF machine is immediately prepped for a build, and the process chamber is flooded with an inert gas to minimize the exposure of the contents to atmosphere. Finally, a build is begun in a timely manner. Once the process is complete the build is removed, and the process chamber is cleaned of all remaining powder and by-products. Any subsequent builds would utilize virgin powder taken directly from the manufacturer-provided powder container in the same manner. In this manner the powder utilized for a build has had minimized exposure to any conditions other than those experienced during its original manufacture and the LPBF process that has produced the build it was directly utilized for. Exposure to atmosphere, handling conditions, and LPBF process chamber conditions has been minimized in aspects of both quantity and time.

The second method may be termed as repeated process exposure powder use. In this approach, four subsequent builds are planned. Each build has been calculated to use 10 *kg* of powder and slightly more than 40 *kg* of powder is loaded into the LPBF machine powder

hopper directly from the sealed container supplied by the powder manufacturer. The LPBF machine is immediately prepped for a build, and the process chamber is flooded with an inert gas. Once the first build is complete, the build process chamber is opened, exposing it to atmosphere. The hopper is covered with a sieve to protect it from undue contamination. The first build is removed, exposing the process chamber to contamination by the operator and powder from the build area, and new build plate is installed. The process chamber is flooded with an inert gas. The top layer of the powder hopper is swept into the powder collector by the recoater. The second build process is started, and the process is repeated until all planned builds (in this case four) are complete. In this situation powder is exposed to multiple potential channels of contamination and alteration increasing in aspects of both quantity and time linearly between the first and final builds. The powder used for the first of four builds is of the directly used virgin condition. The powder used for each subsequent build has evolved and is of the repeated process exposure condition with the second, third, and fourth builds being exposed to one, two, and three prior LPBF processes, i.e. various degrees of repeated process exposure.

This study compares these two powder conditions, directly used virgin power and repeated process exposed powder, through four consecutively executed builds as described above and detailed in Table 3. An assumption is made that these conditions are representative of operating procedures relevant to multiple LPBF machines and processes in-use. The first build, termed additive build 1 or A1, models virgin powder direct use. The subsequent second, third, and fourth additive builds (builds A2, A3, and A4) model various degrees of repeated process exposure conditioned powder. Figure 3 displays a graphical

explanation of how powder in the hopper of the LPBF machine is used for subsequent builds, and the overall LPBF process architecture.

Table 1. Analyzed powder conditions

Powder supply/build ID	Condition	Number of prior processes
A1	Virgin powder direct use	0
A2	Repeated process exposed	1
A3	Repeated process exposed	2
A4	Repeated process exposed	3

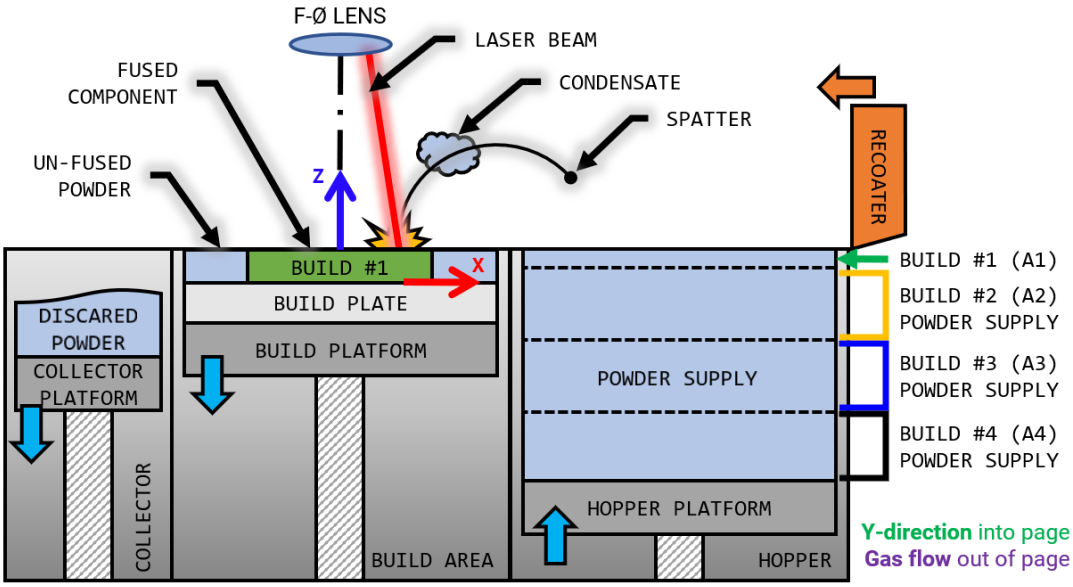

Figure 3. Depiction of the build process used for production of the tested and analyzed LPBF specimens. The powder hopper contains powder that will be used for four consecuitively executed builds. The hopper supply is not replenished or purposely altered between builds. Several methods of powder supply contamination due to the fusion process are depicted.

A precise description of the build operation procedures is provided below.

1. Load 80 *kg* of powder directly from the sealed manufacturer container to the powder hopper.
2. Collect a powder sample from the powder hopper.
3. Calibrate the laser: Command the laser to 100W. Calibration limits are ±2% of the commanded value.

4. Level the build plate.
5. Seal the process chamber and command flooding with argon.
6. Apply doses of powder until the build plate is fully covered with one layer of powder.
7. Execute the build. Powder quantity used is roughly 25 *kg*.
8. Once the build is complete, use the recoater sweep the top layer of the powder in the hopper over the completed build into the powder collector.
9. Open the process chamber, cover the hopper with a 75 μm sieve.
10. Remove powder from the build area into the powder collector. Remove the build plate.
11. Clean the process chamber of excess powder in the build area.
12. Install a new build plate.
13. Remove the sieve.
14. Repeat steps 2-13 for the three subsequent builds.

3.1.2 Virgin powder characteristics

The powder feedstock used in this study was procured from *Praxair Surface Technologies*, under the commercial product name of *Truform 174-l61* adhering to Praxair specification *ZFE276-L62BK*. This product specification conforms to the chemical composition specifications of *UNS S17400* in all aspects other than maximum allowable nickel content. The manufacturer lot-specific chemical composition analysis is provided in Table 2, along with the manufacturer and UNS specifications per ASTM A693-16 [91], [92]. Powder lot #1 of the provided specification was utilized, manufactured on August 17th of 2018. This powder was gas atomized in an argon atmosphere, as opposed to water

atomization or gas atomization in an atmosphere of another inert gas. Several additional powder measurements, reported in Table 3 with measurement method noted, were provided by the manufacturer. All measurements reported were taken on powders sampled per ASTM B215. Reported PSD measurements d_{10}, d_{50}, and d_{90}, refer to the diameter of the 10th, 50th, and 90th percentiles, by diameter, of the characterized sample, as per ASTM E1617.

Table 2. Chemical composition of 17- PH virgin powder

Element	Fe	Cr	Ni	Cu	Mn	Mo	Si	C	
Mfg. specification	Bal.	16.70 15.50	4.60 3.60	3.50 3.00	0.70	0.50	1.00	0.06	
UNS specification	Bal.	17.5 15.0	5.0 3.0	5.0 3.0	1.00	…	1.00	0.07	
Test result	Bal.	16.27	4.18	3.24	0.03	0.07	0.76	0.06	
Element	P	S	N	O	Sn	Al	Ta	Nb/Cb	Other
Mfg. specification	0.025	0.025	0.025	0.040	0.02	0.05	0.05	0.40 0.15	0.20
UNS specification	0.040	0.030				…		0.45 0.15	
Test result	<0.005	0.002	0.007	0.022	0.00	0.00	0.00	0.19	0.14

Units are [%]. Limits are a maximum unless shown as a range

Table 3. Manufacturer powder test results

Metric	Test method	Result	*Minimum specification	*Maximum specification
Hall flow*	ASTM B213	13.8 *s/50g*		
Sieve, +230†	ASTM B214	0% wt.		0%
Sieve, +270†	~	1% wt.		5%
Tap Density	ASTM B527	4.57 g/cm^3		
PSD, d_{10}	ASTM B822	25 μm	10 μm	
PSD, d_{50}	~	37 μm		
PSD, d_{90}	~	55 μm		55 μm
PSD, -16 µm‡	~	1% vol.		2%
PSD, -22 µm‡	~	5% vol.		

**Minimum and maximum manufacturer specification are provided only if specified.*
***Method 1 utilized.*
†Refers to the percent mass of the sample retained by the sieve, where #230 and #270 sieves have openings of 63 and 53 µm respectively, per ASTM E11.
‡Refers to percent volume of sample measured to be under the specified diameter.

3.1.3 Specimen design

Each build includes specimens intended primarily for either quasi-static uniaxial tensile testing, uniaxial fatigue testing, or microstructural evaluation. Two specimen types were designed to accommodate for these needs – a 'universal' as-built specimen design that can be post-processed to produce a specimen appropriate for either tensile or fatigue testing, and a 'witness' specimen for microstructural evaluation. The tensile specimen as-machined design corresponds to a standard sub-size cylindrical with a 6.0 *mm* gage diameter specimen per ASTM E8 [93]. The fatigue specimen design corresponds to the guidelines of ASTM E466 for cylindrical gage section specimens, and has a reduced diameter section of 6.0 *mm* [94]. Both designs are detailed in Figure 4. Specimen grip surface runout in relation to the gage section was kept under 0.03 *mm* total runout.

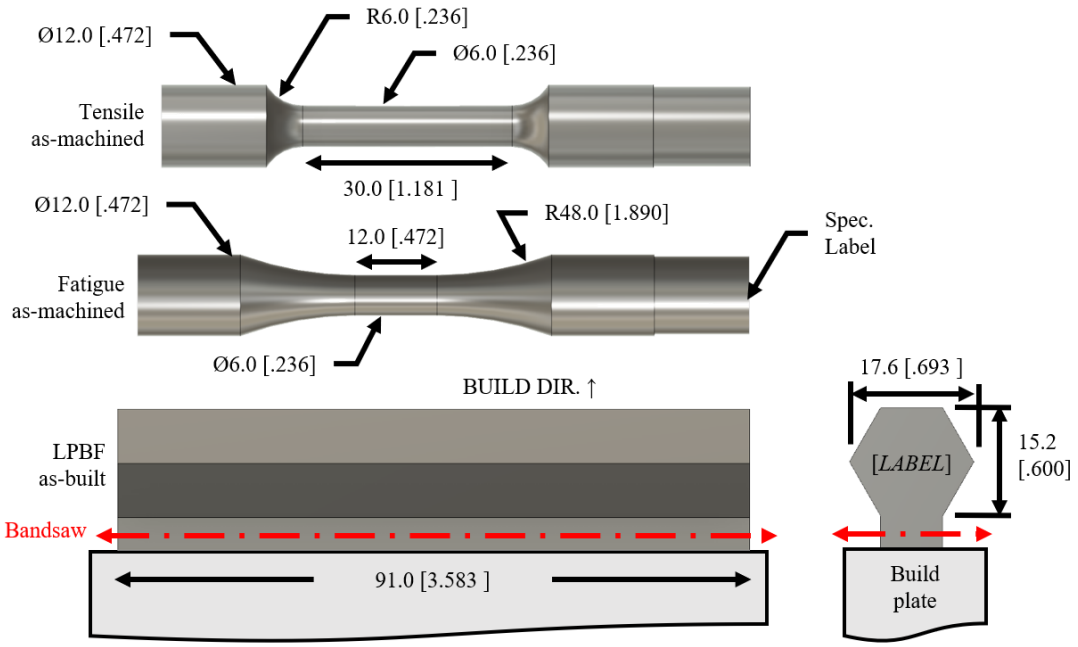

Figure 4. Top) As-machined tensile specimen geometry. Middle) As-machined fatigue specimen geometry. Bottom) As-built universal specimen design, in relation to the build plate. All unbracketed dimensions are in [mm], and bracketed dimensions are in [in].

The design of the LPBF-manufactured specimens, shown in Figure 4, is a simple hexagonal prism of 15.2 *mm* across flats and 91.0 *mm* in length. All specimens were built horizontally, or with their longitudinal axis normal to the build direction. Specimens were built horizontally since such a strategy yields the longer fatigue life and additionally keeps overall powder usage to a reasonable amount. These specimens are each raised off the build plate by the support geometry of a short, fully fused, rectangular prism that provides ample allowance for separation of the specimen from the build plate by band sawing. This large, solid support provides even heat syncing across the length of the specimen in addition to mechanical anchoring to the build plate that resists thermally induced stresses.

3.1.4 LPBF build strategy

An EOS M290 commercial LPBF system (commercially known as direct metal laser sintering (DMLS) system) was used to manufacture the specimens analyzed in this thesis. All four builds were manufactured on the same machine using the same processing parameters and build strategy. The layout of a single 250 x 250 *mm* build plate is provided in Figure 5. A single build layout contains 24 specimens for use in mechanical testing and 3 'witness' specimens for microstructural evaluation. The layout may be considered to have 5 distinct rows of mechanical test specimens, where rows are specimens located at the same Y location in the build plate. Specimen names identify row number as the first digit, beginning at "1" and proceeding consecutively to "5" in the +Y direction. The second digit refers to a specimen's location within a row, beginning at "1" and proceeding consecutively to either "2" or "9" in the +X direction. The first, third, and fifth rows have two specimens each oriented with their longitudinal axis in the X direction. The second and fourth rows have nine specimens each, oriented with their longitudinal axis in the Y direction. It should

be noted that specimens 3-1, 4-1, 4-2, and 5-1 from build A4 did not build properly due to a short-coating issue and were therefore not processed nor analyzed and tested.

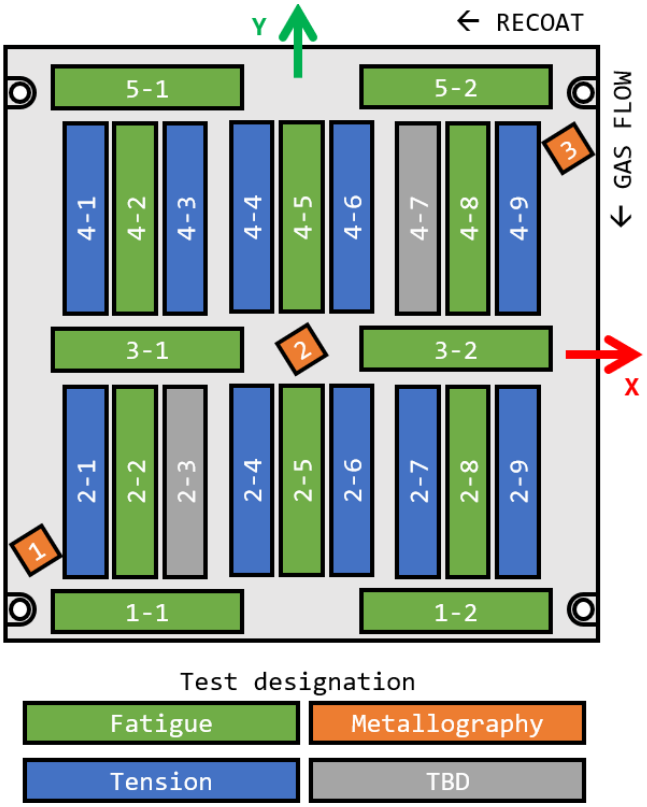

Figure 5. Build layout for all builds. Build direction is +Z, or out of the page. Note that specimens 3-1, 4-1, 4-2, and 5-1 from build A4 did not build properly and were not subsequenbtly processed nor analyzed or tested.

Fusing/exposure order was designed to adhere to known best practices for LPBF systems which minimize contamination via by-products of the laser-welding process. These by-products are mostly known to be preferentially transported in the direction of gas flow and recoat. As such, components furthest in the direction of gas flow are fused first, starting from the component furthest in the direction of recoat and proceeding against the recoat direction. Once a group of components approximately in the same Y region are fused, the next group of components that are now furthest in the direction of gas flow are

fused and so-on for each layer. The order of component fusion in addition to the a list of which tests were conducted on which specimens is provided in Table 4.

Table 4. Scan order

Specimen	Use	Build seq. No.	***Specimen***	Use	Build seq. No.
1-1	-	1	***4-1***	T**	15
1-2	F	3	***4-2***	F**	17
2-1	T	2	***4-3***	T	18
2-2	F	4	***4-4***	T	19
2-3	-	5	***4-5***	F	20
2-4	T	7	***4-6***	T	21
2-5	F	8	***4-7***	-	22
2-6	T	9	***4-8***	F	23
2-7	T	10	***4-9***	T	24
2-8	F	11	***5-1***	-	25
2-9	T	12	***5-2***	-	27
3-1	-	13	***B1***	M	6
3-2	-	16	***B2***	M	14
			B3	M	26

"F" indicates fatigue specimen. "T" indicates tensile specimen. "M" indicates 'witness' specimen for microstructural evaluation.
**A4-4-7 underwent tensile testing.*
***A4-3-1, 4-1, 4-2, and 5-1 were not tested due to improper manufacture.*

All specimens were built using the 'stripes' scan strategy and the 'time homogenization' methodology. The stripes scan strategy, in addition to the homogenizing heat treat applied to the specimens post-build, makes specimen orientation within the X-Y plane non-influential on mechanical properties. The stripes scan strategy, shown in Figure 6, refers to a single n^{th} layer of a component, i.e. a cross-sectional slice, being scanned in parallel stripe regions. Once the entire interior of a slice of a component is fused in this manner the contours of the slice are scanned. All components present in the current n^{th} powder layer are fused in this fashion in the specified scan order. The process repeats in all subsequent layers. Stripe orientation is incremented by 67° between layers resulting in the orientation of the stripe in the n^{th} layer only repeating in the $(n + k \cdot 361)^{th}$ layers. The

time homogenization methodology uses the infill longest scan vector within a layer to define the time between the start and end of all other scan vectors within a layer. This strategy avoids areas of a build which only require short scan vectors from building up heat.

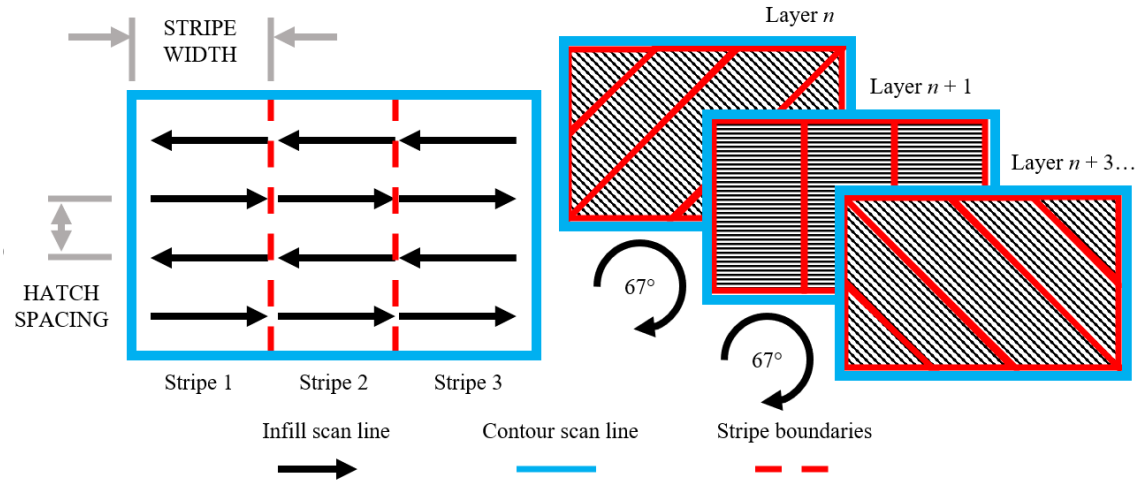

Figure 6. Description of the 'stripes' scan strategy. Infill scan vectors are in black, contour scan patterns in blue, and stripe boundaries in red.

Relevant LPBF build process parameters are provided in Table 5. These parameters adhere to standard build parameters provided by EOS for 40 μm-layer 17-4 PH powder. Only parameters for the scan paths that form the interior of the analyzed specimens are provided, as alternate parameters for specialized scan paths such as those used for a contour scan path, 'upskin', or 'downskin' will not make up the final as-machined specimens which are analyzed and tested.

Table 5. LPBF build parameters

Parameter	Value
Layer height	40 μm
Laser power	220 W
Scan speed	755 mm/s
Hatch spacing	0.11 μm
Beam diameter	80 μm
Built plate temperature	80 ℃
Scan strategy	'Stripes'
Stripe orientation alternation	67°
Build time (approximate)	85 hr

3.1.5 Post-LPBF specimen processing

The post-LPBF thermal processing and surface preparation of the mechanical test specimens examined in this study should were chosen according to two major motivations. First, the independent variable to be primarily investigated is powder-use state, the effects of which are suspected to be subtle. Factors in specimen preparation and post-processing known to produce confounding effects in fatigue should are thus either eliminated or made equal between all tested specimens. Second, specimen thermal processing and surface preparation conditions of interest and relevance to the considered field of applications should be investigated. The overall processing flow for both tensile and fatigue specimens is described in Figure 7. All specimens are solutionized and aged on the build plate, then separated by band sawing. Both specimen types are rough and finish machined via a similar procedure. Specimens intended for fatigue testing are polished to eliminate effects of the machining process that can influence fatigue performance. A small amount of 0.625 *in* diameter wrought bar (UNS S17400 AISI type 630 specification) was heat treated in the same lot and used in following experiments to provide a baseline of performance. This material is referred to as "W1" in subsequent writing and figures.

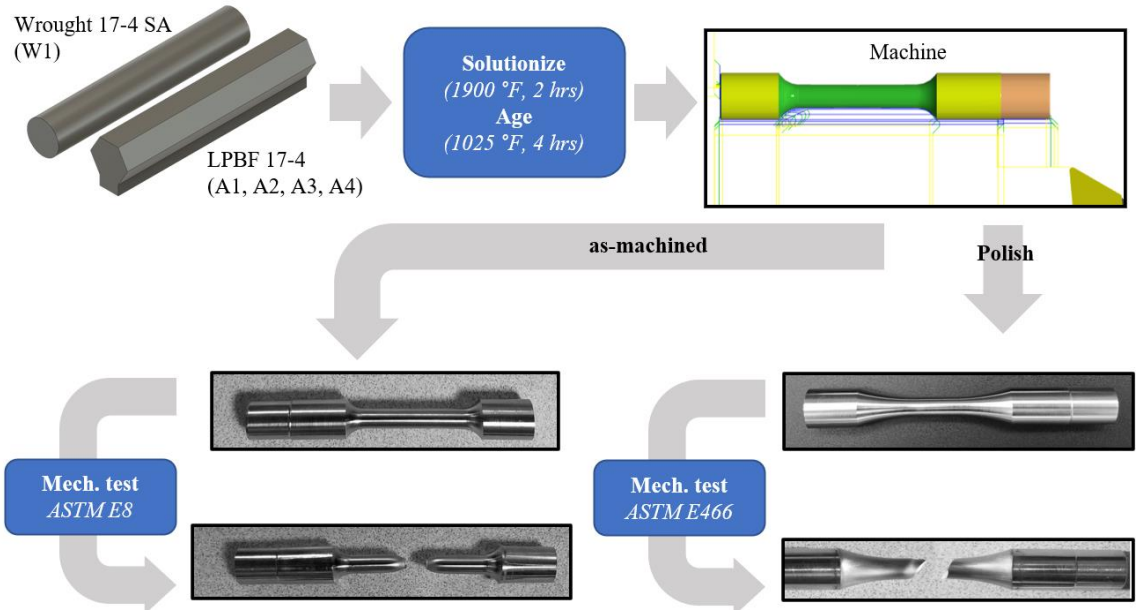

Figure 7. Manufacturing process workflow for tensile and fatigue type mechanical test specimens.

As discussed earlier, the best fatigue properties are seen in the H1025 condition, which is therefore used here. Per the AMS specification heat treatment was accomplished by solutionizing at 1900 °F [1038 °C], air quenching at a sufficient rate to below 90 °F [32 °C], and finally aging at 1025 °F [552 °C] for 4 hours [83]. All specimens were heat treated in a single lot, in their as-built condition on the build plate, in a temperature monitored vacuum furnace with quenching performed by back-filling with argon. Prior to this heat treatment all specimens were solutionized and aged in one prior cycle as a single lot. This cycle utilized the incorrect time period for aging and as such a second correct cycle was performed, as described. This additional prior treatment is not expected to produce significant differences as opposed to a single, correctly executed cycle nor produce any differences between individual specimens.

All specimens intended for mechanical testing were machined to 1) produce a low roughness free surface and 2) remove all sub-as-built-surface defects typical of the LPBF

process. Machining was performed by the author on an NC Okuma Genos L250 turning center. All specimens were turned with identical tooling, tool paths, cutting feeds and speeds, and flood coolant conditions. The only differences in machining strategy between tensile and fatigue type specimens is tool path shape. Cutting conditions echo example practices described in ASTM E466, Appendix section X1. After facing, drilling, and boring of a center in one specimen end, all functional features of a specimen are turned in a single set-up on a live-center, ensuring low-runout between specimen grip surfaces and the gage portion and thus low bending stresses experienced during testing. The finish tool path removed 0.012 *in* (dia.) of material with carbide insert tooling. Inserts were carefully monitored for wear and frequently replaced. Inspection of the machined specimens showed no evidence of undercutting of the fillet radii nor significant barrelling of the gage section due to deflection. Tensile specimens were machined with a 0.001 *in* taper towards the middle of the gage section, as allowable per ASTM E8. All specimens of both types were visually inspected for scratches, chatter, nicks, and other deviations from expected surface finish. As-machined specimens were inspected with a *Mitutoyo Surftest SJ*-410 and displayed a surface roughness of roughly R_a = 9.0 μm. Fatigue specimens were polished after machining using the below procedure to impart a final surface with low roughness and a lay parallel to the specimen axis.

1. Hand-polish using #1000 grit SiC sandpaper and a light cutting fluid (WD-40) the gage portion and fillets of a specimen rotating at 500 *rpm* for approximately 10 seconds, imparting a circumferential lay. This is to remove machining marks and the surface layer affected by the machining process.

2. Hand-polish longitudinally using a light cutting fluid and increasing grits of SiC sandpaper (#800, #1000, and #2000 consecutively) imparting a lay along the axis of the specimen parallel to the direction of stress.

A large sample of fatigue specimens (19) were inspected via the non-contact method of scanning coherence interferometry using a *Zygo zegage* interferrometer. A region of 834 x 834 μm was scanned. While ASTM E466 only specifies R_a = 0.2 μm [8 μin] as a requirement, multiple other parameters were measured, as displayed in Table 6. Form was subtracted from the measured surface profile by removing a cylinder of best fit, as is standard procedure per ASME B46. The software tools accompanying the interferometer were used for calculation of all presented surface roughness parameters, adhering to standard methods. While the region inspected does not encompass the entire gage section surface it provides a measurement typical of any one specimen surface finish, barring the presence of significant defects in the unscanned region. Since all sampled specimens displayed acceptable surface finishes the remaining specimens were not individually inspected via interferometry, and merely visually screened for surface defects. A typical scan is provided in Figure 8.

Table 6. Typical fatigue specimen gage section surface roughness

Parameter	*Mean [µm]*	*Standard deviation [µm]*
S_a	0.121	0.018
S_q	0.162	0.018
S_v	-1.300	0.304
R_a	0.080	0.023

19 polished fatigue specimens were sampled. Measurements were taken from an 834 x 834 µm sample area, with a best-fit cylinder subtracted from the as-measured profile to remove form.

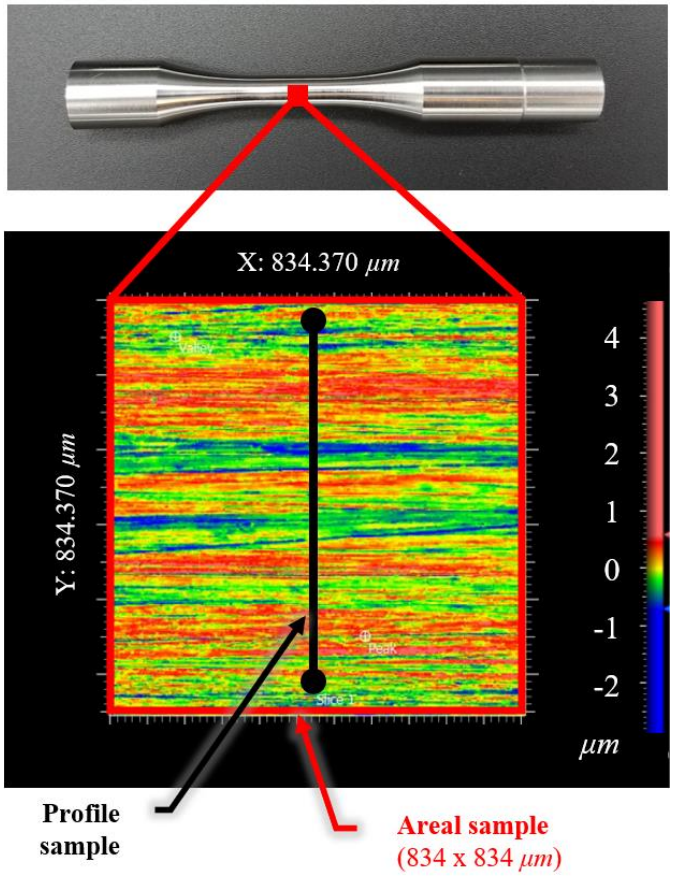

Figure 8. Typical interferometric scan of a polished fatigue specimen. The depicted scale in microns. The portion of the scan that forms the areal and profile samples are depicted in red and black, respectively. The profile sample is taken perpendicular to the direction of lay.

3.2 Powder characterization

Powder samples were taken from the hopper area immediately prior to each build in accordance with ASTM B215, via practice 1B, using a single-level tube sampler. Samples

were immediately stored in sealed containers and kept in an environmentally controlled location. In the case of all powder characterization efforts, powder sample containers were not opened except to extract them for measurement. For morphological evaluation powders were placed on carbon tape and imaged using a *Zeiss Ultra 60* SEM – all samples were immediately imaged in the same session.

In order to assess flowability of the sampled powder conditions Hall flow testing was conducted per ASTM B213. A Hall flowmeter funnel was used in combination with test method 2. A quantity of roughly 50 g (-0.09/+0.16 g) of powder from each powder condition was used for each test. Each ~50 g sample was tested three times, and each sample was weighted directly prior to each test. All flow times were taken by a single operator in a single session. A corrected flow time was calculated for each test, where the measured flow time ($t_{flow,meas.}$) was multiplied by a correction factor of 50 g divided by the measured mass of the sample (m) to form a corrected flow time (t_{flow}). All flow times reported from this point on refer to this corrected flow value.

$$t_{flow} = t_{flow,meas.} * \left(\frac{50}{m}\right) \quad (1)$$

A *Freeman FT4* powder shear cell was used for rheological evaluation of the sampled powders according to ASTM D7891. Specified masses of the powder samples were loaded into the testing apparatus shear cell vessel using the built-in mass scale. Powders were first conditioned (thoroughly mixed and homogenized) in the shear cell, then compacted, and finally leveled according to the standard. Powders were compacted under a consolidation stress of 6 *kPa*. The powder was then manually pre-sheared according to the standard, then the automatic test program proceeded to the shear the powder at several

distinct levels of applied normal stress while recording the powder's torsional resistance to shearing. Torsional force measurements were converted to shear stress according to the standard. Bulk rheometry measurements were extracted according to the standard.

3.3 Microstructural evaluation

Witness specimens B1, B2, and B3 were extracted from each build and subjected to the same heat treatment in the same heat lot as all specimens. Specimens were sectioned by band sawing in a plane parallel to the build section through their middle. Once sectioned, specimens were mounted in epoxy mixed with conductive nickel powder. Specimens were rough ground for approximately 30 *min* using a conventional automatic metallographic grinder/polisher with #240 SiC sand paper lubricated and cooled with water, removing any heat or deformation affected portions due to the sectioning process. Following this step, mounted specimens were polished with #500, #1000, #2000, and #4000 grit SiC sandpaper. Diamond abrasive suspensions of 9, 3, and 1 μm in abrasive particle size were then used. Modified Fry's reagent, consisting of 25 *mL* HCl, 25 *mL* HNO_3, 75 *mL* H_2O, and 1 *g* $CuCl_2$, was swabbed on for roughly 30 seconds to chemically etch and reveal microstructure. Specimens were inspected optically with a *Leica DVM6* digital microscope. Additionally, specimens were inspected with a *Zeiss Ultra 60* SEM.

3.4 Mechanical testing

3.4.1 Computed tomography inspection of fatigue test specimens

Computed tomography (CT) was used to gain insight as to the typical quality level of the produced components in addition to possible correlation of pre-existing defects with

fracture initiators. Inspections were conducted on three fatigue specimens. A *Zeiss Metrotom 800* industrial CT scanner with a maximum acceleration voltage of 130 *kV* was used for the inspection. Specimens were inspected in their fully heat treated and machined condition. The relevant CT analysis parameters are provided in Table 7. Two scans of differing parameters were conducted on a select specimen in an attempt to assess the effects of beam hardening on the identification of porosity subsurface regions. CT data was reconstructed using the commercially available software package *VGStudio MAX* from *Volume Graphics*. ISO-50 thresholding was used for initial surface determination, after which an advanced deformable volume technique was used for a refined surface determination. The integral porosity identification tool "EasyPore" was used to identify regions of porosity. Identified regions, if there were any, were manually screened for identify them as true pores or scan artifacts.

Table 7. CT analysis parameters

Parameter	Scan 1	Scan 2
CT system	Zeiss Metrotom 800	
Voxel side length	15 μm	
No. of projections	800	
Scan time	~1.0 *hrs*	
Accel. voltage	130 *kV*	
Current	45 μA	60 μA
Prefilter	0.75 *mm Cu*	1.5 *mm Cu*

3.4.2 Tensile, fatigue, and hardness testing

Tensile tests were conducted on H1025 condition fully machined LPBF manufactured specimens. In addition, a small number of reference tests were conducted on wrought 17-4 bar, heat treated and machined in the same manner. Tests were conducted according to ASTM E8 on an *MTS* servohydraulic 98 *kN* capacity load frame. An *Interface* 111 *kN* capacity load cell was used for data acquisition. Cylindrical collet grips with a 12

mm grip diameter were used. Extensometry data for both analysis and control purposes was attained with an *MTS* 1 *in* blade-type extensometer. Following recommended ASTM E8 procedures, specimens were pulled at a strain rate of 0.45 *mm/min* prior to yield, and 5 *mm/min* after yield and until failure. Force, extensometry (strain), crosshead displacement, and time data were captured at a rate of 102 *Hz*. Frame alignment was checked via the method described in Appendix X2 of ASTM E1012. Once force and strain data were acquired stress was calculated as the measured force over the cross-sectional area. Yield strength was calculated via the 0.2% offset method. Modulus was calculated via linear least-squares fitting to the linear portion of the stress-strain curve. Ultimate strength and elongation at failure were also extracted as the peak engineering stress observed and the maximum strain before failure observed. Ten specimens per build were tested, as noted in Table 4. Note that the same specimens in each build were used for testing, with the exception of specimen A4-4-1 not being tested, and specimen A4-4-7 being tested in its stead.

Fatigue tests were conducted on H1025 condition fully machined and polished specimens. Force controlled constant amplitude axial fatigue tests were conducted according ASTM E466 on the same *MTS* servohydraulic 98 *kN* capacity load frame. An 8 *Hz* sinusoidal forcing function with a stress ratio of $R = 0.1$ was utilized. Force error was captured at a rate of 512 *Hz* using a logarithmic sampling strategy and occasionally inspected for divergence from the commanded levels – none was shown. Six tests per build were conducted, and tests were on the same specimens of the same location from each build, spread across the build area. A1-4-2 and A2-2-8 data is not presented, due the lack

of a properly built specimen in the first case and an improperly interrupted fatigue test in the second.

Rockwell hardness was measured for a selection of specimens from each build. Hardness tests were conducted with a *Wilson Rockwell 574* automatic hardness tester. Tester repeatability and error was checked for compliance with ASTM E18 before and after any testing session. Hardness was measured on the HRC scale, using the appropriate indenter. Hardness was measured on the 12 *mm* diameter grip portion of fully machined H1025 condition specimens. Specimens were mounted to a V-block, anchored to the test platform to prevent movement between tests, to center them under the indenter and measured hardness was compensated for the known diameter of the tested specimen according to ASTM E18.

3.5 Fatigue life reliability analyses

This study uses a reliability modeling approach to compare the effects of powder condition on fatigue life. A small set of initial fatigue tests (four) were conducted at varying stress levels to produce a very rough S-N curve to aid in selection of loading conditions for in-depth investigation. Once initial tests were conducted, a simple linear fit was made to the S-log(N) data. A testing load that would produce a stress of S_{max} = 867 *MPa* was selected based on this fit to produce failure in the desired HCF regime. All following fatigue tests were conducted at this S_{max}, with a loading ratio of R = 0.1, at a frequency of 8 *Hz*, under a force-controlled sinusoidal forcing function.

Two analysis methods were used to compare the fatigue life data from each build, A1, A2, A3, and A4. The first utilized parametric methods to fit probability density

functions to the observed distribution of fatigue lives from each build and conclude if any were different. The second utilized the non-parametric empirical survival function to characterize each fatigue lives displayed in each build and conclude if any were different.

3.5.1 Parametric analysis

Parametric statistics are based in description of data using a deterministic model such as a probability density function (PDF). A wide range of PDFs exist to model many natural and man-made phenomena. Historically, fatigue life and reliability have been modelled by a select number of PDFs, notably the Weibull and lognormal distributions, or variations thereof. An extensive review of the history of applications of these distributions to fatigue life data is beyond the scope of this work, but other authors have extensively summarized their use and applicability, as noted in the background section. To summarize, both distributions have similar characteristics. Both can be right skewed which accurately describes the infrequent phenomena of structures exhibiting very long or possibly infinite fatigue lives far from the average fatigue life exhibited. The lognormal PDF is often favored for its simple form which is a log-transformation of the well-known normal distribution. As such the lognormal distribution is described by two parameters, the log-mean and log-standard deviation, μ and σ. Here, if x is the random variable, μ is the mean of $\ln(x)$ and σ is the standard deviation of $\ln(x)$. This form allows many well-known statistical techniques developed for comparing normal distributions by simply transforming the data mathematically. The Weibull distribution is well-used in the world of mechanics and reliability modelling and favored for its flexible shape which can model data as having a PDF that is exponentially shaped, bell-shaped, or some variation in between. The distribution is described by the shape and scale parameters, β and η. Both the

Weibull and lognormal distribution PDFs are presented in equations (2) and (3), respectively.

$$P(x) = \frac{\beta}{\eta}\left(\frac{x}{\eta}\right)^{\beta-1} exp\left[-\left(\frac{x}{\eta}\right)^{\beta}\right] \quad (2)$$

$$P(x) = \frac{1}{x\sigma\sqrt{2\pi}} exp\left[-\frac{ln(x-\mu)^2}{2\sigma^2}\right] \quad (3)$$

The workflow used for parametric analysis of fatigue life in this work began with an exploratory data analysis to evaluate how a range of PDFs fit the data. Both the Weibull and lognormal distributions are shown to be appropriate descriptors. Next, both distributions are fit to the data from each build forming a deterministic predictor of the probability of the fatigue life. Fitting is accomplished via the maximum likelihood estimation (MLE) method. This method is computationally intense but does not require the binning of data that other methods would. Likelihood refers to the probability of a hypothesis or model (given a set of parameters, θ) accurately describing data. Likelihood, L, is the optimized variable during the MLE process. Frequently, the natural log of a likelihood function, $\ln(L)$, is handled for mathematical convenience. Additionally, the log-likelihood is sometimes made negative before it is optimized since optimization techniques apply best to minimization. For a model with the parameter set, θ, the MLE process iteratively varies the parameters to maximize the likelihood (or minimize the negative log-likelihood). We are left with a scalar value of maximized likelihood given these parameter values, $L|\hat{\theta}$, or the negative log-likelihood $-\ln(L|\hat{\theta})$. Despite both these values corresponding to a specific value of likelihood, they are often simply referred to as just the likelihood of a model.

Once models, e.g. Weibull or lognormal PDFs, have been fitted via MLE statistical tests may be applied for comparing the models. The likelihood ratio test compares two models based on their maximized likelihood. The models must be nested, meaning that if one model relies on the parameter set θ, the other relies on the same parameter set in addition to additional parameters as well. An example would be $f(x) = a + bx + cx^2$ nests the both the models $g(x) = a + bx$ or $h(x) = a + bx + 2x^2$, where the parameter *c* has been either removed or fixed. The more complex model has all parameters unrestricted, and the less complex model restricts one or more parameters by either eliminating or fixing them. The likelihood ratio test assumes the null, that the restricted model accurately represents the data and tests for the alternative, that the unrestricted model more accurately represents the data. Letting L_0 and L_1 be likelihood of the restricted (null), and unrestricted (alternate) models the likelihood ratio is simply:

$$\lambda = \frac{L_0}{L_1} \tag{4}$$

As discussed, it is more convenient to use log-likelihoods. Additionally, by taking the log of the ratio and doubling it we can produce a relevant test statistic that follows the chi-squared distribution when the null model applies.

$$X^2 = -2\ln(\lambda) = -2\ln\frac{L_0}{L_1} = -2(\ln L_0 - \ln L_1) \tag{5}$$

If the negative log-likelihoods are considered, a simple substitution of each ln(*L*) term is performed, and the negative sign factors out. The test statistic can be compared to a chi-squared distribution at the desired significance level α, with *k* degrees of freedom, referring

to the difference between the number of free parameters considered in the unrestricted and restricted models.

$$null\ is\ true: X^2 < X^2_{k,\alpha}$$
$$alternative\ is\ ture: X^2 > X^2_{k,\alpha}$$

To utilize the test to determine if two distributions which described the data from two groups differ, the problem is phrased as such and the following steps are executed.

Null: Both groups come from a single population, described by *n* parameters

Alternative: Each group comes from a distinct population described by *n* parameters, making for $m = n + n$ parameters total.

1. Fit a distribution using MLE to a single set of data made up of both groups. Calculate the log-likelihood of this null model.
2. Fit a distribution using MLE to each group individually and calculate each log-likelihood. Sum them to produce the log-likelihood of the alternative.
3. Compare null and alternate log-likelihoods with the likelihood ratio test, with $k = m - n$ degrees of freedom, at a desired significance level.

3.5.2 Non-parametric analysis

Non-parametric analysis does not rely on fitting of deterministic models to data. Non-parametric methods are extremely valuable in cases where data cannot be confidently said to adhere to a known distribution or if a data set is small enough that it is difficult to prove as much. A non-parametric method of describing reliability data of great use is the empirical survival function, also known as the Kaplan-Mier estimator. This function describes the probability for survival, or in this case the probability for any one specimen

to not have failed by *N* cycles. This concept results in a metric that is directly analogous to the complement of the cumulative density function (CDF). Utilizing a set of fatigue life data for tests conducted at a single loading criterion the survival function is expressed as function of the number of failures thus far O_N and the number of test specimens still 'at risk' R_N at any cycle count *N*.

$$S(N) = \prod_{i:N_i \leq N} \left(1 - \frac{R_N}{O_N}\right) \tag{6}$$

An estimator of variance, Greenwood's formula for variance, can be calculated for the survival function, and confidence bounds can be calculated via the *z*-distribution.

$$Var\big(S(N)\big) = S(N)^2 \sum_{i:\, t_i \leq t} \frac{O_N}{R_N(R_N - O_N)} \tag{7}$$

$$Bounds = z_{\alpha/2}\sqrt{Var\big(S(N)\big)} \tag{8}$$

The log-rank test, also known as the Mantel-Cox test, distinguishes the empirical survival curve between groups, $S(t)_j$. While survival curves can be compared graphically, the log-rank test takes into account how sampling error effects how well a curve models the survival probability of the underlying population. The strengths of the test include not assuming any underlying population distribution, the ability to account for right-censored observations, and good handling of right-skewed distributions. The test relies on the same assumptions that the Kaplan-Mier estimator does, namely that censoring is not related to prognosis and that recorded event times are accurate. While the test is most often used to conduct pairwise comparisons it can also be aimed at more than two groups and conclude

whether any display detectable differences. When doing so, the power of the test increases, analogously to how the power of ANOVA is superior to multiple pairwise t-tests.

The structure of the test is simple: the null hypothesis assumes that there is no difference in underlying population survival probabilities, with the alternative being that there is a detectable difference. In the context of fatigue lives, we define that for each group g an event constitutes a failure at N cycles, and a censored observation is a test which was halted without failure at N cycles. Computation of the test statistic requires first assuming the null and treating all groups as a single set of observations to construct a single empirical survival function. This survival function predicts survival probability at any cycle count N as a proportion of observed failures thus far O_N divided by the number of specimens that are still 'at-risk' of failure R_N.

$$S_0(N) = \frac{O_{0,N}}{R_{0,N}} \in [0,1] \tag{9}$$

By referencing this null survival function, the expected number of failures in each group, should its independent survival function be identical to S_0, can be calculated. The number of specimens at risk in group g at time N multiplied by the null survival function defines the expected number of failures that have occurred in group g at time N.

$$E_{g,N} = R_{g,N} \frac{O_{0,N}}{R_{0,N}} \tag{10}$$

Once the expected and actual number of failures in for each group is known they can be compared in each group and combined across groups to produce a relevant test statistic.

There are multiple methods for calculation of a test statistic for the log-rank test, but here a statistic that can be related to the chi-squared distribution is chosen.

$$X^2 = \sum_g \frac{\left(\sum O_{g,N} - \sum E_{g,N}\right)^2}{\sum E_{g,N}} \tag{11}$$

For m groups being compared, this statistic is then compared to the value of chi-squared distribution with $k = m - 1$ degrees of freedom evaluated at the desired probability of type I error, α.

RESULTS AND DISCUSSION

4.1 Powder measurements

Powder morphology can be qualitatively assessed by the SEM micrographs attained of the various powder samples. Powder samples A2, A3, and A4 all displayed fairly similar morphological characteristics, and as such Figure 9 displays a sample from the powder used to manufacture build A1 compared to the powder used to manufacture build A3. The A1 powder sample was sampled from the hopper directly prior to the execution of the A1 build process and thus represents directly used virgin powder, solely exposed to the conditions require to load it into the LPBF machine and prepare the first build.

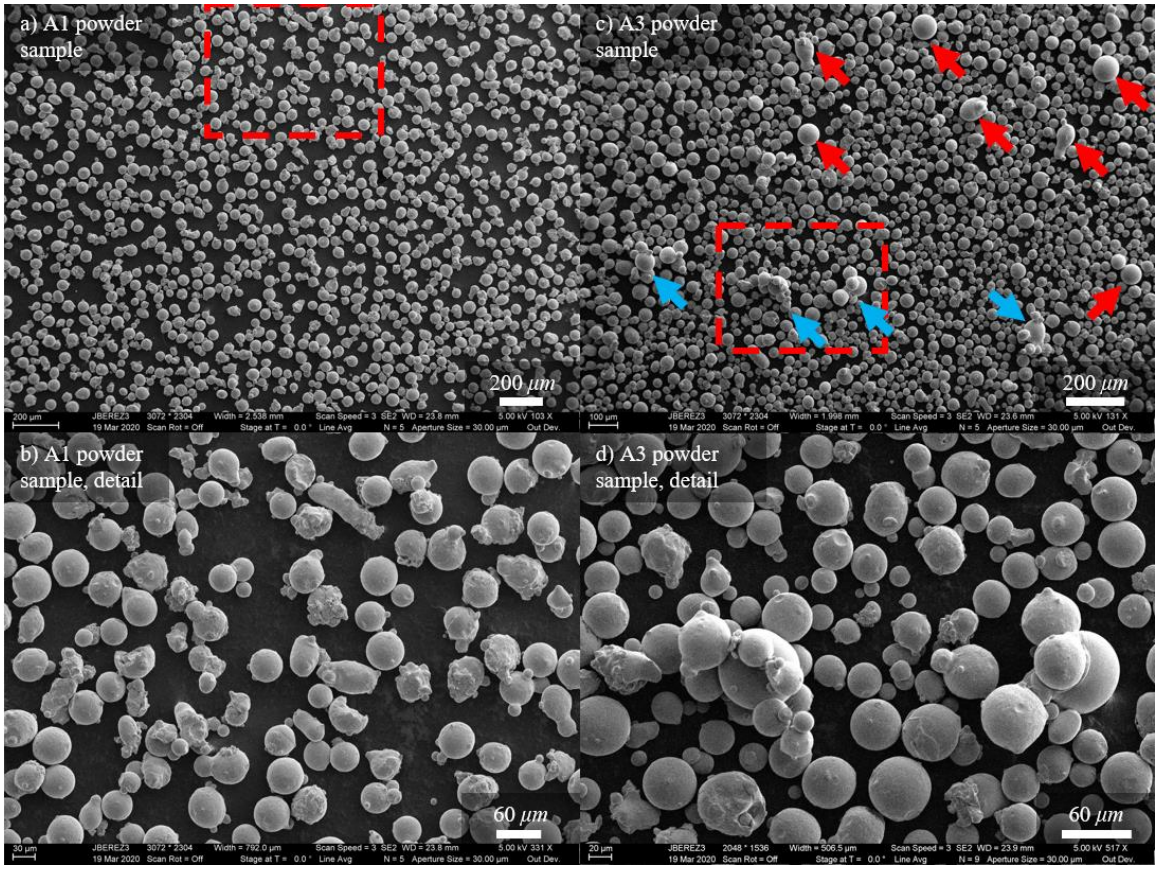

Figure 9. SEM images of powder samples taken from the hopper powder supply corresponding to powder used for the first (A1) and third (A3) builds. Suspected meltpool ejecta are identified by red arrows. Particles that display satellites or fusion to other particles suspected as a result of the fusion or spatter process are identified by blue arrows.

The A1 powder sample exhibits particles of a fairly tight size distribution, particularly with a lack of many particles far above 40-50 μm in diameter – for reference, the d_{90} measurement provided by the powder manufacturer is 55 μm. There does not appear to be an excess of fine particles either. Particles display a morphology typical of the gas atomization process which was used to manufacture the powder [3]–[5]. Particles are generally fairly spherical, with a significant proportion accompanied by small satellites, normally several factors smaller in diameter than the parent particle. Very few highly elongated particles are present. The A3 powder sample notably differs in its make-up due to the presence of several very large single particles or multi-particle agglomerates. These

particles appear to be byproducts of the LPBF process that is undertaken in the build area of the process chamber. The large particles or size with few satellites (notated with red arrows) are likely meltpool ejecta due to violent meltpool conditions [95]. The large agglomerates appear to show very smooth surface texture of at least one large particle, indicating that meltpool ejecta managed to fuse with other virgin particles. The particles have been evidently transported to the hopper area via one of several possible mechanisms. High velocity spatter, large enough in size, may have traveled against the dominant shielding gas flow direction [96]. Turbulent gas flow in regions of the build may also be responsible [97]. The recoater blade may have also transported them back into the hopper. Particles much larger than the layer height (40 μm) have difficulty settling in the power bed and may be captured by the recoater blade and shed in the hopper during a subsequent recoat when a high wall of powder can rip the large particles from the recoater.

Measurements of powder flowability, quantified as Hall flowability, are presented in Figure 10. The results show an increasing trend in flow time (i.e. a decrease in flowability) accompanying the degree of powder repeated process exposure, which matches basic flowability energy (BFE) measurements from a study looking at un-sieved re-used powders, which are a similar condition to the repeated process exposed powders [43]. A one-way ANOVA was performed on the data, shown in Table 8, resulting in a conclusion that at least one group significantly differs from the rest with a *p*-value of <0.001. A Tukey-Kramer analysis was performed to further investigate the differences between the powder flowabilities, as shown in Table 9. Data appears to be distributed normally and the respective sample variances are sufficiently homogenous, taking into consideration small number of observations. Levene's test on the data produces a *p*-value of 0.206, supporting

this claim. The virgin powder and powder used to manufacture build A1 displays a significant difference when compared to all other builds. Finally, the powder that is used to manufacture builds A3 and A4 display a difference at the limits of significance with a *p*-value of 0.05. The minor differences between the powder samples A2, A3, and A4 imply that the effects of repeated process exposure conditions on Hall flowability saturates after the powder has been exposed to just two prior builds, in this case. A reduction in flowability may be attributed to the large aspherical particles that have been added to the powder supplies by the LPBF process exposure. The difference in the virgin and A1 powder is interesting, as the powder should have experience very little exposure to influencing conditions. It is possible that the compaction of powder in the hopper by the operator prior to build A1, a standard procedure, better mixed the powder or broke up agglomerate particles present in the virgin powder container.

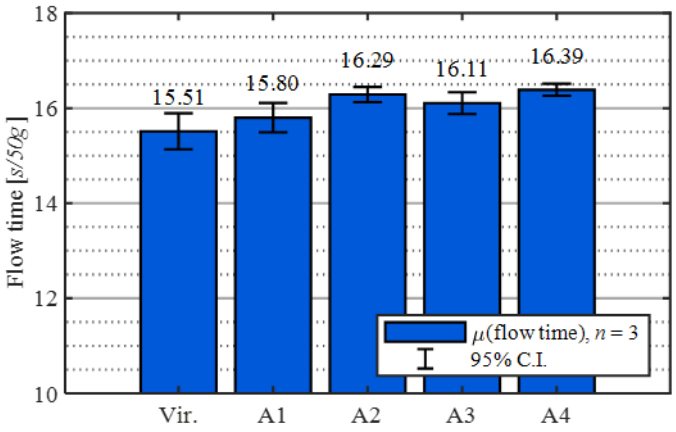

Figure 10. Hall flowability, measured in seconds of flow per 50g sample. The average of three tests with an identical powder sample is presented.

Table 8. One-way ANOVA on Hall flowability

Source	DoF	SS	MS	*F*	*p*
Factor	4	1.555	0.389	35.7	<0.000
Error	10	0.109	0.011		
Total	14	1.663			

Sum of squares (SS) and mean square (MS) are presented in [sec^2].

Table 9. Tukey-Kramer comparison of Hall flowability

	Lower C.B.	Mean diff.	Upper C.B.	
Comparison		[*sec*]		*p*
Vir.-A1	-0.57	-0.29	-0.01	0.04
Vir.-A2	-1.05	-0.77	-0.49	<0.001
Vir.-A3	-0.87	-0.59	-0.31	<0.001
Vir.-A4	-1.15	-0.87	-0.59	<0.001
A1-A2	-0.77	-0.49	-0.21	<0.001
A1-A3	-0.59	-0.31	-0.03	0.03
A1-A4	-0.87	-0.59	-0.31	<0.001
A2-A3	-0.10	0.18	0.46	0.29
A2-A4	-0.38	-0.10	0.18	0.77
A3-A4	-0.56	-0.28	0.00	0.05

Powder rheometry was investigated via the FT4 powder rheometry testing method. The results of testing on virgin powder as well as powders sampled from the hopper supply that was used to manufacture builds A1, A2, A3, and A4 are presented in Figure 11. In order to allow for a closer inspection of the produced shear stress values the pre-shear data points are not depicted, as they are at significantly higher normal stress values of 6 *kPa*. The shear stress curves do not imply any differences between the rheological properties of any powder sample, with minimal differences between individual gathered data points and overlapping of the interpolated curves in multiple places.

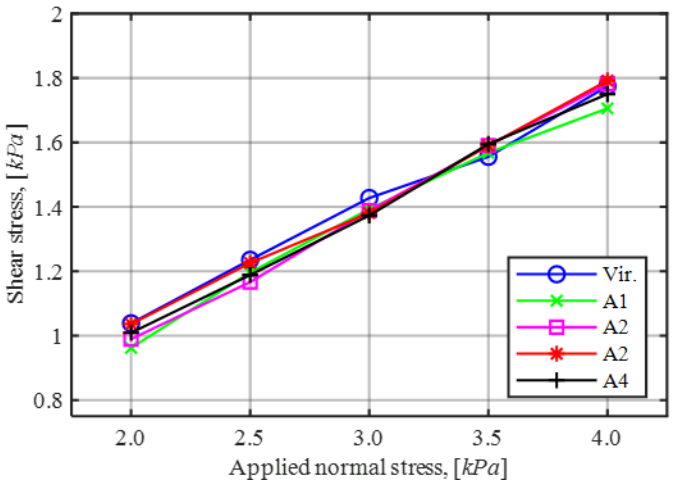

Figure 11. FT4 rheomtery test data. Data presented are taken during steady-state shear, pre-shear data is not pictured.

Several rheological properties of the powder can be extracted from these data using methods described in the relevant standard. A depiction of these methods applied to the virgin powder sample is provided in Figure 12. Shear data is used to calculate the yield locus as a line of best fit. The yield locus' y-intercept determines cohesion, and its angle to the horizontal is the angle of internal friction. Two Mohr's circles are drawn to determine the unconfined yield strength and the major principle stress. The first circle is tangent to the yield locus and the y-axis, with its center on the x-axis. The second is tangent to the yield locus, intercepts the pre-shear point, and has its center on the x-axis. The effective yield locus connects the origin to a tangent point on this circle and its angle to the horizontal is the angle of effective friction. A summary of these values for all analyzed powder samples is presented in Table 10. Interestingly, the virgin powder sample displays the greatest resistance to shearing, with the lowest angle of internal friction, highest cohesion, unconfined yield strength, and major principle stress. The flow function of the virgin powder is also the lowest, indicating a high cohesivity and resistance to free flow. No trends that accompany the degree of powder repeated process exposure are observed in any

extracted values. Interestingly the results run in contrast to what the flowability test might suggest; the virgin powder displays the most viscous properties in the FT4 test, but the greatest flowability in the Hall test. As earlier discussed, powder bulk fluid properties appear to be complex in their relation. There seems to be two possible conclusions – other studies [57], [58] that have concluded flowability trends with cohesivity/BFE incorrectly used permeability to approximate flowability; or the powder condition measured here is unique in that it results in good flowability coming with high cohesivity. It should also be noted that the inability to statistically test the reported rheology results, especially when the data is closely gathered as mentioned, may mean the cohesivity conclusions made here are confounded by measurement error.

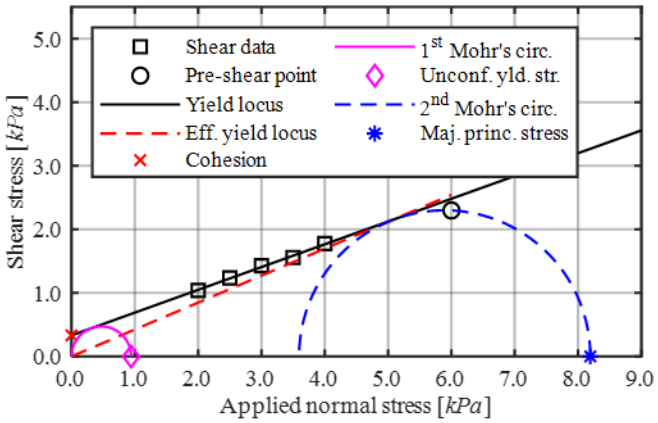

Figure 12. A depiction of the values extracted from a FT4 rheometry test. Data corresponding to the virgin powder sample is presented.

Table 10. FT4 rheometry test extracted values

	Ang. internal friction, φ [*deg.*]	Cohesion, C [Pa]	Unconfined yld. strength, f_c [Pa]	Maj. principle stress, σ_1 [Pa]	Effective ang. of friction, δ [deg]	Flow function, FF [σ_1/f_c]
Vir.	19.7	331	941	8199	23.0	8.7
A1	20.4	250	720	7960	22.9	11.1
A2	21.9	178	527	7966	23.7	15.1
A3	20.6	280	807	7940	23.4	9.8
A4	20.7	251	725	7772	23.3	10.7

Values were extracted from data in accordance with ASTM D7891.

4.2 Microstructural description of produced components

After mounting, polishing, and etching, specimens B1, B2, and B3 from all four builds were inspected via optical microscopy and SEM. Micrographs are presented in Figure 13. Microstructural differences detectable via these methods as a function of powder condition were not hypothesized and a cursory inspection of the revealed microstructures did not reveal any clearly defined distinctions. For contrast, micrographs from the equivalently heat treated wrought material (W1) are provided in Figure 13a. While both alloys appear to be of a largely martensitic content, the wrought material presents a microstructure with more lath-like packets of martensite, grouped in distinct directions that subdivide prior austenite grains. The AM material presents martensite that appears to be more blunted in its shape. This is likely due to the increased carbon content of the virgin powder (0.06%) compared to the wrought material (0.023%), which favors different martensite morphology as is well established for steels. The optical micrographs show that the solutionizing step of the heat treatment effectively homogenized the microstructure, removing most directionality and gradient due to repeated meltpool solidification, similar to results reported in other studies of LPBF manufactured 17-4 [61], [86]. This is especially evident when comparing to Figure 13c and d, which show a 17-4 as-built specimen,

sampled from a distinct build manufactured from a different powder lot but produced with the same process parameters.

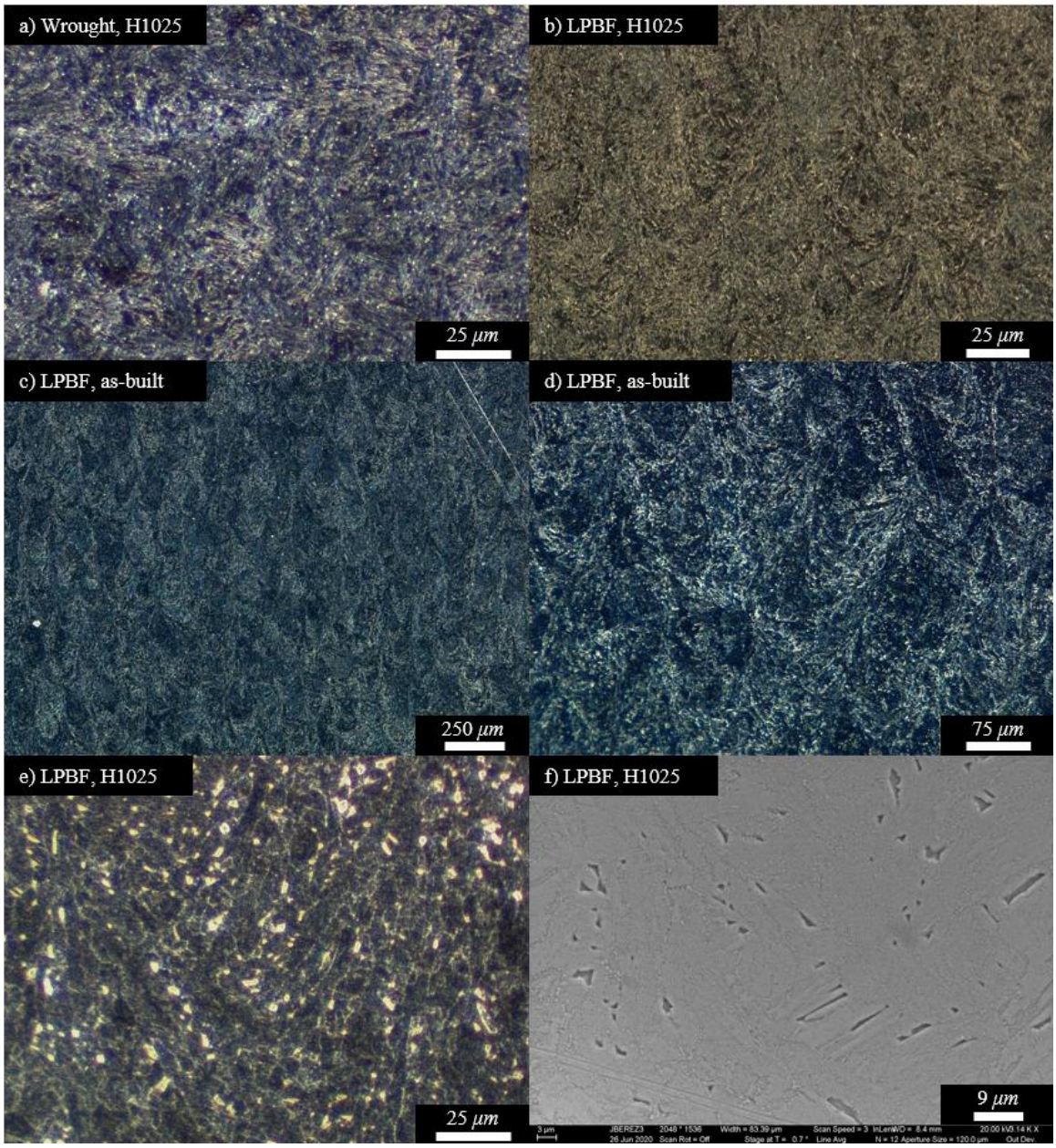

Figure 13. Micrographs of polished an etched a) Wrought H1025 17-4 b) LPBF H1025 17-4 c-d) As-built LPBF 17-4, different powder lot e) LPBF H1025 17-4, specimen A1-B3 f) LPBF H1025 17-4, specimen A4-B2.

Other expected features of the microstructure include retained or reverted austenite as well as precipitate particles. Retained austenite is not expected in the heat treated

specimens due to the argon processing atmosphere and the properly applied solutionizing cycle, and large retained austenite grains do not appear to be present [61], [63]. The optical micrographs do not provide sufficient magnification to examine for less obvious features, but the SEM micrograph in Figure 13f yields some insights. The martensite structure is more apparent, and it appears in groupings of elongated, but not strictly lath-like subgrains. Notably, a homogenous distribution of dark and irregularly shaped second phases are present – they correspond to the bright irregularly shaped areas in the optical micrograph of Figure 13e. They appear to have some depth, but they are not voids or porosity, as confirmed by an inspection of the unetched portions of the specimens (masked during etching) which did not show these features. The second phase regions range from 1-5 μm in size, effectively ruling them out as copper precipitates which have been widely reported to be very fine, on the order of 1-30 *nm*, depending on the degree of ageing. More likely, this second phase is reverted austenite. Bhambroo et. al. identified via EBSD reverted austenite with very similar density, size, and morphology in wrought 17-4 solutionized and aged at 1075 °F [580 °C] for 4 *hrs*. Several authors have reported findings of reverted austenite in aged 17-4 despite the fact that the known austenite formation start temperature of the bulk alloy is higher than the aging temperature used here (1025 °F [552 °C]) as well as in the noted study [98]–[100]. It is theorized that the matrix rejection of austenite stabilizing elements such as Ni, Cu, and C towards martensite boundaries during aging provide strong local nucleation sites for austenite to form at aging temperatures. The bright martensite boundaries seen in the optical micrographs and displayed as strings of particles in the SEM images are difficult to positively identify without applying further experimental techniques. They may be more reverted austenite, as observed by Viswanathan et. al. in

17-4 solutionized and aged at 1075 °F [580 °C] for 4 *hrs* [98]. They could also be M_6C_{27} or M_7C_3 type carbides decorating the boundaries, which would also be the result of Ni, Cu, and C rejected by the supersaturated martensite during the aging process which is also supported by prior literature [98], [100]. The difference in how they etched compared to the larger reverted austenite colonies would suggest they are carbides. The presence of these carbides, possibly greater in quantity than the wrought material due to the high AM carbon content, may impact ductility as observed in the conducted tensile testing.

4.3 Computed tomography inspection

CT scans of three specimens e.g., A1-F03, A4-F02, & A4-F07, were reconstructed and analyzed for porosity. Reconstructions of two scans of A4-F07 using two distinct CT analysis parameters are shown in Figure 14. It can be seen that the parameters of Scan 2 were successful at reducing beam hardening effects although their effect on the porosity analysis still cannot be entirely ruled out, even though a relatively low degree of beam hardening is observed. While some pores were identified by the software tools used, all automatically identified pores were disregarded as either scan artifacts or lacking in certainty of identification due to a their extremely small volume of only several voxels. None of these small pores displayed a change in gray values in the supposed pore region upon a manual inspection of individual scan slices. Overall, no pores were identified with any confidence in any of the analyzed CT scans. Fractography work, presented later in this study, supports this finding with fracture initiating defects being of a size and shape that would be extremely difficult to positively identify via the CT scanning methods used.

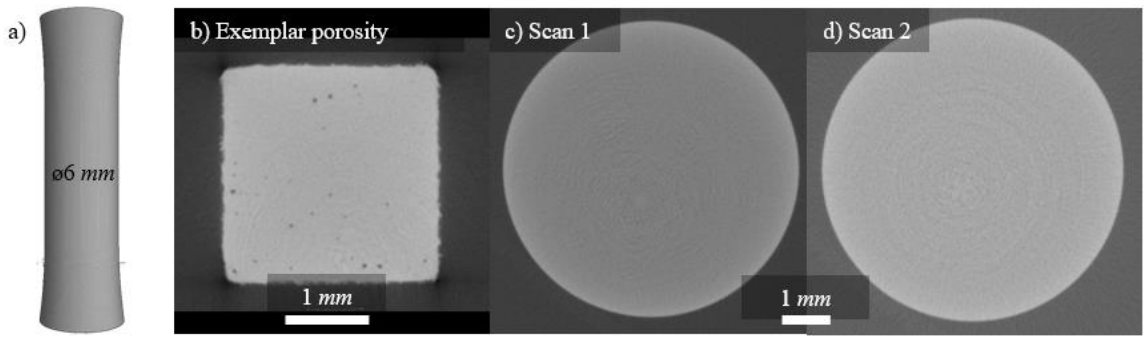

Figure 14. Images of from reconstructed CT scans showing a) The entire scan region of fatigue specimen A4-3-5. b) A 316L stainless steel specimen scanned using the same CT system displaying exemplar porosity [101]. c&d) A typical slice of a reconstruction corresponding to a scans of A4-3-5 using the scan 1 and scan 2 parameters – no porosity is detected.

4.4 Hardness by build and spatial origin

Rockwell hardness measurement were extracted from the grip regions of machined mechanical test specimens from each of the four builds, specifically specimens 1-1, 1-2, 3-1, 3-2, and 5-2. Note that specimen A4-3-1 could not be measured due to previously described short-coating issues. To test for a difference in the hardness between the tested specimens from the four builds a one-way ANOVA is conducted. Measurements from all 3-1 specimens are excluded in order to compare the identical sets of specimens between the builds. Results are presented in Table 11. There does appear to be at least one group that may significantly differ from the others. A Tukey-Kramer analysis is presented in Table 12 to provide further insight. The data was found to be approximately normal and the variances homogenous, with Levene's test on the data producing a *p*-value of 0.136. A2 appears to present the highest overall hardness, with the Tukey-Kramer method providing pairwise comparisons with A1, A3, and A4 with respective *p*-values of 0.099, 0.084. and 0.041. The mean differences are less than 0.37, 0.38, and 0.43 HRC points. These differences are close to the known limits of Rockwell hardness testing repeatability

[102], and should be viewed with some skepticism especially given that the overall results do not display any easily explainable trends.

Table 11. One-way ANOVA on Rockwell hardness between builds

Source	DoF	SS	MS	*F*	*p*
Factor	3	0.94	0.31	3.37	0.032
Error	28	2.60	0.09		
Total	31	3.54			

Sum of squares (SS) and mean square (MS) are presented in [HRC^2].

Table 12. Tukey-Kramer comparison Rockwell hardness between builds

	Lower C.B.	Mean diff.	Upper C.B.	
Comparison		[*HRC*]		*p*
A1-A2	-0.78	-0.37	0.05	0.099
A1-A3	-0.40	0.01	0.43	1.000
A1-A4	-0.35	0.06	0.48	0.976
A2-A3	-0.04	0.38	0.79	0.084
A2-A4	0.01	0.43	0.84	0.041
A3-A4	-0.37	0.05	0.47	0.988

Rockwell hardness testing results are further detailed in Figure 15. Two measurements per specimen spatial origin are presented, one representing all averaged measurements from tests sites 1, 2, and 3 across all builds and the other from tests sites 4, 5, and 6 across all builds. This produces a map of 10 hardness measurements across the build plate. The presented map indicates the lowest hardness in the center of the build plate and increasing hardness towards in the positive and negative Y directions. LPBF processes are known to vary spatially, with the most noticeable variations at the X and Y extremes of the build area. In this case, the process aspect that might be suspect would be meltpool size and thermal conditions. The laser in an LPBF machine such as an EOS M290 travels the furthest distance to reach the build area and additionally the beam spot shape is most distorted at the limits of the build area. Several other researchers have worked on hardness mapping across the build area, producing mixed results [55]. That said, a close statistical

interrogation of the hardness results does not allow for any conclusive statements as to hardness variation by component spatial origin. A one-way ANOVA was conducted on the data, organized by spatial origin, and results are reported in Table 13. The data was found to be normally distributed, with some notable discrepancies towards the tails of the distribution. The variances homogenous, with Levene's test on the data producing a *p*-value of 0.055. It seems further investigation would be required to definitely prove or disprove an effect of spatial origin on hardness. In either case, the measured differences are very small; less than 1 *HRC* point between extremes.

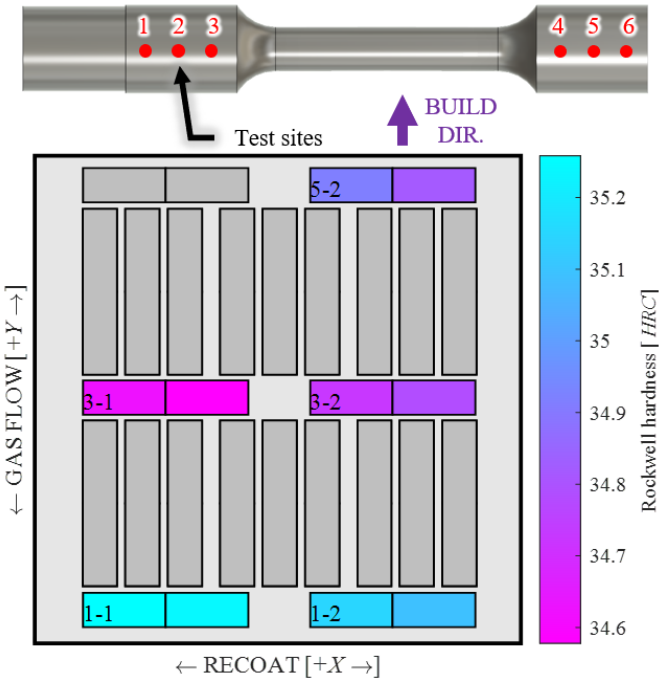

Figure 15. HRC hardness as measured by probing transverse to the build direction on the machined grip areas of select specimens. Three measurements were taken on each grip section, sites 1-3 on the –X end and sites 4-6 on +X end of the specimen. Results from each end are averaged across all builds.

Table 13. One-way ANOVA on Rockwell hardness between spatial origins

Source	DoF	SS	MS	*F*	*p*
Factor	9	2.08	0.23	2.01	0.076
Error	28	3.21	0.11		
Total	37	5.29			

Sum of squares (SS) and mean square (MS) are presented in [HRC^2].

4.5 Quasi-static tensile properties

Tensile tests displayed excellent repeatability in the general form of their stress-displacement profiles, pictured in Figure 16. Results from specimen A4-2-6 have been identified as an outlier data point, with no clear explanation. Exhibited yield was over 4.5 standard deviations lower than the grand mean of all additive tensile tests. As such, this data point is not included in any analyses. For closer examination, a stress-strain curve typical of both the additively manufactured and wrought specimens are presented in Figure 16b. The additively manufactured specimens exhibit a lesser degree of strain hardening and lower elongation both of which indicated the absence of large amounts of retained austenite [59], [60]. They also have a higher yield and ultimate strength, all features typical in additive materials partly due to the characteristic Hall-Petch strengthening as a result of the fine grain sizes produced by the high cooling rates [10], [59]. The specimens did undergo static recrystallization during solutionizing, but their beginning grain size will have influenced the fineness of the produced martensite. The superior yield and ultimate strengths are also indicative of an aging process that effectively enabled precipitation hardening. Further factors to consider when explaining the differences between the LPBF and wrought tensile properties include composition and response to heat treatment. Notably, manufacturer-provided material certifications show that the wrought material tests contained 0.026% C whereas the virgin powder has been noted as containing 0.06%

C – both contain an identical amount of Cu, 3.240%. This difference in carbon content contributes to the formed martensite being harder and stronger for the LPBF material as a result of greater dislocation density. Additionally, if the LPBF material starts with a finer austenite grain size it will have a finer martensite structure and the diffusion kinetics that govern precipitation during aging will act differently in the two materials.

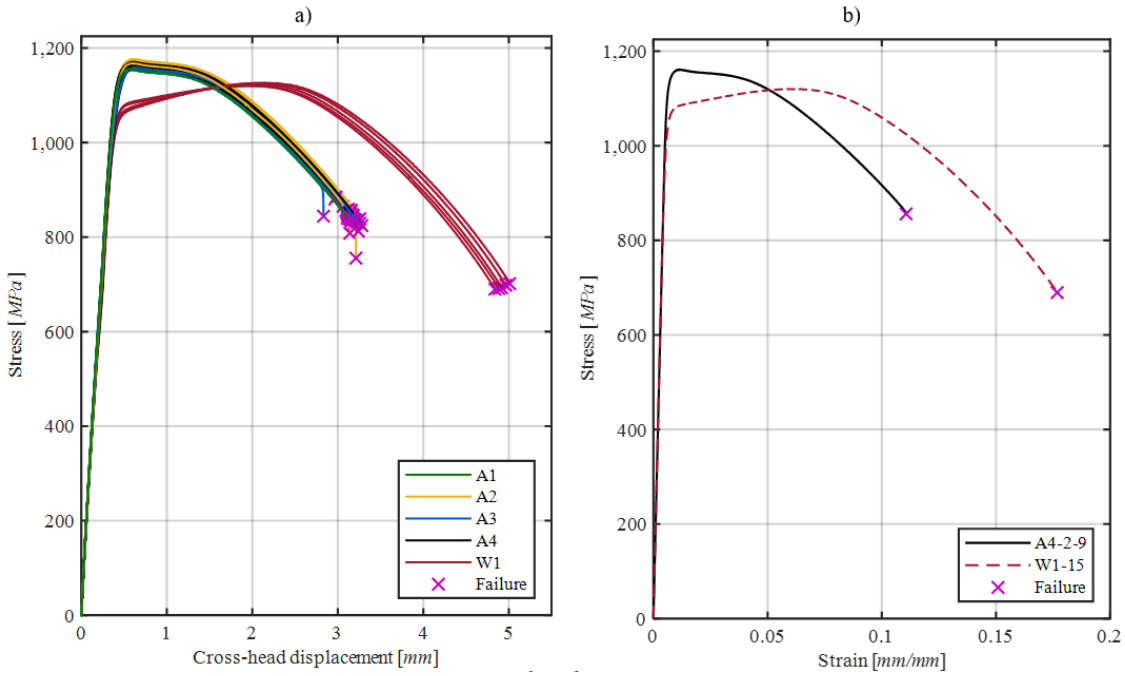

Figure 16. a) Engineering stress vs. cross-head displacement as measured by an in-line load cell and in-line LVDT for all tesed AM and wrought specimens. b) Engineering stress vs. engineering strain as measured by an in-line load cell and a contact extensometer for two specimens with performance typical the AM and wrought specimens.

Yield strength and ultimate strength are presented in Figure 17. A one-way analysis of variance (ANOVA) was utilized to test for differences between yield and ultimate strengths between groups A1, A2, A3, and A4. Yield strength data is approximately normally distributed, with minor deviations in the tails of the data. Levene's test on the data produces a *p*-value of 0.020 but considering that Bartlett's test produces a *p*-value of 0.28 it is difficult to rule the variances as definitely homogenous or not. In the case of

ultimate strength, the data was found to be normally distributed with some deviations in the tail regions, and the variances homogenous as indicated by the *p*-value of 0.406 produced by Levene's test. The results are presented in Table 14 and Table 16, respectively. Both tests display very low *p*-values, indicating that the null is disproven with high confidence and at least one group differs from the others. To further parse these results, a Tukey-Kramer analysis was conducted. Results are displayed in Table 15 and Table 17, respectively. It is found that A2 displays significantly greater yield and ultimate strength compared to all other builds. The mean of the yield strength of specimens from A2 are 6.28, 8.46, and 6.76 *MPa* higher than the mean strengths of builds A1, A3, and A4, respectively. Similarly, the ultimate strengths are 9.60, 10.14, and 7.37 *MPa* higher. Due to the sole outstanding nature of A3 tests this is not expected to be a function of powder condition, nor would prior work indicate that powder condition is expected to greatly affect tensile properties. It would seem a stochastic variation in the LPBF process could be associated with build A3 and can be attributed with the minor albeit statistically detectable differences shown.

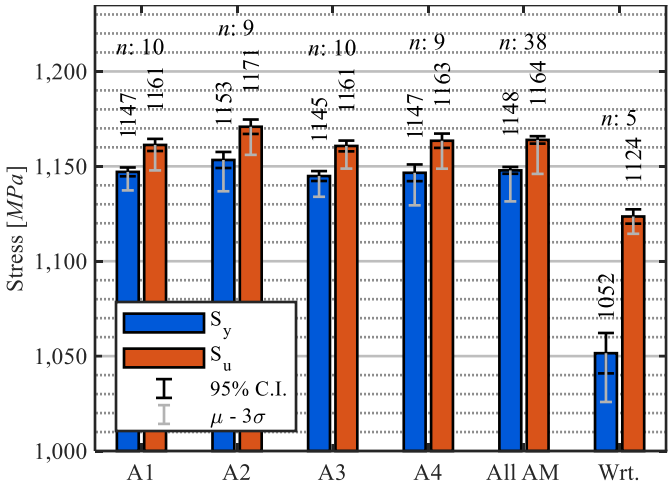

Figure 17. Yield and ultimate strength, S_y and S_u, for each group of specimens. The data reported for 'All AM' specimens corresponds to statistics that summarize groups A1, A2, A3, and A4 when considered together. 95% confidence intervals are calculated via the relevant t-statistic multiplied by standard error. The mean value minus three standard deviations is presented to predict the lower-bound of performance.

Table 14. One-way ANOVA on yield strength, S_y

Source	DoF	SS	MS	*F*	*p*
Factor	3	3.80E+14	1.27E+14	6.01	0.002
Error	34	7.18E+14	2.11E+13		
Total	37	1.10E+15			

Sum of squares (SS) and mean square (MS) are presented in [Pa^2].

Table 15. Tukey-Kramer comparison of yield strength, S_y

	Lower C.B.	Mean diff.	Upper C.B.	
Comparison		[*MPa*]		*p*
A1-A2	-11.98	-6.28	-0.58	0.026
A1-A3	-3.37	2.19	7.74	0.714
A1-A4	-5.22	0.48	6.19	0.996
A2-A3	2.76	8.46	14.17	0.002
A2-A4	0.91	6.76	12.61	0.018
A3-A4	-7.40	-1.70	4.00	0.851

Table 16. One-way ANOVA on ultimate strength, S_u

Source	DoF	SS	MS	*F*	*p*
Factor	3	6.08E+14	2.03E+14	9.70	<0.000
Error	34	7.10E+14	2.09E+13		
Total	37	1.32E+15			

Sum of squares (SS) and mean square (MS) are presented in [Pa^2].

Table 17. Tukey-Kramer comparison of ultimate strength, S_u

Comparison	Lower C.B.	Mean diff. [*MPa*]	Upper C.B.	*p*
A1-A2	-15.27	-9.60	-3.93	<0.000
A1-A3	-4.98	0.54	6.06	0.993
A1-A4	-7.90	-2.23	3.45	0.716
A2-A3	4.46	10.14	15.81	<0.000
A2-A4	1.55	7.37	13.19	0.008
A3-A4	-8.44	-2.76	2.91	0.559

Elongation was analyzed in a similar manner. The data was found to be approximately normal, with several outlier observations, and the variances potentially not homogenous, shown by the *p*-value of 0.0026 reported by Levene's test. This is likely due to the relatively small sample size and outlier observations typical to elongation measurements. As such, the results of the applied statistical tests should be viewed with some skepticism. A one-way ANOVA on the elongation of groups A1, A2, A3, and A4, shown in Table 18, reveals a result on the edge of statistical significance, with a *p*-value of 0.06. Upon closer inspection via a Tukey-Kramer comparison shown in Table 19, this may be attributed a combination of even less significant differences between groups A1 and A3, and A2 and A3 with individual comparison *p*-values of 0.099 and 0.153. Due to the low *p*-values of these individual comparisons, it is concluded that no significant effects of powder condition on elongation can be detected. Note that a limited number of tests could be analyzed for each group, given a lack of strain data past yield for a handful of specimens. Sample sizes are noted in Figure 18.

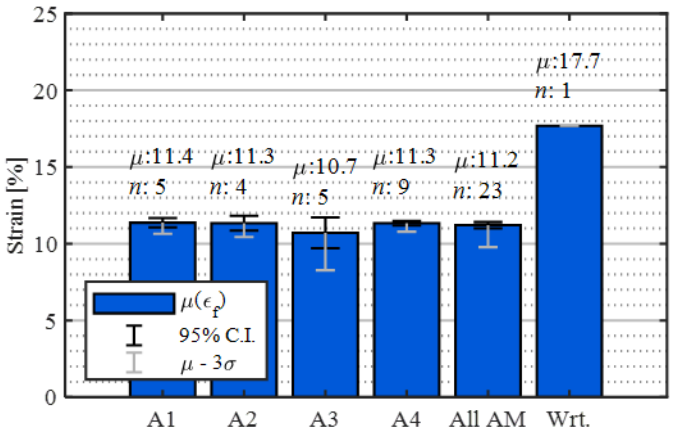

Figure 18. Elongation at failure, ε_f, for each group of specimens presented as a percent value. The data reported for 'All AM' specimens corresponds to statistics that summarize groups A1, A2, A3, and A4 when considered together. 95% confidence intervals are calculated via the relevant t-statistic multiplied by standard error. The mean value minus three standard deviations is presented to predict the lower-bound of performance.

Table 18. One-way ANOVA on yield strength, ε_f

Source	DoF	SS	MS	*F*	*p*
Factor	3	1.58E-04	5.28E-05	2.94	0.060
Error	19	3.42E-04	1.80E-05		
Total	22	5.00E-04			

Sum of squares (SS) and mean square (MS) are presented in [(mm/mm)^2].

Table 19. Tukey-Kramer comparison of yield strength, ε_f

	Lower C.B.	Mean diff.	Upper C.B.	
Comparison		[%]		*p*
A1-A2	-0.77	0.03	0.83	1.000
A1-A3	-0.09	0.66	1.41	0.099
A1-A4	-0.63	0.04	0.70	0.998
A2-A3	-0.17	0.63	1.43	0.153
A2-A4	-0.71	0.01	0.73	1.000
A3-A4	-1.29	-0.62	0.04	0.072

Modulus is presented in Figure 19. A one-way ANOVA on the elongation of groups A1, A2, A3, and A4, shown in Table 20, revealed no significant difference, with a *p*-value of 0.683. The data was found to be normally distributed, with some deviations at the tails, and the variances homogenous, with Levene's test producing a *p*-value of 0.92. Interestingly, the additively manufactured material had a somewhat higher modulus than

the wrought comparison. This is not an effect of higher porosity content influencing the apparent modulus, as this would actually lower the measured stiffness due to a reduction in cross sectional area. Modulus is a complex property depending on many variables and as such a further insight cannot be provided in this context.

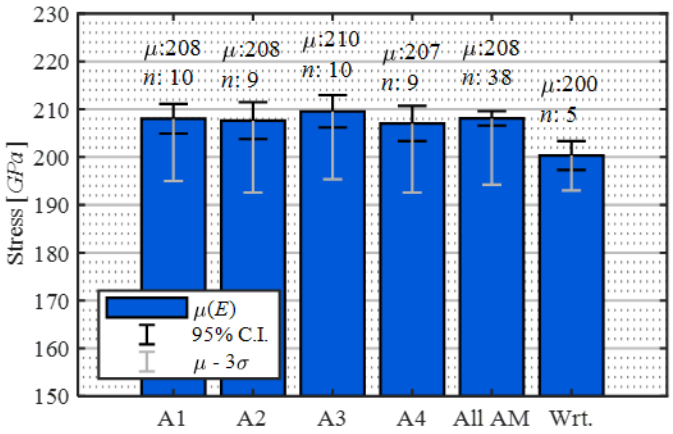

Figure 19. Modulus, E, for each group of specimens. The data reported for 'All AM' specimens corresponds to statistics that summarize groups A1, A2, A3, and A4 when considered together. 95% confidence intervals are calculated via the relevant t-statistic multiplied by standard error. The mean value minus three standard deviations is presented to predict the lower-bound of performance.

Table 20. One-way ANOVA on modulus, *E*

Source	DoF	SS	MS	*F*	*p*
Factor	3	3.35E+19	1.12E+19	0.50	0.683
Error	34	7.57E+20	2.23E+19		
Total	37	7.90E+20			

Sum of squares (SS) and mean square (MS) are presented in [Pa^2].

Tensile tests exhibited a stress-strain curve typical of a fairly plastic strain-hardening metal and examination of the fracture surfaces, shown in Figure 20, support this finding. Significant necking prior to final failure is present, as can be seen in a specimen whose test was halted prior to final failure. Facture surfaces show a classic cup-and-cone structure, indicating ductile failure. SEM fractographs in Figure 21 support this claim, with ductile dimples observed in both additively manufactured and wrought specimens.

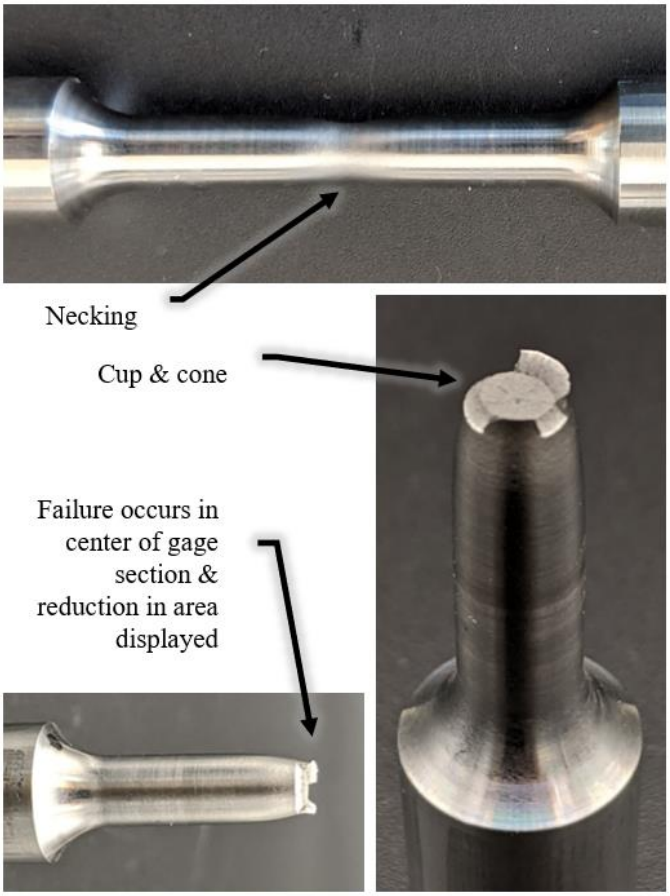

Figure 20. Typical characteristics of a static tensile failure in an AM specimen.

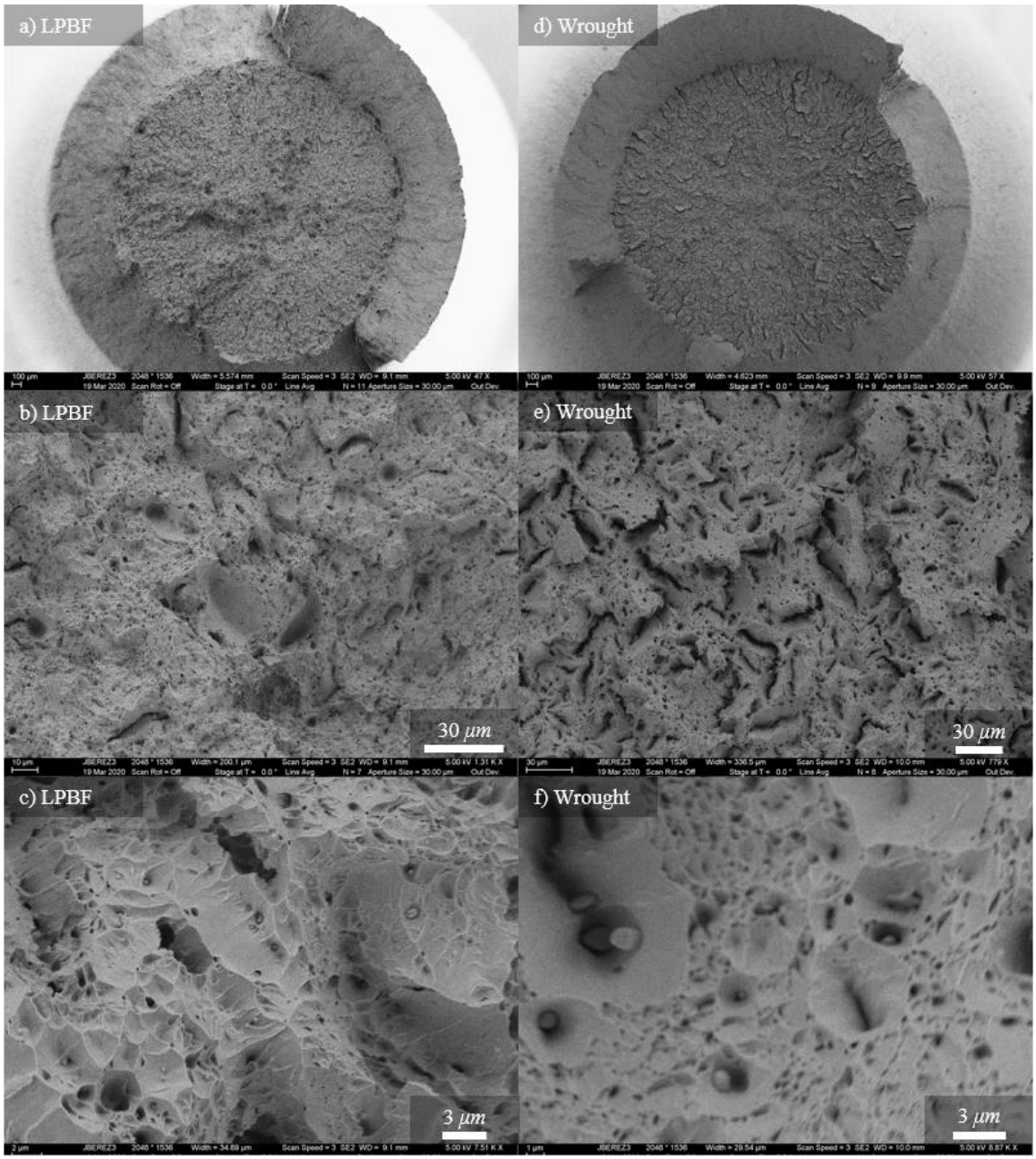

Figure 21. Figures a-c, SEM fractographs of specimen A1-2-4. Figures d-f, SEM fractographs of specimen W1-15.

4.6 Fatigue properties of produced components

4.6.1 Fatigue life a function of powder condition

Four initial tests on specimen 2-2 of each build were conducted at various stress levels and loading ratio of $R = 0.1$, these tests were used to select a loading criterion of S_{max} = 867 MPa. A simple linear least-squares fit to the data, where N_f was transformed to $\log(N_f)$, was used to select a load that would produce failure towards the lower end (N_f = ~350,000) of the HCF regime. All subsequent tests were conducted under these conditions. As stated, prior work predicts the most sensitive response to processing conditions in this regime. Interestingly, as seen in Figure 22 the subsequently executed tests do not closely follow the predicted *S-N* curve, which vastly overpredicts performance.

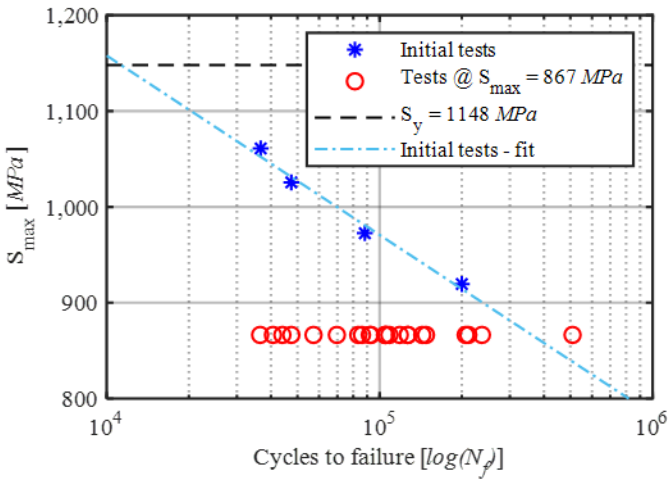

Figure 22. S-log(N_f) plot, for R = 0.1, displaying data corresponding to both initially conducted tests and the extended testing conducted at a fixed stress level. The initially conducted tests were on specimen 2-2 from A1, A2, A3, and A4.

In order to answer the main research question of this work, results are organized by build and presented in Figure 23. A significant amount of variation within each group is evident. Fatigue lives vary from roughly 30,000 to 500,000 cycles between all the groups. A visual examination the plotted data does not reveal any easily detectable differences.

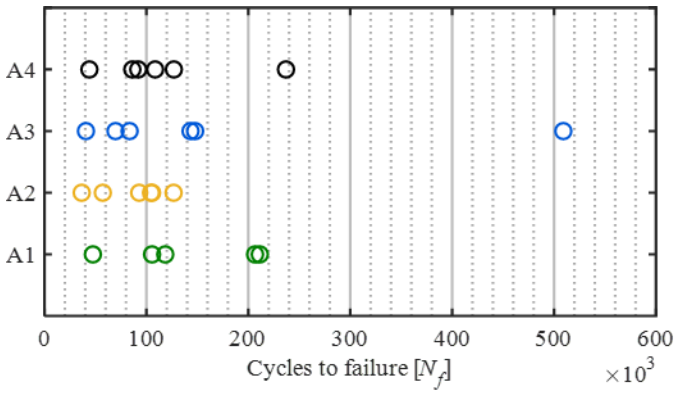

Figure 23. Fatigue life of all specimens tested at S_{max} = 867 MPa, R = 0.1 organized by builds A1, A2, A3.

In order to distinguish the data, the non-parametric empirical survival function, was calculated for each group. Results are presented in Figure 24a) where the probability of survival past *N* cycles is presented as a function of *N*. Greenwood's formula for variance was used to calculate confidence bounds on the functions for groups A1 and A4 shown in figure Figure 24b. Neither figure shows easily detected differences between the groups. The confidence bounds in Figure 24b overlap considerably.

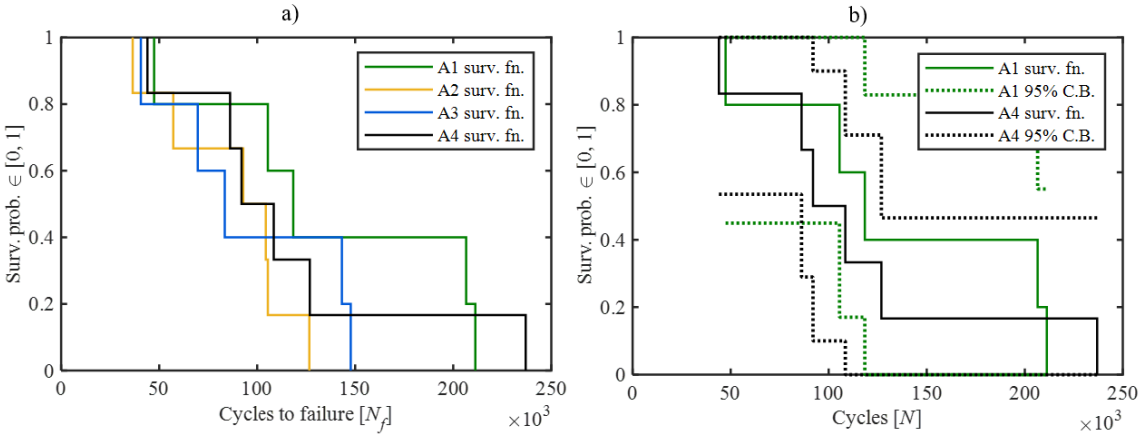

Figure 24. a) Survival functions as estimated by the Kaplan-Mier method for specimens tested at S_{max} = 867 MPa, R = 0.1 for groups A1, A2, A3, and A4. b) Survival for groups A1, and A4. 95% confidence bounds derived by Greenwood's formula.

The log-rank test was applied in order to further compare the respective survival functions. The null assumes that all groups hail from a population with the same survival

function, and the alternate states that at least one group has a survival function distinct from the others. The test considers data from all four groups as a single set to calculate survival function should the null be true. Using this function, the expected survival probability was calculated at each recorded point of failure for the four groups and compared to actual number of failures at each point for each group. All four tests were considered simultaneously, and the log-rank test produced a chi-squared statistic of 2.43, corresponding to a *p*-value of 0.49 when compared to the critical chi-squared value of 6.25 for $\alpha = 0.10$ and $k = 3$ degrees of freedom. The null hypothesis holds, and no difference between the four groups' survival functions was detected.

In order to conduct a parametric analysis of the gathered life data, an exploratory data analysis was first conducted to choose the appropriate descriptive distribution. Figure 25 displays the data on probability plots corresponding to normal, exponential, extreme value, lognormal, and Weibull distributions. With the non-parametric analysis indicating a lack of great difference between the groups, all four are considered at once for the sake of choosing a common underlying model. These plots display probability of failure as a function of life on non-linear axes that would arrange the data on a line should they accurately model the underlying distribution. Notably, failure of specimen A3-2-8, which failed at 509,052 cycles, was not accounted for by any of the five considered distributions, with the normal, exponential, and extreme value distributions severely under-estimating its probability. In order to better visualize how well the various distributions model data in lower life regimes this data point was removed from Figure 26. The probability plots for the lognormal and Weibull distributions show the data fairly linearly, distribute the data evenly, and provide a fairly accurate model for specimens that displayed a lower life, an

important aspect since these specimens provide a lower bound to performance. The normal and extreme value distributions have weaknesses with modeling specimens displaying a higher life. The exponential distribution shows some promise, but as it is a reduction of the more complex Weibull distribution, and does not show a significantly better fit than the more general Weibull distribution it does not provide any significant strengths. Given the historical basis for modeling fatigue data with Weibull and lognormal distributions, these distributions are selected for further analysis. Due the difficulty of describing the life of specimen A3-2-8, this data point is considered as an outlier for subsequent parametric analysis methods and not used in following calculations. The results of this exploratory data analysis also informed the earlier described non-parametric approach, and this outlier data point was not considered there, either.

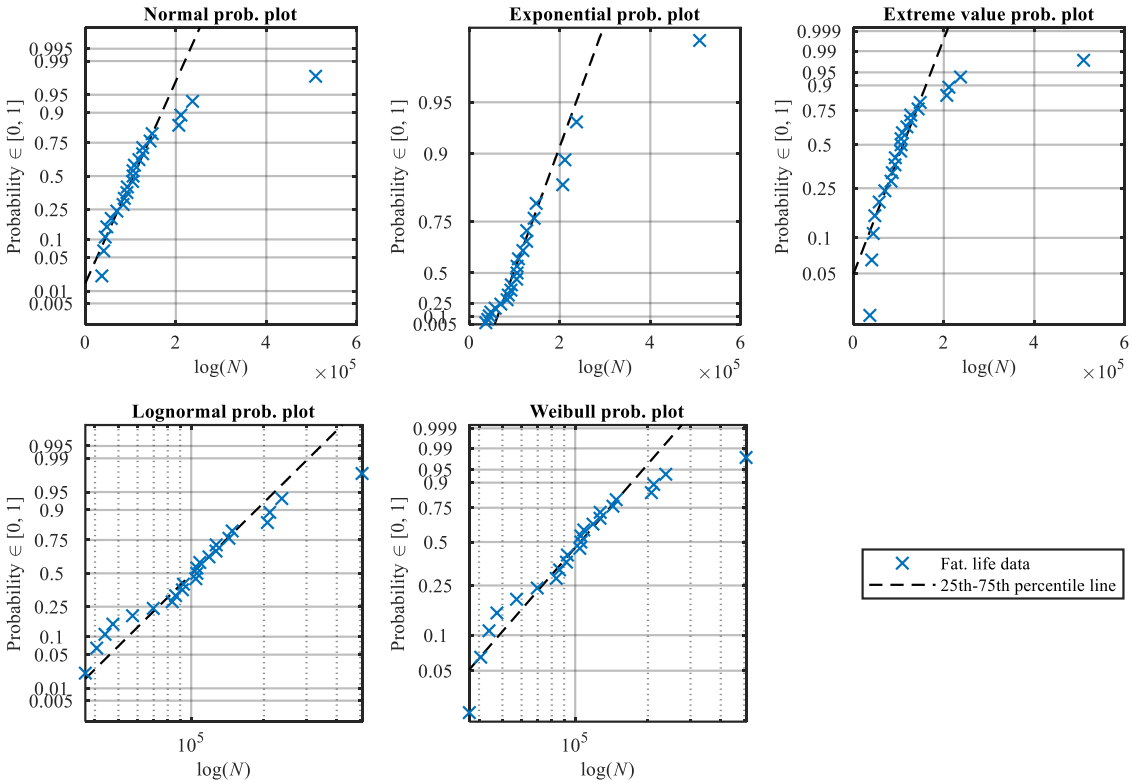

Figure 25. Probability plots of five distribution types using the life data for tests conducted at S_{max} = 867 MPa and R = 0.1. Note that the fit line is merely provided as a judge of linearity and is determined by intersecting the 25th and 75th percentiles of the data. Outlier data point N_f = 509,052 for specimen A3-2-8 is included.

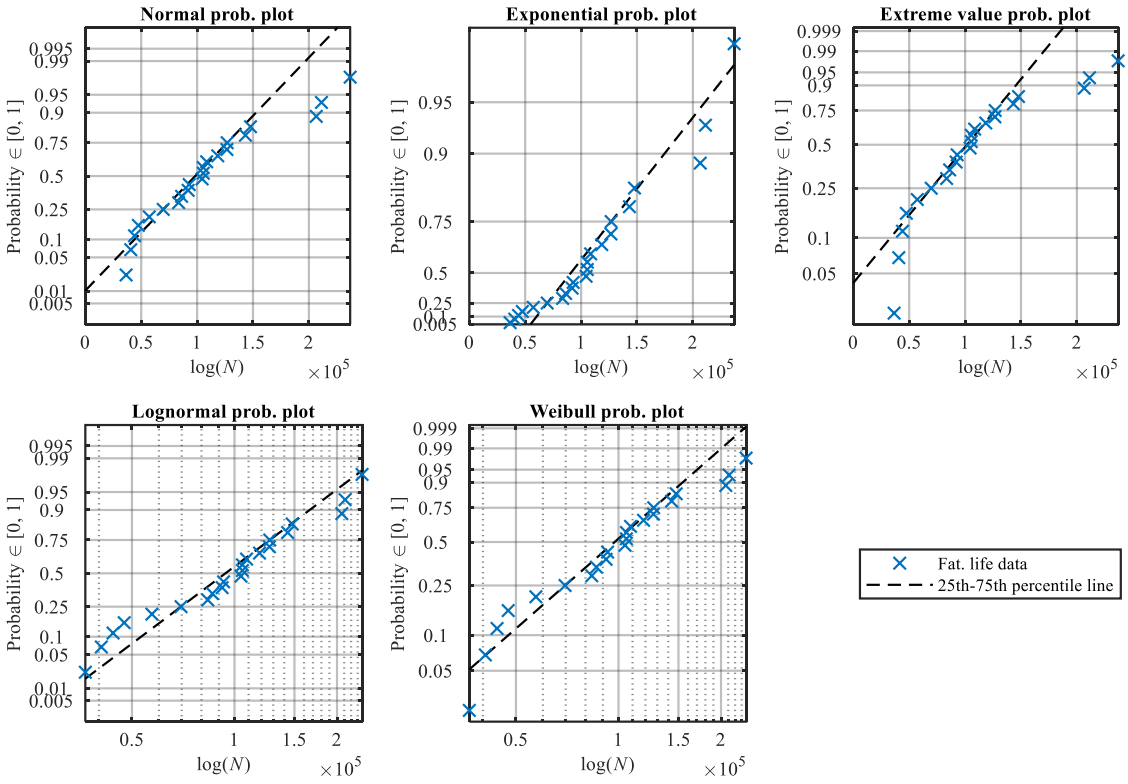

Figure 26. Probability plots of five distribution types using the life data for tests conducted at S_{max} = 867 MPa and R = 0.1. Note that the fit line is merely provided as a judge of linearity and is determined by intersecting the 25th and 75th percentiles of the data. Outlier data point N_f = 509,052 for specimen A3-2-8 is excluded.

One weakness of the two down-selected distributions is that neither has a definite lower bound, meaning data with a value of zero has a finite probability of occurring. An interesting variation on the Weibull distribution to consider that accounts for this is the three-parameter Weibull distribution, described by equation (12).

$$P(x) = \frac{\beta}{\eta}\left(\frac{x-\gamma}{\eta}\right)^{\beta-1} exp\left[-\left(\frac{x-\gamma}{\eta}\right)^{\beta}\right] \tag{12}$$

This distribution is simply a shift on the conventional Weibull distribution by the value γ, and thus produces a lower bound that can be based in a physical understanding of the modeled phenomena. To test the fitness of this distribution several potential values of γ were subtracted from the life data set, and then plotted on Weibull probability plots shown

in Figure 27. Should a three parameter Weibull distribution be a better model the data would appear as more linear. Values of γ = 0, 10,000, 20,000, and 30,000 were tested, corresponding to a limit on the lower bound of life of the same value. None of the three non-zero values created significantly more linearity in the plots, and thus a three parameter Weibull distribution was excluded from further analysis.

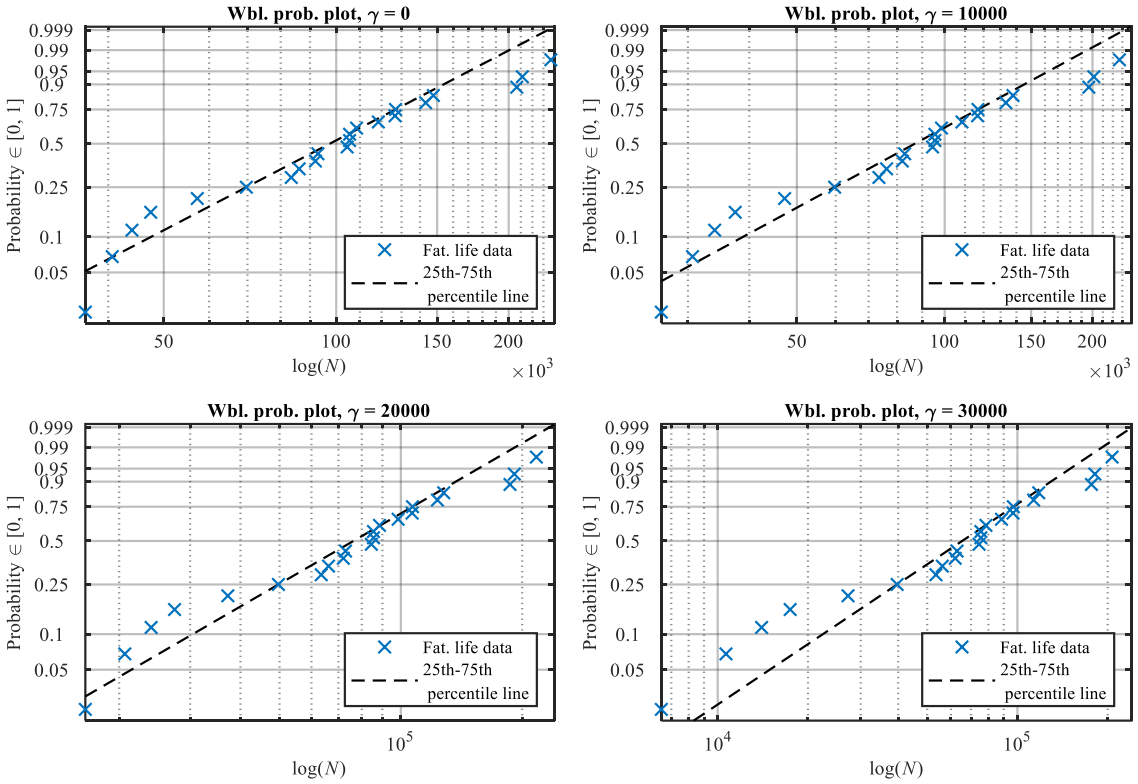

Figure 27. Probability plots testing the effect of various values of a shift parameter, γ, in a three parameter Weibull distribution. Shift parameter values of 0, 10,000, 20,000, and 30,000 cycles are tested. Note that the fit line is merely provided as a judge of linearity and is determined by intersecting the 25th and 75th percentiles of the data.

Having selected the appropriate models for the fatigue lives displayed by the four groups of data, a comparison between fitted models was undertaken. To begin, lognormal and Weibull distributions were fit to each of the four sets of data via MLE, using the MLE tools integral to the computation software package *Matlab*. The outcome was parameter estimations for each distribution, in addition to asymmetric confidence intervals based on

the sample size and variability of the data, displayed in Figure 28. Group A1 shows both the highest log-mean and scale for the lognormal and Weibull distributions, respectively. In both cases this indicates that the fitted distribution for A1 is shifted further in the direction of longer life, although differences in the log-standard deviation and shape parameters between groups may influence the actual arithmetic mean of the fitted distributions in the other direction. The large overlap of the confidence intervals for all parameters for both distribution types does not encourage drawing any conclusions on model differences at this point.

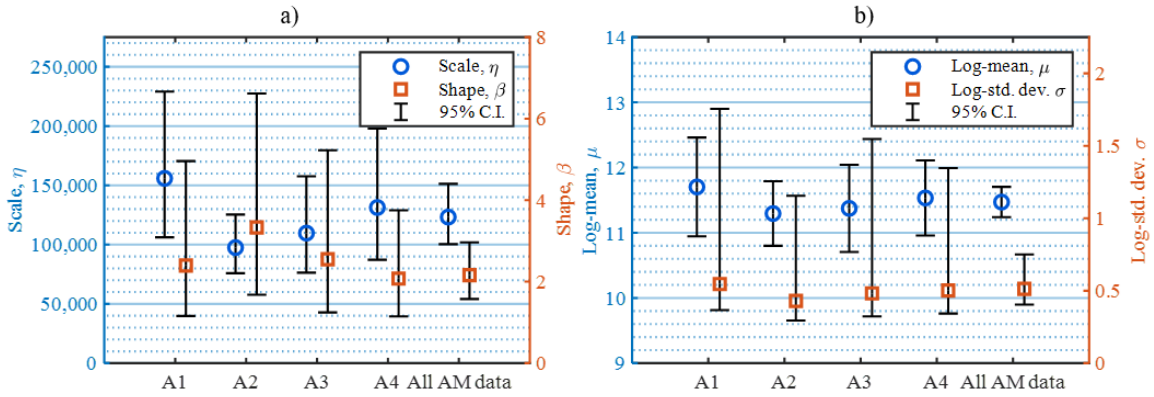

Figure 28. The estimated parameters correspond to tests conducted at S_{max} = 867 MPa and R = 0.1 for groups A1, A2, A3, A4, and all groups considered as a single set of data. a) Lognormal parameters determined by maximum likelihood estimation. b) Weibull parameters determined by maximum likelihood estimation.

To additionally distinguish the fitted distributions they were plotted on probability plots and their MLE parameters were used to draw lines that represent the fitted underlying distributions. These probability plots use the maximum likelihood estimates to draw these lines, not the crude linear judge previously shown that connects the 25th and 75th percentiles of the data. Figure 29 shows this for both cases of the fitted lognormal and Weibull distirbutions. The high log-mean and scale of group A1 is again evident by noticing the right shift in the line representing the estimated disribution for A1. Both plots suggest, in

order, that the log-mean and scale increases from group A2 to A3 to A4 to A1. This order does not seem to imply an accompanying trend in fatigue life as the degree of repeated process exposure increases other than the A1 group displaying the most favorable estimated log-mean and scale. While the lognormal probability plot shows very similar slopes between the esitmated distirbutions, indicating similar log-standard deviations, the Weibull probabilty plot suggests that A2 may have a distinct shape parameter due to its somewhat higher slope when compared to the other distribution estimates. This would mean the PDF shape proceeds from an exponential to a bell-shaped curve and that the area under the estimated A2 PDF is lesser at lower life, implying a higher probability for specimens from A2 to display a higher life.

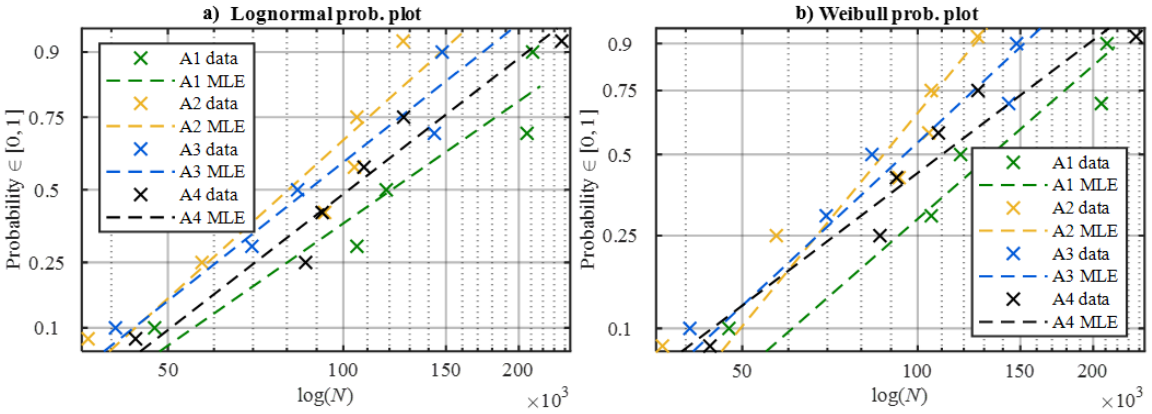

Figure 29. Data collected from groups A1, A2, A3, and A4 for tests conducted at S_{max} = 867 MPa and R = 0.1. a) Lognormal probability plot with lines corresponding to the respective MLE distributions of each group. A right shift in a corresponds to an increase in the log-mean and a decrease in slope corresponds to an increase in the log-standard deviation. b) Weibull probability with lines corresponding to the respective MLE distributions of each group. A right shift in a corresponds to an increase in the scale parameter and an increase in slope corresponds to an increase in the shape parameter.

A qualitative insight into the deviations between the estimated distributions for each group is now established. The likelihood ratio test was then used to produce a definitive comparison via a binary indication of pairwise difference between the groups. Having

already calculated the maximum likelihood parameter estimates for each group it is relatively simple to extract the likelihood value associated with each estimate, again using software tools integral to the computational software package *Matlab*. The likelihood ratio test can only be utilized for comparisons between two models at a time, so six pair-wise comparisons were performed to detect possible differences between all of the four groups. In each case the null assumes that the two compared groups hail from the same underlying population and thus a maximized likelihood was additionally calculated for the set of data that contains the results from both compared groups. The likelihood of this estimation was then compared to the sum of the likelihoods for the individual estimates for each compared group via the likelihood ratio test to produce the relevant test statistic. In this case a value was produced that was compared to the chi-squared distribution with $k = 2$ degrees of freedom, indicating that the unrestricted (alternate) model uses two more free parameters than the restricted (null) model. This applies in both the cases of the Weibull and lognormal distributions, as both distributions are fully described by two parameters each, and when comparing a model made up of two distributions to a single one the difference in unrestricted parameters is 2. The significance level used for this test is $\alpha = 0.10$, which was used to calculate the critical test statistic value. The results of each pair-wise comparison are presented in Table 21. None of the comparisons produced a test statistic that meets the chosen significance level although the A1-A2 comparison produces a *p*-value of 0.11 alluding to possible difference. This finding is supported by the qualitative interpretations of the estimated distributions for these two groups, implying that they are spread the furthest apart. However, in the case of the Weibull distribution, the PDF estimation for A2 is less right-skewed than A1, which somewhat counteracts the supposed shift between the

two estimated distributions. Overall, no definitive difference is detected between any of the four groups.

Table 21. Likelihood ratio test results

	Lognormal estimation			Weibull estimation		
Comparison	X^2	hyp.	*p*	X^2	hyp.	*p*
A1-A2	1.92	0	0.383	4.49	0	0.106
A1-A3	0.87	0	0.647	1.74	0	0.419
A1-A4	0.16	0	0.923	0.36	0	0.834
A2-A3	0.01	0	0.996	0.79	0	0.673
A2-A4	0.76	0	0.684	3.03	0	0.220
A3-A4	0.13	0	0.936	0.79	0	0.674

X^2_{crit} = 4.61 corresponding to α = 0.10 and k = 2 degrees of freedom. Hyp. = 0 indicates the null.

4.6.2 Fatigue life dependence on spatial origin

While the impacts of powder condition on fatigue life have thus far been presented, with powder condition appearing to not influence fatigue life in the HCF regime, insights generalized to the LPBF process and the 17-4 PH material system can still be made. Of great interest is the implied dependence of fatigue life on the build plate spatial origin of a produced component. Figure 30 displays fatigue life results labeled by specimen number, i.e., spatial origin, and provides a map of the average fatigue life over the build plate.

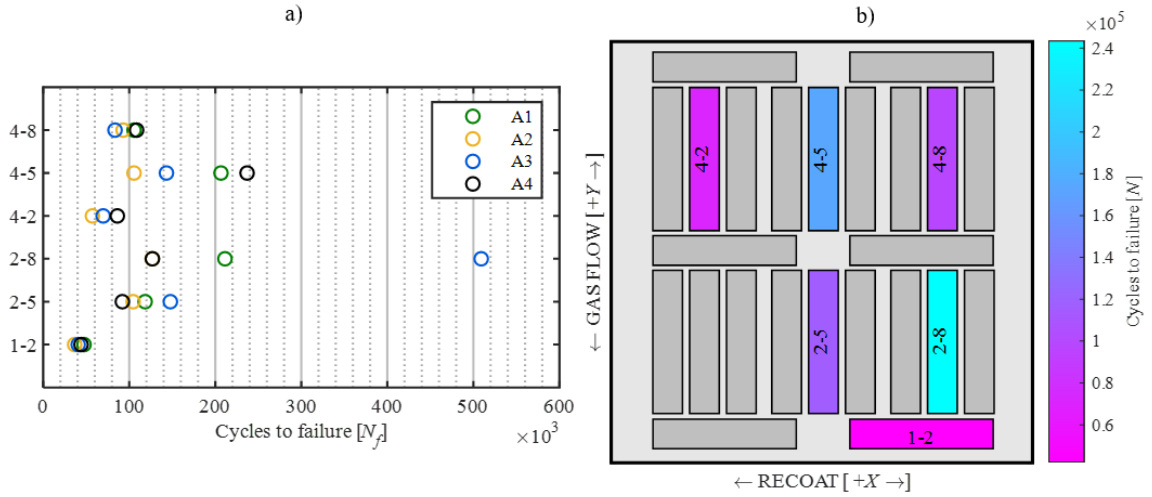

Figure 30. a) Fatigue life of specimens tested at S_{max} = 867MPa, R = 0.1 organized by specimen number, signifying build plate spatial origin. b) Mean cycles to failure, N_f, shown for each set of tested specimens. The mean was taken across the all specimens corresponding to the same spatial origin on the build plate for all builds, where data was available.

Two major observations can be made. First, average fatigue life appears to vary based on spatial origin. Second, variation in fatigue life is heteroscedastic – specimens of a spatial origin that exhibit low fatigue life display low variation while those of a higher typical life display much greater variation. This kind of heteroscedasticity mirrors what is typically expected with a decrease in stress amplitude, as was shown in Figure 2. The portrayed dependence of fatigue life on spatial origin is of great interest, as it would suggest that components with well qualified and defined design and processing parameters may exhibit vastly different fatigue properties should their placement within the build area not be controlled. Typically, this parameter of spatial origin has not been studied in reference to fatigue life and neither does it seem to be greatly emphasized in industry as a process parameter that requires close control [97], [103]. Fatigue life does not appear to exhibit a single trend across any one direction of the build plate. Notably specimens 1-2 and 4-2 have, by far, the lowest fatigue lives of the tested specimens. Specimen 2-8 appears to have, on average, a quite high fatigue life but this result is somewhat influenced by the fatigue

life of specimen A3-2-8, which was earlier identified as an outlier observation. Should this specimen be excluded from the map specimen 2-8 would show a fatigue life still at the high end of the observed fatigue life spectrum, but to a far lesser degree. Specimens with very low average lives (1-2 and 4-2) are notably the tested specimens located furthest in the directions of shielding gas flow and recoater motion, respectively. This observation matches common knowledge of two phenomena observed in the LPBF process. Shielding gas flow is a critical feature of the LPBF process, as the gas serves both purposes of shieling the process zone in addition to clearing process by-products from the build area. The byproducts of the laser welding process, such as meltpool ejecta/spatter and condensate, are both undesirable. The large particles that often are ejected from the meltpool will impact local powder bed density and create voids in the powder bed that may persist in the fusion of subsequent layers, as is theorized in numerous works about powder and part quality relations [5], [57], [58]. Condensate composition will differ from the bulk material and spatter has been shown to have considerable oxide layers [4], [104] – both deleterious to the final component if incorporated. Further, oxides are not always burned off in the laser welding process and may create non-nominal meltpool conditions [104]. Shielding gas flow is supposed to transport these byproducts into a gas receiver nozzle on the other side of the build plate. However, this function is known to be imperfect, with process byproducts frequently settling on the -Y end of the build area [95]. This will incorporate byproducts into the subsequently fused layers of a component, should the recoater not transport them entirely off the build area while spreading the next layer.

Recoater motion is also known to produce effects that may impact produced component quality issues. As identified by several researchers, due to the extremely small

distance between a recoater blade and the powder bed, large particles are preferentially transported across the build area in the direction of the recoat [3], [95]. This may include particles from the hopper as well as particles already present in the build area, such as the large meltpool spatter particles earlier described. In these cases the particles can either be dragged entirely over the build area or dragged over a portion of the build area until powder bed conditions allow them to settle. In the first case shallow valleys may be created in the newly spread powder bed and in the latter large particles can create local powder bed voids. Both situations can lead to porosity in a final produced component. Overall, this phenomenon of mechanical property dependence on spatial origin has been rarely studied with few conclusive relations presented as of yet. Esmaelizadeh identified areas of the build in the direction of gas flow and recoat to have a greater density of large particles [95]. Chua and Chong showed a trend in tensile properties that produced higher strengths trending opposite to the recoat direction and noted a likely non-laminar gas flow in certain regions [97]. Fitzgerald and Everhart found that builds more densely packed with components exhibit lower tensile performance, suggesting the effect of process byproducts [103]. They also noted a decrease in tensile properties in the direction of gas flow. Finally, in the only study known to the author to correlate location with fatigue, Soltani-Tehrani et. al, observed fatigue life reducing in the direction of recoat [58].

An examination of a selection of the specimen fracture surfaces was conducted to provide insight as to the driving factors behind fatigue failure. A depiction of the typical fracture surface topography is presented in Figure 31. Topography was measured with a *Keyence VR-5000* high resolution structured light scanner and analyzed with the accompanying software. The fracture topography is typical of fatigue failure of a ductile

metal. A fracture growth area is plain to see, oriented normal the specimen axis and direction of stress. The growth area shows the region that the crack progressed through due to cyclic loading prior to final failure. Shear lips are evident on either side of the growth area, and minor plastic deformation (localized necking) is noticeable on the free surfaces of the specimen that are close to the shear lips. All tested specimens exhibit a very similar fracture surface topography, with the only major differences being the exact configuration of the shear lips.

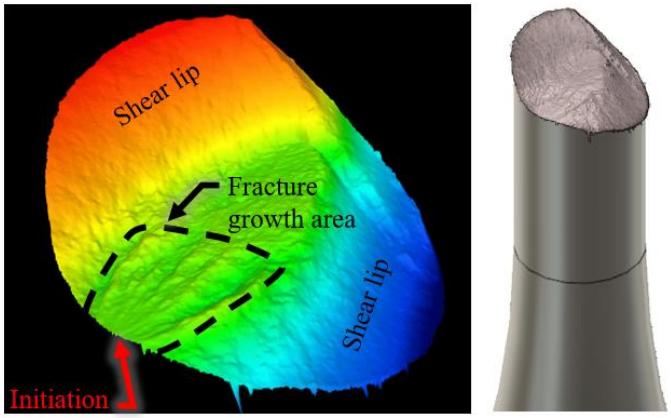

Figure 31. Typical fracture surface topography displayed by tested specimens. On the left the fracture surface topography is presented in detail. On the right, the surface is superimposed on a CAD image of a fatigue specimen.

Extensive imaging of the fracture surfaces of many specimens was conducted via scanning electron microscopy. Due to the similarity in overall topography, focus was given to the fracture growth region and in particular the initiation site. Figure 32 shows images of a fracture growth region and an inset of the identified LoF fracture initiator. All inspected fracture surfaces displayed prominent chevrons and clear topography that identified a single fracture initiation point in a sub-surface region. Nearly all inspected fractures surfaces also show a clear defect at the initiation site. A selection of SEM fractographs are presented in Figure 33 which represent a range of the initiation sites (with the exception of

Figure 33a) seen across the inspected specimens. Figure 34a and b also identify defects at initiation sites. The majority of defects appear to be LoF defects. They can be identified by either the clearly present unfused powders, voids, or a distinct local surface texture that does not show river lines or signs of fracture growth indicating that these defects existed prior fatigue testing. LoF defects that are present at initiation sites have a size range of roughly 25-125 μm. Figure 33a shows a LoF defect in the fracture growth area of one specimen that very clearly shows lack of fusion surrounding what looks to be two scan paths areas, one on top of the other. There was lack of fusion both between layers and in the plane perpendicular to the layer indicating there was a particularly poor powder bed density in this area. Specimen A3-2-8, shown in Figure 34a, which showed the highest observed fatigue life, shows a very small gas pore that looks to incubate into a larger crack before steady crack growth begins. Specimen A4-2-5, shown in Figure 34b, has an unidentified defect present at its initiation site. This defect does not appear to be of the parent material and is more likely a non-metallic inclusion. Figure 34b-f show the initiation site and three significant LoF defects present in the fracture growth surface of specimen A3-1-2. This specimen, which displayed one of the lower observed fatigue lives, displayed a very high concentration of LoF defects in the fracture growth area as compared to other specimens. This would suggest that the fracture growth stage makes up a significant portion of fatigue life in this study, with possibly more rapid growth in this specimen due to multiple large defects in the path of the crack.

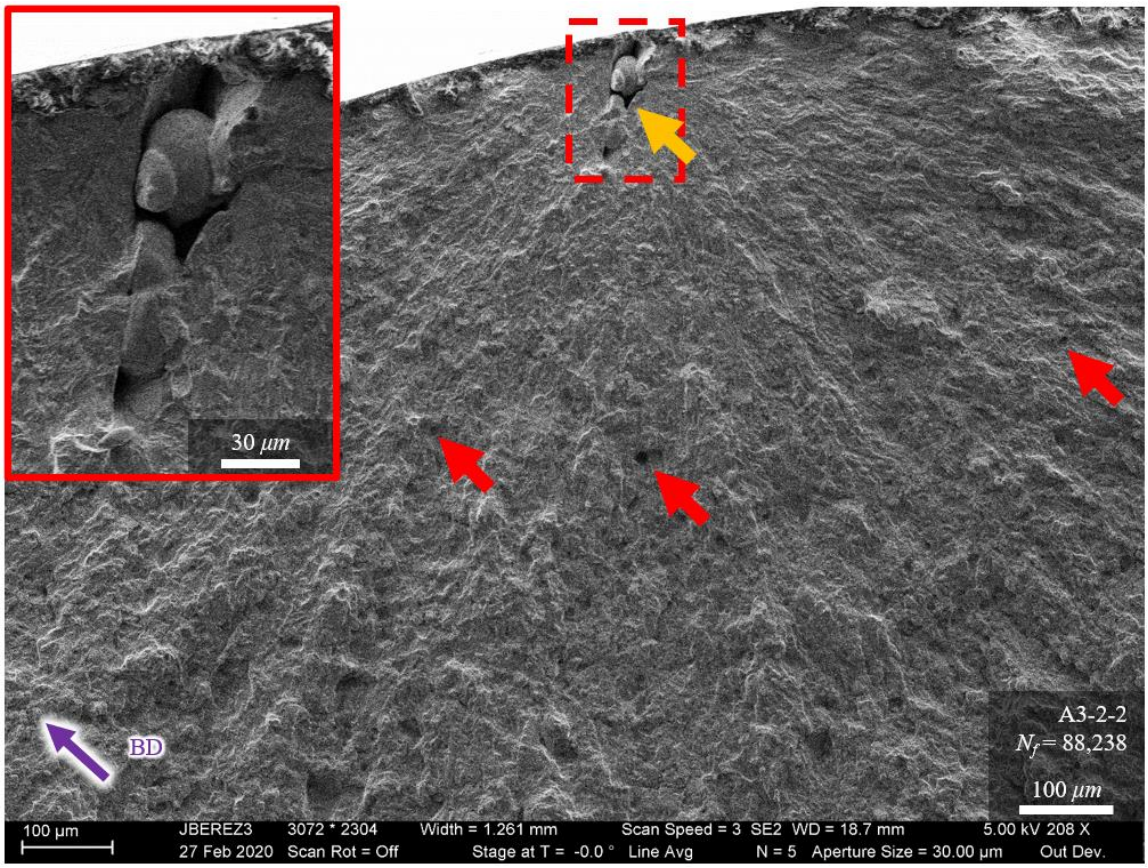

Figure 32. Typical identification of fracture intiator modeeld by specimen A3-2-2. Suspected gas porosity, LoF, and unidentified defects are noted by red, yellow, and blue arrows. The arrow labeled "BD" points in the build direction.

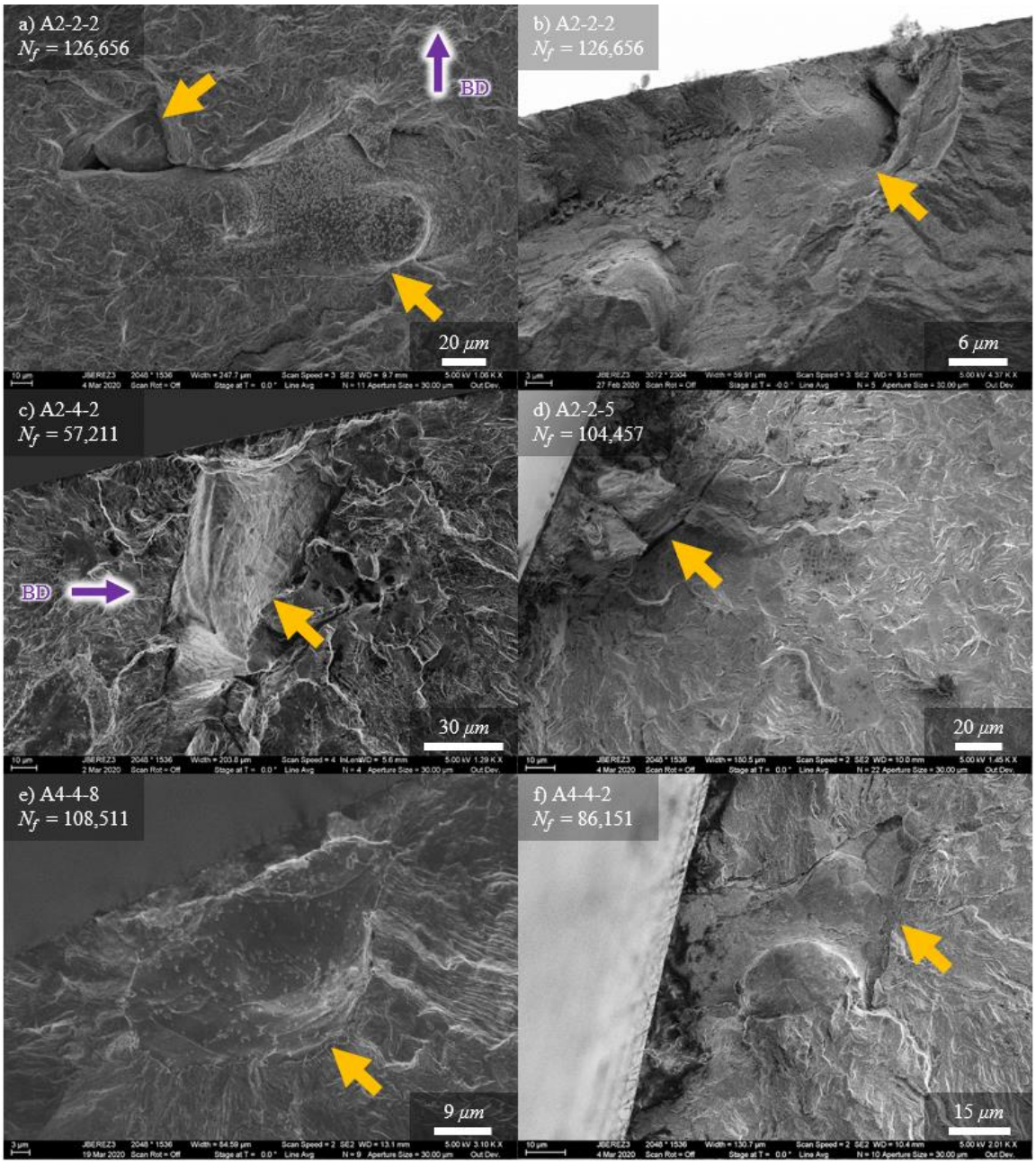

Figure 33. Suspected gas porosity, LoF defects are noted by yellow arrows. The arrow labeled "BD" points in the build direction. Figure a shows defects present in the fracture surface. Figures b-f show defects at the fracture initiaion site.

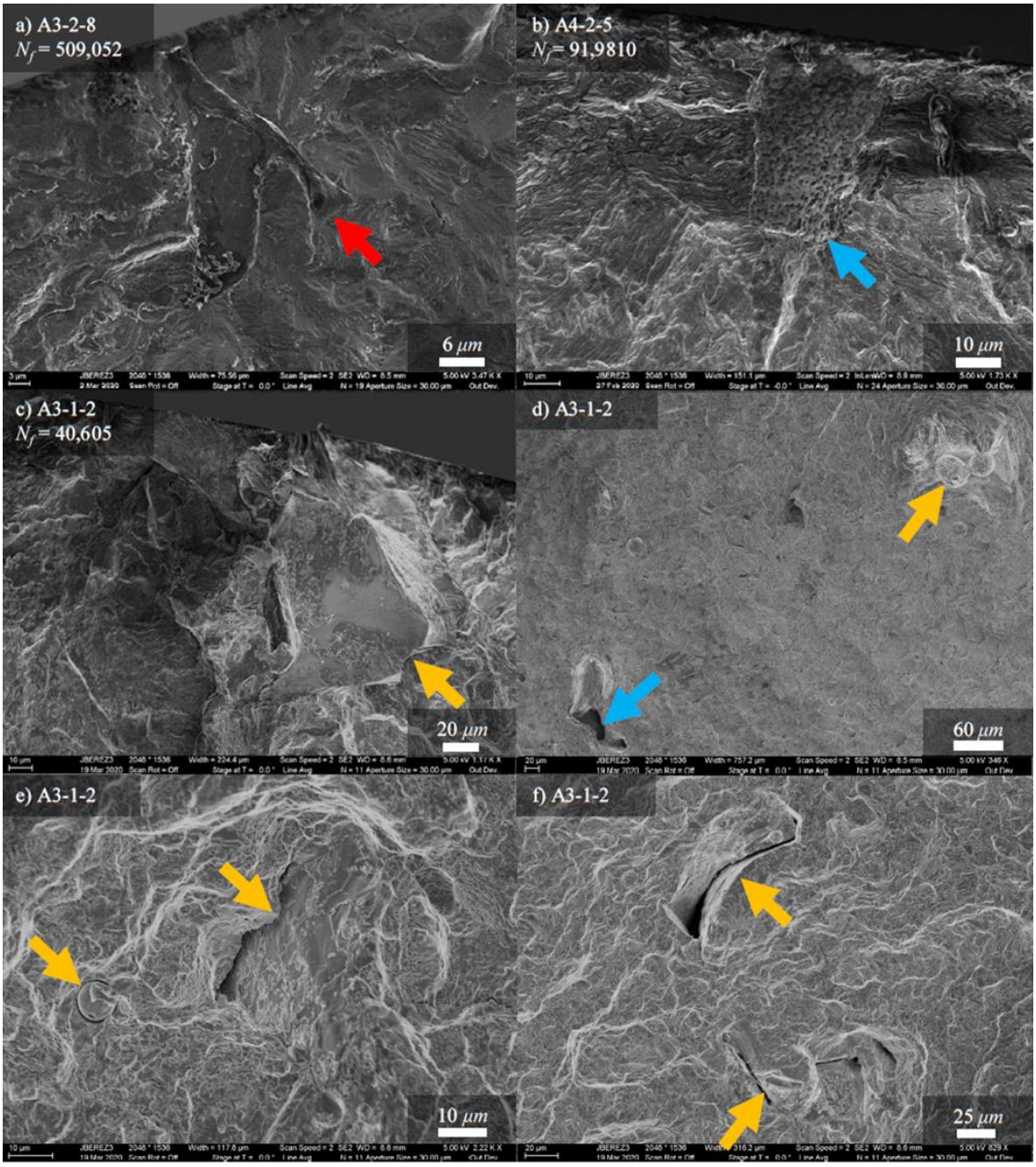

Figure 34. Suspected gas porosity, LoF, and unidentified defects are noted by red, yellow, and blue arrows. Figures a-c show defects at the fracture initiaion site. Figures d-f show defects present in the fracture surface.

4.6.3 Statistical description of all builds as a single population

Given that it has been shown that the powder conditions studied did not drive fatigue properties of the studied builds, it is possible to look at the entire set of fatigue data

as representative of a single underlying population. Due to the large number of tests conducted under the same process and test conditions this offers a fairly unique possibility for characterizing variation in fatigue life in the low HCF regime for LPBF produced and heat treated 17-4. Figure 35 provides an empirical survival function that describes the variation in the tested specimens across builds A1, A2, A3, and A4. Fatigue lives exhibit a coefficient of variation of 79%, should the specimen with $N_f = 509{,}052$ be considered, and 51% otherwise. The survival function shows a somewhat linear decrease in probability of survival through roughly 150,000 cycles, after which the right-skewed nature of observed fatigue lives dominates. Parametric measures can also be fitted to the whole set of data – Figure 35 shows maximum likelihood estimated Weibull and lognormal theoretical survival functions superimposed on the data. Survival functions were calculated as the compliment of the respective cumulative distribution functions. This provides a better judge of fit than superimposing a PDF on a histogram as no binning is required that would obscure the data. The Weibull survivor function appears to fit the data in the middle of the life regime better and provide a more conservative estimate in the low life regime. Examining these two distributions as PDFs, shown in Figure 36, the difference is more evident. The Weibull PDF notably does not approach $N = 0$ asymptotically, due to its shape parameter. Altogether, the Weibull distribution appears a more appropriate model for fatigue life scatter, due to its fit and conservative nature at points. In a design context a finite lower limit on life probability might need to be established. If one notes the confidence bounds on the parameters of both fitted functions from Figure 28 these estimations appear to be fairly descriptive of the true underlying population.

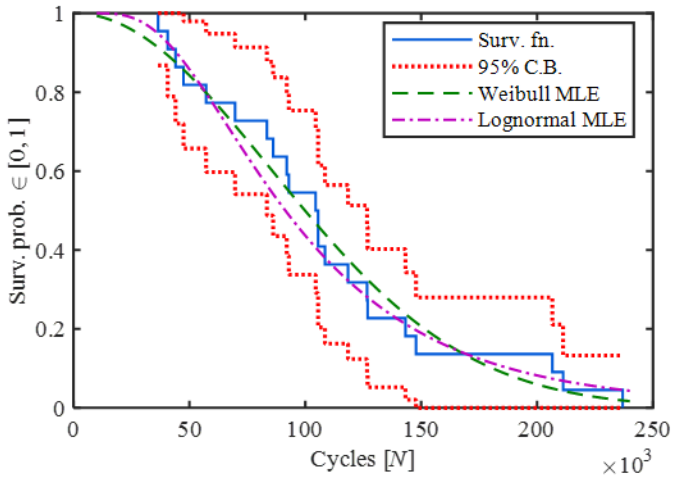

Figure 35. Survival function as estimated by the Kaplan-Mier method for specimens tested at S_{max} = 867 MPa, R = 0.1 from all groups A1, A2, A3, and A4. 95% confidence bounds derived by Greenwood's formula. Weibull and lognormal theoretical survival functions are calculated via MLE. Outlier specimen A3-2-8 has been excluded.

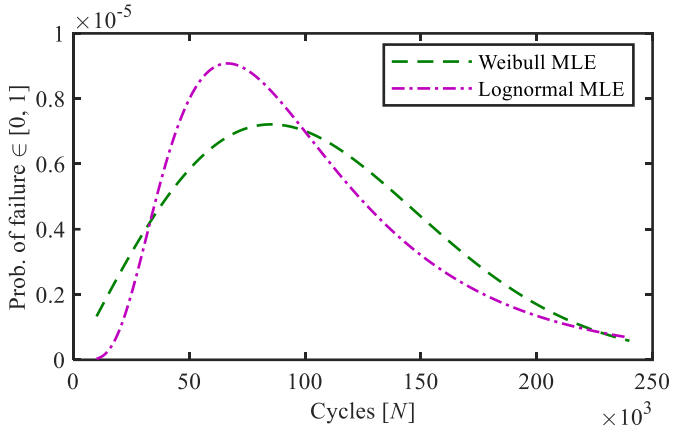

Figure 36. PDFs fitted to the life of specimens tested at S_{max} = 867 MPa, R = 0.1 from all groups A1, A2, A3, and A4 via MLE. Outlier specimen A3-2-8 has been excluded.

Evidently, the LPBF process studied here has several stochastic underlying factors that have produced this result. In this case it seems that the precise nature of the build plate layout has driven a large amount of this variation, and since nearly all of the build plate was used and fairly evenly sampled by the conducted tests these descriptors provide a strong picture of fatigue life scatter typical in HCF. A study of the fracture surfaces suggests that variation in defect size and position appear to contribute significantly to fracture initiation. That said, barring defects of extreme size and severity (which were not

observed), there does not appear to be a relation between defect size and fatigue life implying that overall concentration of defects, which enable faster crack growth, are more important in determining fatigue life. This observation follows with findings from other researchers who have identified the crack incubation stage in AM parts that present flaws to be negligible and HCF to be more governed by crack growth [84]. This might explain the spatial origin dependence of fatigue, as the mechanisms that change powder bed quality and composition across the build area would affect the gross amount and density of defects in build plate locations that are more heavily affected than others.

CLOSING

5.1 Conclusions

Taking the whole of the presented results into account, it is possible to draw several conclusions on the analyzed LPBF process and powder conditions. Powder characteristics are shown to change, but with limited effects on the end product. The conducted experiments have illuminated several interesting fatigue properties. An enumeration of the conclusions drawn from this study are presented below.

1. Repeated process exposure of in-machine powder supplies has been shown to evolve the powder quickly, with less than roughly 86 hours of build time significantly altering A2 powder supplies, and subsequent process exposures further altering the A3 and A4 powder supplies. Effects were primarily seen in PSD, flowability, and powder rheology. Fusion process byproducts increased the number of large particles. Powder decreased in flowability and increased in cohesivity. Each of these outcomes can be conceptually connected to deleterious effects on powder bed quality of powder layers that are produced with these powders.
2. The evolution of in-machine powder supplies due to repeated process exposure does not match the evolution of powder properties seen in powder recycling practices. Recycling tends to increase shift virgin powder PSD curves right by the reduction of fine particles and addition of large particles, albeit ones that fit within the original virgin powder PSD. In-machine repeated process exposure does not reduce the number of fine particles and does add particles of a size previously not represented in the virgin powder PSD.

3. The studied powder condition does not produce detectable effects in mechanical properties. Tensile properties, fatigue life in HCF, and hardness are shown not to change with powder condition.
4. Fatigue life appears to be largely driven by two things: LoF defects which randomly fall in subsurface regions and initiate cracks, and bulk defect concentration that enables crack growth. Both of these variables exhibit considerable variation, which appears to be partly attributable to how powder bed conditions vary withing the build area. This produces a heteroscedastic variation in fatigue life as a function of build plate spatial origin.

5.2 Contributions, limitations, and future study

The contributions of this thesis are in the characterization of an understudied powder condition – in-machine repeated process exposed powders – and its effects. This work provides a fuller picture of the LPBF process and the feedstock material it utilizes. These materials are not to be thought of as static in their attributes once loaded into an LPBF machine – they evolve with exposure to processing conditions. These results will be presented in a publication aimed at the AM community. Another contribution is in the selection of techniques that might be applied to characterizing the highly variant fatigue behavior seen in AM materials. Although the applied methods are not new, communication of this work is expected to introduce them to a community of researchers that are unfamiliar with these tools. Finally, several insights that further the understanding of fatigue mechanisms and driving process conditions are identified. This informs future development of LPBF processes and the selection of post-processing steps, such as HIP, that can be taken to mitigate the identified issues. These results will be considered for

publication in a journal or conference that would invite critique from experts in both the AM and fracture & fatigue fields.

This thesis is not without its limitations. Powder PSD and chemistry were not studied to the level of thoroughness that would form a inform greater conclusions on the evolution of powder characteristics. Additionally, in the area of powder characterization, the discovered changes in powder characteristics are quite subtle and due to this the precision and bias of the measurement methods used should considered when interpreting the results. A highly specific material system and associated heat treatment has been investigated, even if it is a relevant combination. Notably, many conclusions of fatigue properties are based in reasoning that should be confirmed with continued experimentation. With this thesis' main research question being related to powder conditions additional results on the dependence of fatigue life on build plate spatial origin did not receive as thorough an investigation as they require. Future work will include a continuation of the presented fatigue testing, fracture surface characterization, and statistical representation of the behavior the produced typical of the produced components. Fatigue crack growth testing, interrupted fatigue testing, and more extensive fractography would be needed to state the conclusions provided with greater certainty. Additionally, simulation and experimental work on the nature of powder bed quality based on the suspected underlying mechanisms that vary within the build area would further this work.

REFERENCES

[1] J. A. Slotwinski and E. J. Garboczi, "Metrology Needs for Metal Additive Manufacturing Powders," *J. Miner. Met. Mater. Soc.*, vol. 67, no. 3, p. 6, 2015, doi: 10.1007/s11837-014-1290-7.

[2] D. Bourell, M. C. Leu, and D. W. Rosen, Eds., "Roadmap for Additive Manufacturing, Identifying the Future of Freeform Processing." The University of Texas at Austin, 2009.

[3] J. A. Slotwinski, E. J. Garboczi, P. E. Stutzman, C. F. Ferraris, S. S. Watson, and M. A. Peltz, "Characterization of Metal Powders Used for Additive Manufacturing," *J. Res. Natl. Inst. Stand. Technol.*, vol. 119, p. 460, Oct. 2014, doi: 10.6028/jres.119.018.

[4] M. J. Heiden *et al.*, "Evolution of 316L stainless steel feedstock due to laser powder bed fusion process," *Addit. Manuf.*, vol. 25, pp. 84–103, Jan. 2019, doi: 10.1016/j.addma.2018.10.019.

[5] P. D. Nezhadfar, A. Soltani-Tehrani, A. Sterling, N. Tsolas, and N. Shamsaei, "The Effects of Powder Recycling on the Mechanical Properties of Additively Manufactured 17-4 PH Stainless Steel," presented at the Solid Freeform Fabrication, Austin, Texas, 2018.

[6] M. Schmidt *et al.*, "Laser based additive manufacturing in industry and academia," *CIRP Ann.*, vol. 66, no. 2, pp. 561–583, 2017, doi: 10.1016/j.cirp.2017.05.011.

[7] T. Lienert, T. Siewert, S. Babu, and V. Acoff, Eds., "Laser Beam Welding," in *ASM Handbook, Volume 6A, Welding Fundamentals and Processes*, ASM International, 2011, pp. 556–569.

[8] T. Lienert, T. Siewert, S. Babu, and V. Acoff, Eds., "Laser Deposition Processes," in *ASM Handbook, Volume 6A, Welding Fundamentals and Processes*, ASM International, 2011, pp. 587–594.

[9] C. B. Williams, J. K. Cochran, and D. W. Rosen, "Additive manufacturing of metallic cellular materials via three-dimensional printing," *Int. J. Adv. Manuf. Technol.*, vol. 53, no. 1–4, pp. 231–239, Mar. 2011, doi: 10.1007/s00170-010-2812-2.

[10] M. Kamal and G. Rizza, "Design for metal additive manufacturing for aerospace applications," in *Additive Manufacturing for the Aerospace Industry*, Elsevier, 2019, pp. 67–86.

[11] D. D. Rosen, D. S. Johnston, and M. Reed, "Design of General Lattice Structures for Lightweight and Compliance Applications," Loughborough University, 2006, p. 14.

[12] T. Niendorf *et al.*, "Functionally Graded Alloys Obtained by Additive Manufacturing," *Adv. Eng. Mater.*, vol. 16, no. 7, pp. 857–861, Jul. 2014, doi: 10.1002/adem.201300579.

[13] D. Bourell *et al.*, "Materials for additive manufacturing," *CIRP Ann.*, vol. 66, no. 2, pp. 659–681, 2017, doi: 10.1016/j.cirp.2017.05.009.

[14] F. Calignano *et al.*, "Overview on Additive Manufacturing Technologies," *Proc. IEEE*, vol. 105, no. 4, pp. 593–612, Apr. 2017, doi: 10.1109/JPROC.2016.2625098.

[15] J. Schmelzle, E. V. Kline, C. J. Dickman, E. W. Reutzel, G. Jones, and T. W. Simpson, "(Re)Designing for Part Consolidation: Understanding the Challenges of Metal Additive Manufacturing," *J. Mech. Des.*, vol. 137, no. 11, p. 111404, Nov. 2015, doi: 10.1115/1.4031156.

[16] H. Ko, S. K. Moon, and J. Hwang, “Design for additive manufacturing in customized products,” *Int. J. Precis. Eng. Manuf.*, vol. 16, no. 11, pp. 2369–2375, Oct. 2015, doi: 10.1007/s12541-015-0305-9.
[17] I. Gibson, D. W. Rosen, and B. Stucker, “Design for Additive Manufacturing,” in *Additive Manufacturing Technologies:*, I. Gibson, D. W. Rosen, and B. Stucker, Eds. Boston, MA: Springer US, 2010, pp. 299–332.
[18] R. K. Leach, D. Bourell, S. Carmignato, A. Donmez, N. Senin, and W. Dewulf, “Geometrical metrology for metal additive manufacturing,” *CIRP Ann.*, pp. 1–24, Jun. 2019, doi: 10.1016/j.cirp.2019.05.004.
[19] A. D. Dressler, E. W. Jost, J. C. Miers, D. G. Moore, C. C. Seepersad, and B. L. Boyce, “Heterogeneities Dominate Mechanical Performance of Additively Manufactured Metal Lattice Struts,” *Addit. Manuf.*, Jun. 2019, doi: 10.1016/j.addma.2019.06.011.
[20] E. Stugelmayer, “Characterization of Process Induced Defects in Laser Powder Bed Fusion Processed AlSi10Mg Alloy,” Graduate Theses & Non-Theses, Montana Tech, 2018.
[21] M. Seifi, A. Salem, J. Beuth, O. Harrysson, and J. J. Lewandowski, “Overview of Materials Qualification Needs for Metal Additive Manufacturing,” *JOM*, vol. 68, no. 3, pp. 747–764, Mar. 2016, doi: 10.1007/s11837-015-1810-0.
[22] A. Yadollahi, M. J. Mahtabi, A. Khalili, H. R. Doude, and J. C. Newman, “Fatigue life prediction of additively manufactured material: Effects of surface roughness, defect size, and shape,” *Fatigue Fract. Eng. Mater. Struct.*, vol. 41, no. 7, pp. 1602–1614, Jul. 2018, doi: 10.1111/ffe.12799.
[23] “MSFC-STD-3716:STANDARD FOR ADDITIVELY MANUFACTURED SPACEFLIGHT HARDWARE BY LASER POWDER BED FUSION IN METALS.” NASA MSFC, Oct. 18, 2017.
[24] S. Moylan, J. Slotwinski, A. Cooke, K. Jurrens, and M. A. Donmez, “An Additive Manufacturing Test Artifact,” *J. Res. Natl. Inst. Stand. Technol.*, vol. 119, p. 429, Oct. 2014, doi: 10.6028/jres.119.017.
[25] F. Caltanissetta, M. Grasso, S. Petrò, and B. M. Colosimo, “Characterization of in-situ measurements based on layerwise imaging in laser powder bed fusion,” *Addit. Manuf.*, vol. 24, pp. 183–199, Dec. 2018, doi: 10.1016/j.addma.2018.09.017.
[26] B. Lane and H. Yeung, “Process Monitoring Dataset from the Additive Manufacturing Metrology Testbed (AMMT): ‘Three-Dimensional Scan Strategies,’” *J. Res. Natl. Inst. Stand. Technol.*, vol. 124, p. 124033, Nov. 2019, doi: 10.6028/jres.124.033.
[27] Ritchie, Davidson, Boyce, Campbell, and Roder, “High-cycle fatigue of Ti-6Al-4V,” *Fatigue Fract. Eng. Mater. Struct.*, vol. 22, no. 7, pp. 621–631, Jul. 1999, doi: 10.1046/j.1460-2695.1999.00194.x.
[28] F. H. Kim, A. L. Pintar, J. Fox, A. M. Donmez, and A.-F. Obaton, “Probability of Detection of X-Ray Computed Tomography of Additive Manufacturing Defects,” in *46th Annual Review of Progress in Quantitative Nondestructive Evaluation*, Portland, OR, 2019, p. 3.
[29] S. Romano, A. Brandao, J. Gumpinger, M. Gschweitl, and S. Beretta, “Qualification of AM parts: Extreme value statistics applied to tomographic measurements,” *Mater. Des.*, vol. 131, pp. 32–48, 2017, doi: 10.1016/j.matdes.2017.05.091.

[30] P. Samal and J. Newkirk, Eds., “History of Powder Metallurgy,” in *ASM Handbook, Volume 7, Powder Metallurgy*, ASM International, 2015, pp. 3–8.
[31] P. Samal and J. Newkirk, Eds., “Metal and Alloy Powders for Welding, Hardfacing, Brazing, and Soldering[1],” in *ASM Handbook, Volume 7, Powder Metallurgy*, ASM International, 2015, pp. 769–782.
[32] P. Samal and J. Newkirk, Eds., “Powder Metallurgy Methods and Applications,” in *ASM Handbook, Volume 7, Powder Metallurgy*, ASM International, 2015, pp. 9–19.
[33] S. Berumen, F. Bechmann, S. Lindner, J.-P. Kruth, and T. Craeghs, “Quality control of laser- and powder bed-based Additive Manufacturing (AM) technologies,” *Phys. Procedia*, vol. 5, pp. 617–622, 2010, doi: 10.1016/j.phpro.2010.08.089.
[34] A. du Plessis and E. Macdonald, “Hot isostatic pressing in metal additive manufacturing: X-ray tomography reveals details of pore closure,” *Addit. Manuf.*, vol. 34, p. 101191, Aug. 2020, doi: 10.1016/j.addma.2020.101191.
[35] U. O. B. de Oliveira, “Laser treatment of alloys,” University of Groningen, 2007.
[36] P. Samal and J. Newkirk, Eds., “Materials Standards and Test Method Standards for Powder Metallurgy,” in *ASM Handbook, Volume 7, Powder Metallurgy*, ASM International, 2015, pp. 45–51.
[37] Energetics Incporated, Ed., “Measurement Science Roadmap for Metal-Based Additive Manufacturing.” NIST, May 2013.
[38] Atomization Technology Innovation Consortium, Ed., “Roadmap for the Development of Advanced Atomization and Spraying Technologies.” ASM International, Mar. 2017.
[39] A. T. Sutton, C. S. Kriewall, M. C. Leu, and J. W. Newkirk, “Powder characterisation techniques and effects of powder characteristics on part properties in powder-bed fusion processes,” *Virtual Phys. Prototyp.*, vol. 12, no. 1, pp. 3–29, Jan. 2017, doi: 10.1080/17452759.2016.1250605.
[40] I. E. Anderson, E. M. H. White, and R. Dehoff, “Feedstock powder processing research needs for additive manufacturing development,” *Curr. Opin. Solid State Mater. Sci.*, vol. 22, no. 1, pp. 8–15, Feb. 2018, doi: 10.1016/j.cossms.2018.01.002.
[41] G. Jacob, C. U. Brown, M. A. Donmez, S. S. Watson, and J. Slotwinski, “Effects of powder recycling on stainless steel powder and built material properties in metal powder bed fusion processes,” National Institute of Standards and Technology, Gaithersburg, MD, NIST AMS 100-6, Feb. 2017. doi: 10.6028/NIST.AMS.100-6.
[42] A. Amado, M. Schmid, G. Levy, and K. Wegener, “Advances in SLS Powder Characterization,” in *22nd Annual International Solid Freeform Fabrication Symposium*, Austin, Texas, 2011, p. 15.
[43] J. Clayton, D. Millington-Smith, and B. Armstrong, “The Application of Powder Rheology in Additive Manufacturing,” *JOM*, vol. 67, no. 3, pp. 544–548, Mar. 2015, doi: 10.1007/s11837-015-1293-z.
[44] D. M. Drake, “Key Quality Characteristics of Metal Powder for Powder Bed Fusion and Directed Energy Deposition,” Colorado School of Mines, 2018.
[45] T. Senthilvelan, K. Raghukandan, and A. Venkatraman, “Testing and Quality Standards for Powder Metallurgy Products,” *Mater. Manuf. Process.*, vol. 18, no. 1, pp. 105–112, Jan. 2003, doi: 10.1081/AMP-120017592.
[46] “Standard Test Method for Particle Size Distribution of Metal Powders and Related Compounds by Light Scattering.”

[47] ASTM International, “E2651-19 Guide for Powder Particle Size Analysis,” ASTM International, West Conshohocken, PA, 2019. doi: 10.1520/E2651-19.
[48] ASTM International, “E1019-18 Standard Test Methods for Determination of Carbon, Sulfur, Nitrogen, and Oxygen in Steel, Iron, Nickel, and Cobalt Alloys by Various Combustion and Inert Gas Fusion Techniques,” ASTM International, West Conshohocken, PA, 2018.
[49] ASTM International, “B964-16 Standard Test Method for Apparent Density of Non-Free-Flowing Metal Powders Using the Carney Funnel,” ASTM International, West Conshohocken, PA, 2016.
[50] ASTM International, “B215-15 Standard Practices for Sampling Metal Powders,” ASTM International, West Conshohocken, PA, 2015.
[51] ASTM International, “B213-20 Test Methods for Flow Rate of Metal Powders Using the Hall Flowmeter Funnel,” ASTM International, West Conshohocken, PA, 2020. doi: 10.1520/B0213-17.
[52] “Standard Test Method for Shear Testing of Powders Using the Freeman Technology FT4 Powder Rheometer Shear Cell.”
[53] M. Barclift, S. Joshi, T. Simpson, and C. Dickman, “Cost Modeling and Depreciation for Reused Powder Feedstocks in Powder Bed Fusion Additive Manufacturing,” in *Proceedings of the 26th Annual International Solid Freeform Fabrication Symposium*, Austin, Texas, p. 22.
[54] J.-P. Kruth, G. Levy, F. Klocke, and T. H. C. Childs, “Consolidation phenomena in laser and powder-bed based layered manufacturing,” *CIRP Ann.*, vol. 56, no. 2, pp. 730–759, 2007, doi: 10.1016/j.cirp.2007.10.004.
[55] W. E. Luecke and J. A. Slotwinski, “Mechanical Properties of Austenitic Stainless Steel Made by Additive Manufacturing,” *J. Res. Natl. Inst. Stand. Technol.*, vol. 119, p. 398, Oct. 2014, doi: 10.6028/jres.119.015.
[56] A. Strondl, O. Lyckfeldt, H. Brodin, and U. Ackelid, “Characterization and Control of Powder Properties for Additive Manufacturing,” *JOM*, vol. 67, no. 3, pp. 549–554, Mar. 2015, doi: 10.1007/s11837-015-1304-0.
[57] P. E. Carrion, A. Soltani-Tehrani, N. Phan, and N. Shamsaei, “Powder Recycling Effects on the Tensile and Fatigue Behavior of Additively Manufactured Ti-6Al-4V Parts,” *JOM*, vol. 71, no. 3, pp. 963–973, Mar. 2019, doi: 10.1007/s11837-018-3248-7.
[58] A. Soltani-Tehrani, J. Pegues, and N. Shamsaei, “Fatigue Behavior of Additively Manufactured 17-4 PH Stainless Steel: The Effects of Part Location and Powder Re-use,” *Addit. Manuf.*, Jun. 2020, doi: 10.1016/j.addma.2020.101398.
[59] H. K. Rafi, D. Pal, N. Patil, T. L. Starr, and B. E. Stucker, “Microstructure and Mechanical Behavior of 17-4 Precipitation Hardenable Steel Processed by Selective Laser Melting,” *J. Mater. Eng. Perform.*, vol. 23, no. 12, pp. 4421–4428, Dec. 2014, doi: 10.1007/s11665-014-1226-y.
[60] B. AlMangour and J.-M. Yang, “Improving the surface quality and mechanical properties by shot-peening of 17-4 stainless steel fabricated by additive manufacturing,” *Mater. Des.*, vol. 110, pp. 914–924, Nov. 2016, doi: 10.1016/j.matdes.2016.08.037.
[61] P. D. Nezhadfar, R. Shrestha, N. Phan, and N. Shamsaei, “Fatigue behavior of additively manufactured 17-4 PH stainless steel: Synergistic effects of surface roughness and heat treatment,” *Int. J. Fatigue*, vol. 124, pp. 188–204, Jul. 2019, doi: 10.1016/j.ijfatigue.2019.02.039.

[62] S. Takaki, K. Fukunaga, J. Syarif, and T. Tsuchiyama, “Effect of Grain Refinement on Thermal Stability of Metastable Austenitic Steel,” *Mater. Trans.*, vol. 45, no. 7, pp. 2245–2251, 2004, doi: 10.2320/matertrans.45.2245.
[63] L. E. Murr *et al.*, “Microstructures and Properties of 17-4 PH Stainless Steel Fabricated by Selective Laser Melting,” *J. Mater. Res. Technol.*, vol. 1, no. 3, pp. 167–177, Oct. 2012, doi: 10.1016/S2238-7854(12)70029-7.
[64] T. L. Starr, K. Rafi, B. Stucker, and C. M. Scherzer, “CONTROLLING PHASE COMPOSITION IN SELECTIVE LASER MELTED STAINLESS STEELS,” in *23rd Annual International Solid Freeform Fabrication Symposium*, Austin, Texas, 2012, p. 8.
[65] G. Raugel and Y. Yi, “Recyclability Study on Inconel 718 and Ti-6Al-4V Powders for Use in Electron Beam Melting,” *J. Dyn. Differ. Equ.*, vol. 27, no. 3–4, pp. 333–334, Dec. 2015, doi: 10.1007/s10884-015-9497-z.
[66] L. C. Ardila *et al.*, “Effect of IN718 Recycled Powder Reuse on Properties of Parts Manufactured by Means of Selective Laser Melting,” *Phys. Procedia*, vol. 56, pp. 99–107, 2014, doi: 10.1016/j.phpro.2014.08.152.
[67] Y. Murakami and S. Beretta, “Small Defects and Inhomogeneities in Fatigue Strength: Experiments, Models and Statistical Implications,” *Extremes*, vol. 2, pp. 123–147, 1999, doi: 10.1023/A:1009976418553.
[68] K. Gall, M. F. Horstemeyer, B. W. Degner, and J. Fan, “On the driving force for fatigue crack formation from inclusions and voids in a cast A356 aluminum alloy,” *Int. J. Fract.*, vol. 108, pp. 207–233, 2001, doi: 10.1023/A:1011033304600.
[69] A. Yadollahi and N. Shamsaei, “Additive Manufacturing of Fatigue Resistant Materials: Challenges and Opportunities,” *Int. J. Fatigue*, vol. 98, pp. 14–31, May 2017, doi: 10.1016/j.ijfatigue.2017.01.001.
[70] R. G. Budynas, J. K. Nisbett, and J. E. Shigley, *Shigley’s mechanical engineering design*, Tenth edition. New York, NY: McGraw-Hill Education, 2015.
[71] P. H. Wirsching, “NASA Contractor Report 3697: Statistical Summaries of Fatigue Data for Design Purposes.” NASA, Jul. 1983.
[72] J. Schijve, *Fatigue of structures and materials*, Second edition. Dordrecht: Springer, 2009.
[73] “Standard Practice for Statistical Analysis of Linear or Linearized Stress-Life (S-N) and Strain-Life (ε-N) Fatigue Data.”
[74] P. H. Wirsching, “Fatigue reliability,” *Prog. Struct. Eng. Mater.*, vol. 1, no. 2, pp. 200–206, Jan. 1998, doi: 10.1002/pse.2260010213.
[75] Y. Wu and P. H. Wirsching, “Advanced Reliability Method for Fatigue Analysis,” *J. Eng. Mech.*, vol. 110, no. 4, pp. 536–553, Apr. 1984, doi: 10.1061/(ASCE)0733-9399(1984)110:4(536).
[76] A. Brot, “Weibull or Log-Normal Distribution to Characterize Fatigue Life Scatter – Which Is More Suitable?,” in *ICAF 2019 – Structural Integrity in the Age of Additive Manufacturing*, A. Niepokolczycki and J. Komorowski, Eds. Cham: Springer International Publishing, 2020, pp. 551–561.
[77] W. Weibull, “A Statistical Distribution Function of Wide Applicability,” *ASME J. Appl. Mech.*, pp. 293–297, Sep. 1951.
[78] R. Sakin and İ. Ay, “Statistical analysis of bending fatigue life data using Weibull distribution in glass-fiber reinforced polyester composites,” *Mater. Des.*, vol. 29, no. 6, pp. 1170–1181, Jan. 2008, doi: 10.1016/j.matdes.2007.05.005.

[79] M. Shirani and G. Härkegård, “Fatigue life distribution and size effect in ductile cast iron for wind turbine components,” *Eng. Fail. Anal.*, vol. 18, no. 1, pp. 12–24, Jan. 2011, doi: 10.1016/j.engfailanal.2010.07.001.
[80] M. Tiryakioğlu, “On the relationship between statistical distributions of defect size and fatigue life in 7050-T7451 thick plate and A356-T6 castings,” *Mater. Sci. Eng. A*, vol. 520, no. 1–2, pp. 114–120, Sep. 2009, doi: 10.1016/j.msea.2009.05.005.
[81] S. Chi-liu, “The Statistical Modeling of Fatigue Data,” University of Arizona, 1994.
[82] H. Li, D. Wen, Z. Lu, Y. Wang, and F. Deng, “Identifying the Probability Distribution of Fatigue Life Using the Maximum Entropy Principle,” *Entropy*, vol. 18, no. 4, p. 111, Mar. 2016, doi: 10.3390/e18040111.
[83] “AMS2759/3G Heat Treatment Precipitation-Hardening Corrosion-Resistant, Maraging, and Secondary Hardening Steel Parts,” SAE International, 2018. doi: 10.4271/AMS2759/3H.
[84] A. Yadollahi, M. Mahmoudi, A. Elwany, H. Doude, L. Bian, and J. C. Newman, “Fatigue-life prediction of additively manufactured material: Effects of heat treatment and build orientation,” *Fatigue Fract. Eng. Mater. Struct.*, vol. 43, no. 4, pp. 831–844, Apr. 2020, doi: 10.1111/ffe.13200.
[85] P. D. Nezhadfar *et al.*, “Fatigue crack growth behavior of additively manufactured 17-4 PH stainless steel: Effects of build orientation and microstructure,” *Int. J. Fatigue*, vol. 123, pp. 168–179, Jun. 2019, doi: 10.1016/j.ijfatigue.2019.02.015.
[86] S. Romano, P. D. Nezhadfar, N. Shamsaei, M. Seifi, and S. Beretta, “High cycle fatigue behavior and life prediction for additively manufactured 17-4 PH stainless steel: Effect of sub-surface porosity and surface roughness,” *Theor. Appl. Fract. Mech.*, vol. 106, Apr. 2020, doi: 10.1016/j.tafmec.2020.102477.
[87] S. Romano, A. Brückner-Foit, A. Brandão, J. Gumpinger, T. Ghidini, and S. Beretta, “Fatigue properties of AlSi10Mg obtained by additive manufacturing: Defect-based modelling and prediction of fatigue strength,” *Eng. Fract. Mech.*, vol. 187, pp. 165–189, Jan. 2018, doi: 10.1016/j.engfracmech.2017.11.002.
[88] A. Yadollahi, N. Shamsaei, S. M. Thompson, A. Elwany, Linkan Bian, and M. Mahmoudi, “Fatigue Behavior of 17-4 PH Stainless Steel Fabricated Using Selective Laser Melting,” 2015, doi: 10.13140/RG.2.1.3996.2323.
[89] S. Sarkar, C. S. Kumar, and A. K. Nath, “Effects of heat treatment and build orientations on the fatigue life of selective laser melted 15-5 PH stainless steel,” *Mater. Sci. Eng. A*, vol. 755, pp. 235–245, May 2019, doi: 10.1016/j.msea.2019.04.003.
[90] O. A. Quintana and W. Tong, “Effects of Oxygen Content on Tensile and Fatigue Performance of Ti-6Al-4 V Manufactured by Selective Laser Melting,” *JOM*, vol. 69, no. 12, pp. 2693–2697, Dec. 2017, doi: 10.1007/s11837-017-2590-5.
[91] “Certificate of Analysis & Certificate of Conformity, TruForm 174-L62,” Praxair Surface Technologies, Oct. 2018.
[92] ASTM International, “A693-16 Standard Specification for Precipitation-Hardening Stainless and Heat-Resisting Steel Plate, Sheet, and Strip,” ASTM International, West Conshohocken, PA, 2016.
[93] ASTM International, “E8/E8M-16ae1 Standard Test Methods for Tension Testing of Metallic Materials,” ASTM International, West Conshohocken, PA, 2020.

[94] ASTM International, “E466-15: Practice for Conducting Force Controlled Constant Amplitude Axial Fatigue Tests of Metallic Materials,” ASTM International, West Conshohocken, PA, 2015. doi: 10.1520/E0466-15.
[95] R. Esmaeilizadeh, U. Ali, A. Keshavarzkermani, Y. Mahmoodkhani, E. Marzbanrad, and E. Toyserkani, “On the effect of spatter particles distribution on the quality of Hastelloy X parts made by laser powder-bed fusion additive manufacturing,” *J. Manuf. Process.*, vol. 37, pp. 11–20, Jan. 2019, doi: 10.1016/j.jmapro.2018.11.012.
[96] L. E. Criales, Y. M. Arısoy, B. Lane, S. Moylan, A. Donmez, and T. Özel, “Laser powder bed fusion of nickel alloy 625: Experimental investigations of effects of process parameters on melt pool size and shape with spatter analysis,” *Int. J. Mach. Tools Manuf.*, vol. 121, pp. 22–36, Oct. 2017, doi: 10.1016/j.ijmachtools.2017.03.004.
[97] K. H. G. Chua and Y. Y. C. Choong, “Investigation of the effects on the print location during selective laser melting process,” in *Proceedings of the 3rd International Conference on Progress in Additive Manufacturing*, 2018, pp. 613–618, doi: Proceedings of the 3rd International Conference on Progress in Additive Manufacturing.
[98] U. K. Viswanathan, S. Banerjee, and R. Krishnan, “Effects of aging on the microstructure of 17-4 PH stainless steel,” *Mater. Sci. Eng. A*, vol. 104, pp. 181–189, Oct. 1988, doi: 10.1016/0025-5416(88)90420-X.
[99] C. N. Hsiao, C. S. Chiou, and J. R. Yang, “Aging reactions in a 17-4 PH stainless steel,” *Mater. Chem. Phys.*, vol. 74, no. 2, pp. 134–142, Mar. 2002, doi: 10.1016/S0254-0584(01)00460-6.
[100] R. Bhambroo, S. Roychowdhury, V. Kain, and V. S. Raja, “Effect of reverted austenite on mechanical properties of precipitation hardenable 17-4 stainless steel,” *Mater. Sci. Eng. A*, vol. 568, pp. 127–133, Apr. 2013, doi: 10.1016/j.msea.2013.01.011.
[101] E. Jost, “CT scan of 316L LPBF dogbone, manufactured by Sandia National Labs.” Feb. 2020.
[102] W. S. Liggett, S. R. Low, D. J. Pitchure, and J. Song, “Capability in Rockwell C scale hardness,” *J. Res. Natl. Inst. Stand. Technol.*, vol. 105, no. 4, p. 511, Jul. 2000, doi: 10.6028/jres.105.041.
[103] E. Fitzgerald and W. Everhart, “The Effect of Location on the Structure and Mechanical Properties of Selective Laser Melted 316L Stainless Steel,” in *Proceedings of the 26th Annual International Solid Freeform Fabrication Symposium*, Austin, Texas, 2016, p. 10.
[104] M. Simonelli *et al.*, “A Study on the Laser Spatter and the Oxidation Reactions During Selective Laser Melting of 316L Stainless Steel, Al-Si10-Mg, and Ti-6Al-4V,” *Metall. Mater. Trans. A*, vol. 46, no. 9, pp. 3842–3851, Sep. 2015, doi: 10.1007/s11661-015-2882-8.